Constraining Planetary Science Problems with Micro-Paleomagnetism

by

Cauê S. Borlina

Submitted to the Department of Earth, Atmospheric and Planetary Sciences
in partial fulfillment of the requirements for the degree of

Doctor of Philosophy

at the

MASSACHUSETTS INSTITUTE OF TECHNOLOGY

February 2022

Author .....
Department of Earth, Atmospheric and Planetary Sciences
Jan. 14, 2021

Certified by .....
Benjamin P. Weiss
Professor
Thesis Supervisor

Accepted by .....
Robert van der Hilst
Head of Department

Constraining Planetary Science Problems with Micro-Paleomagnetism

by

Cauê S. Borlina

Submitted to the Department of Earth, Atmospheric and Planetary Sciences
on Jan. 14, 2021, in partial fulfillment of the
requirements for the degree of
Doctor of Philosophy

Abstract

With the development of micro-paleomagnetic techinques we can measure the magnetic field of micro-scale samples that have direct implications for problems in planetary science. In this thesis I used the techniques from micro-paleomagnetism to address two main problems: (1) when Earth's magnetic field started and (2) how did the magnetic field in the solar nebula varied in space and time. For the first, I conducted paleomagnetic measurements with the Jack Hills zircon grains from Western Australia to address the early evolution of Earth's magnetic field, which has implications for the thermal evolution of the Earth and habitability. For the latter I focused on the paleomagnetism of three different components from CO carbonaceous chondrites: calcium-aluminum-rich inclusions, chondrules and matrix, with them we can measure the solar nebula magnetic field which have directs implications to planetary formation. This thesis is divided into 6 chapters. The first one introduces the general theme of the thesis. The second presents my work on the early evolution of Earth's magnetic field. The third, fourth and fifth present my results from meteoritic magnetism. The sixth chapter discusses future work.

Thesis Supervisor: Benjamin P. Weiss
Title: Professor

Acknowledgments

First, I would like to acknowledge my mentors in the last 10 years that supported me in my academic pursuits. That includes Germán Martínez, Nilton Rennó, Bethany Ehlmann, Edwin Kite and Steven Vance. I also would like to thank my PhD advisor Benjamin Weiss for all the support, thought provoking conversations and freedom to pursue the scientific questions that I was interested; Eduardo Lima for our many hours of scientific debates and fun times that we had in the laboratory; Richard Harrison for the scientific support; and François Tissot for the mentorship in the last few years. I also would like to thank Kevin McKeegan, Timothy Grove, Richard Binzel, Xuening Bai and Julien de Wit for being part of my thesis committee and providing advice and mentorship in the last years.

Second, I would like to acknowledge the people around me that were also part of this thesis. This includes Clara Maurel, and all the fun time we spent getting a PhD, talking about life, and how to make caipirinhas, and Elias Mansbach, for sharing the PhD experience with me. I also would like to thank Rona Oran, John Biersteker, Claire Nichols, James Bryson, Brenda Carbone, Jay Shah and everyone else that was/is part of MIT Paleomagnetism Lab.

Finally, I would like to thank my family for their support: my mom, Rosa, my dad, Valter, my aunt, Daniela, and the dogs, Juan and Nutella. Without them I would not have come to pursue my career in the US and I am very thankful for all of their efforts that helped me get here. I also would like to thank my wife's family including Joanna, Sean, Ian and Paul for all the support and for having accepted and welcomed me. And of course, I would like to thank my wife, Anastasia, for being the best partner one could have during this marathon that was a PhD. She not only shared this entire process with me by having many late night lab dates, but also supported me immensely, and everyday I am thankful for having her in my life.

Contents

Part I

Thesis Overview

Chapter 1

Magnetism in the Early Solar System

While this thesis includes problems from different fields including geophysics, geology, planetary science and astrophysics, they all fall under one main theme which is *what magnetism from the past can inform about planetary formation and evolution.*

Magnetism can be found in several places in the universe, including inside of planetary bodies, evolving planetary systems, molecular clouds and supernovae. In this thesis I focus on two main types of magnetic fields to address problems in planetary science: (1) magnetic fields generated in Earth's interior and (2) magnetic fields that existed during the very beginning of the solar system.

Several planets in the solar system have magnetic fields that are generated in their interior. These include Mercury, Earth, Jupiter, Saturn, Uranus and Neptune. Studying magnetic fields can provide a very unique opportunity to reach the inaccessible interior of a planet. Recent missions have provided key constraints on the structure and dynamics of planetary interiors [e.g., Johnson et al. (2020); Moore et al. (2019, 2018); Dougherty et al. (2018); Anderson et al. (2011)]. While measurements of present-day magnetic fields can provide information about the current state of a planetary body, magnetic fields from the past can provide information to understand how the planet changed in the last billion years: by obtaining records of the magnetic field from the past we can understand how magnetic fields evolve and change over time, providing insights about the mechanisms that sustain them and ultimately constraining the evolution of planetary interiors. In turn, these measurements can help

us understand the interaction between interior and surface of the planetary body and how magnetic fields could have played a role in controlling their atmospheres (Gunell et al., 2018). Magnetic fields from the past can be recorded in rocks through magnetic minerals and paleomagnetic techniques can help us extract information about the recorded field (Tauxe, 2010). **In Chapter 2, I targeted Earth's oldest rocks, the zircon grains from the Jack Hills (Compston and Pidgeon, 1986), as potential paleomagnetic targets to determine when Earth's magnetic started. By combining novel techniques in micro-paleomagnetism with rock magnetism, geochemistry and high-resolution imaging of magnetic carriers, I show that different from what has been proposed they are not robust paleomagnetic targets and that other minerals are required to establish when Earth's field started.**

The other type of magnetic fields that I study in this thesis is that active in protoplanetary disks (we use *solar nebula* to describe the protoplanetary disk phase of the solar system), the birth place of planets and stars in the universe. In fact, magnetic fields, which are coupled to the gas in protoplanetary disks, play a central role in the evolution of disk (Bai and Goodman, 2009; Bai, 2017; Turner et al., 2014; Weiss et al., 2021). Obtaining measurements of protoplanetary disk magnetic fields is very challenging, and ongoing efforts through astronomical observations are pursuing evidence of magnetic fields in current active disks (Weiss et al., 2021). An alternative solution is to use meteorites that formed during the solar nebula as a way to probe the magnetic field of a protoplanetary disk. Similar to Earth rocks, meteorites and their inclusions can contain magnetic minerals that recorded the ambient magnetic field. In turn, these measurements can be used to understand how the solar system and other planetary systems form [see Weiss et al. (2021) for a complete review of previous paleomagnetic measurements from the solar nebula]. **In Chapters 3-5, I targeted carbonaceous chondrites and their inclusions to determine what was the magnetic field at the very beginning of the solar nebula, $\sim$2 million years later and how fast our solar nebula dispersed. I find evidence for what could be the oldest magnetic record of the solar system (Chapter 3),**

for a gap that played a central role in setting the composition of the early solar system (Chapter 4) and that the solar nebula dissipation happened within less than 1.5 million years (Chapter 5).

Part II

The Hadean Dynamo

Chapter 2

Paleomagnetism of Jack Hills Zircon Grains

2.1 Chapter Introduction

The time of origin of the geodynamo has important implications for the thermal evolution of the planetary interior and the habitability of early Earth. It has been proposed that detrital zircon grains from Jack Hills, Western Australia, provide evidence for an active geodynamo as early as 4.2 billion years (Ga) ago. However, our combined paleomagnetic, geochemical, and mineralogical studies on Jack Hills zircons indicate that most have poor magnetic recording properties and secondary magnetization carriers that postdate the formation of the zircons. Therefore, the existence of the geodynamo before 3.5 Ga ago remains unknown.

2.2 Why Single Crystal Paleomagnetism?

Determining the history of the geodynamo before 3.5 Ga ago is limited by the lack of a well-preserved Archean-Hadean rock record. However, the discovery of Hadean

detrital zircon grains in metasediments of the Jack Hills, Western Australia (Compston and Pidgeon, 1986), opens up the possibility of studying the magnetic history of Earth during its first billion years. In particular, primary ferromagnetic inclusions (e.g., magnetite) in the zircons may contain a thermoremanent magnetization (TRM) that records the paleointensity of the ancient field during primary cooling (Fu et al., 2017; Weiss et al., 2015; Tarduno et al., 2014; Sato et al., 2015).

To preserve such a record, magnetite-bearing zircon crystals must have avoided being heated above magnetite's 580°C Curie temperature over their subsequent histories (Weiss et al., 2015, 2018). Furthermore, obtaining accurate paleointensity studies with well-determined ages for bulk zircon grains requires that the grains' natural remanent magnetization (NRM) be dominated by a TRM rather than a secondary crystallization remanent magnetization (CRM) carried by ferromagnetic inclusions formed or altered during aqueous alteration events after zircon crystallization (Weiss et al., 2015, 2018).

Two recent studies (Tarduno et al., 2015, 2020) using single-crystal paleointensity analyses of Jack Hills zircon grains suggested that a geodynamo existed as early as 4.2 Ga ago with a surface field $\sim$0.1 to 1 times that of present-day Earth. However, those studies (Tarduno et al., 2015, 2020) had three main limitations: (i) The ages of the NRMs in the grains analyzed are unknown (Weiss et al., 2015, 2016); (ii) the grains were not shown to contain a TRM rather than a secondary CRM (Weiss et al., 2018; Tang et al., 2019; Trail et al., 2016); (iii) the studies' grain selection criteria, which targeted grains with NRM intensities $>10^{-12}$ Am^2, might inadvertently have excluded zircons that would have recorded the absence of a dynamo (i.e., that carry no magnetization). In addition, there have been no independent studies corroborating their paleomagnetic measurements. The latter issue is particularly important because Jack Hills zircons have some of the weakest magnetic NRMs measured in the history of paleomagnetism and therefore require exceptionally sensitive magnetometry techniques and stringent contamination controls. To further evaluate the evidence of an early dynamo and address these limitations, we conducted coupled paleomagnetic, geochemical, and mineralogical analyses on Jack Hills detrital zircon grains.

2.3 Methodology

2.3.1 Location of the Samples

Our field work was conducted in the Jack Hills in 2002 and 2012. We separated zircons from five rock samples (named D175C, D175H, D175L, and Cong14c) collected at the Hadean zircon discovery site, location W74 (Cavosie et al., 2004), in the Jack Hills, Western Australia, Australia (Compston and Pidgeon, 1986), during the 2012 field trip. Table S1 of Borlina et al. (2020) shows the sampling information about the bulk samples and the source material for the grains.

2.3.2 Zircon Separation from Host Rocks

The five rock samples were manually sledged to gravel size fragments in the Massachusetts Institute of Technology Isotope Laboratory. These fragments then were pulverized in a Shatterbox using an all-ceramic grinding vessel and sieved to $<$500-μm grain size. The material then was mixed in water in a 4-liter beaker, and the suspended material ($\leq$5 μm) was decanted; this wash process was repeated 15 times. The remaining sand- and silt-size fraction then was dried under a heat lamp (maximum temperature of 45^{o}C). The heavy-mineral aliquot was separated by immersion in a high-density liquid (methylene iodide; specific gravity, 3.32), followed by rinsing in acetone and air drying. Zircon grains then were handpicked under a binocular microscope using nonmagnetic tweezers. Note that our separation procedures did not involve the standard use of a Frantz isodynamic separator for removing paramagnetic and ferromagnetic minerals, as the high magnetic field of the Frantz would otherwise alter any original NRM that might have been present in the grains.

2.3.3 Ion and Electron Microprobe Measurements

U and Pb isotopes, backscattered electron microscopy (BSE microscopy), CL, and Li-ion measurements were carried out in the UCLA Secondary Ion Mass Spectrometry (SIMS) Laboratory at the University of California, Los Angeles (UCLA). The

samples were transported between MIT and UCLA in magnetically shielded cans. Approximately 400 grains were placed in 10 separate 2.5-cm-diameter epoxy EPO-TEK 301 mounts and polished to approximately their midplanes. Information about bulk rock source for the zircon grains and their respective mount number are compiled in Table S1 of Borlina et al. (2020). U and Pb isotopes were measured on a CAMECA IMS 1270 SIMS, using an $16O^-$ primary beam, with beam currents of 12 to 15 nA. A beam diameter of ∼20 to 30 μm was used. Isotopes measured were $^{94}Zr^{20}$, ^{204}Pb, ^{206}Pb, ^{207}Pb, ^{208}Pb, ^{232}Th, ^{238}U, and $^{238}U^{16}O$. The mass-resolving power was ≥5500. We used oxygen flooding for improved Pb ionization (Quidelleur et al., 1997). For the common Pb correction, we used a ^{204}Pb correction assuming laboratory contamination with environmental Pb from southern California, specifically the San Diego sewage (Patterson et al., 1976), with common $^{206}Pb/^{204P}b$ = 18.86, common $^{207P}Pb/^{204}Pb$ = 15.62, and common $^{208}Pb/^{204}Pb$ = 38.34. An initial $^{206}Pb/^{207}Pb$ ratio survey on 3754 grains was used to identify grains older than 3.5 Ga for all mounts except UCLA 1, 2, and 3; the latter were instead surveyed for grains older than 3.8 Ga. U-Pb measurements and BSE, CL, and Li images were then acquired from grains that passed this criterion. We calculated the $^{207}Pb/^{206}Pb$ and $^{206}Pb/^{238}U$ dates and inferred the $^{207}Pb/^{235}U$ using the known U isotope ratio ($^{238}U/^{235}U$ = 137.88). We assigned ages using $^{207}Pb/^{206}Pb$ ratios. $^{207}Pb/^{206}Pb$ and $^{206}Pb/^{238}U$ were used to compute the discordance (Spencer et al., 2016; Wang and Wilde, 2018)

$$\left| \frac{\frac{^{207}Pb}{^{206}Pb}}{\frac{^{206}Pb}{^{238}Pb}} - 1 \right| \times 100\% \tag{2.1}$$

Table S2 from Borlina et al. (2020) compiles U-Pb measurements for the grains that passed the initial $^{206}Pb/^{207}Pb$ survey. Table S3 from Borlina et al. (2020) contains age and uncertainties for the 77 grains selected for the paleomagnetic experiments. BSE and CL images were acquired with a TESCAN VEGA3 scanning electron microscope equipped with a TESCAN three-channel color CL detector and TESCAN retractable BSE detector (Bell et al., 2015). Li-ion images were acquired using a

CAMECA IMS 1290 SIMS at the UCLA SIMS Laboratory. We used the Hyperion II radio frequency plasma primary ion source (Liu et al., 2018) with a 250 to 300 pA ^{16}O- beam focused to a <1-μm spot size. We rastered the beam over a 50×50–μm area and recorded 10 frames of ion images of ^{7}Li and ^{30}Si. We used the program WinImage to accumulate the 10 frames each of ^{7}Li and ^{30}Si (image intensity was integrated over all 10 frames), and computed the ratio of the two to get an image of ^{7}Li/^{30}Si intensity. We normalized ^{7}Li to ^{30}Si to account for charging (where the ionization rate may be heterogeneous because of accumulation of charge in the sample as it is continually bombarded with negative secondary ions). The spatial resolution of the images is equivalent to the spot size, so any feature >1 mum is not an artifact. Because boundaries on zones are resolved to $\leq$1 μm, blurring of zones by more than this value means they are actually physically smooth over that length scale. A detectable Li zoning with thickness of <20 μm provides evidence that the sample has not been heated >550^{o}C for more than 1 million years ((Trail et al., 2016). However, this method might provide an underestimation of the peak temperature experienced by the grains in some cases Tang et al. (2017). As discussed in the main text, whether or not the Li band criterion is used to filter our samples does not change the overall outcome of this study. In the supplementary material of Borlina et al. (2020) we provide evidence that the ion and electron microprobe work measurements did not remagnetize the samples. We also provide the complete set of images taken from all measured grains

2.3.4 Acid Washing

We previously showed that most Jack Hills zircon grains, when untreated with concentrated (6 M) hydrochloric acid (HCl) acid, have magnetization likely dominated by secondary minerals coating the zircons (Weiss et al., 2018). Therefore, before paleomagnetic measurements, all grains and one sample (18-11-13) fragmented into three pieces. All acid washing steps were performed in the MIT Isotope Laboratory cleanroom facilities.

2.3.5 Paleomagnetism

Following HCl and H_2SO_4 acid-washing, grains were mounted in pits drilled into Corning Eagle XG glass slides, following similar procedures previously developed for analyzing zircons from the Bishop Tuff (Fu et al., 2017). Figure S3 of Borlina et al. (2020) shows the overall measuring setup. Optical and magnetic field images of the four glass holders with the analyzed here (with the exception of four whole grains; see section S5 of the supplementary materials of Borlina et al. (2020)) were washed with a 6 M HCl solution for 12 min at room temperature, followed by rinsing in Milli-Q water and air drying. Zircon crystals from samples D175C and D175H were washed with HCl before U-Pb measurements, while grains from D175L and Cong14C were washed with HCl after U-Pb measurements. All grains selected for paleomagnetic measurements were extracted from the epoxy mounts using nonmagnetic tools (Semprex probe needle, lot 18) and washed in 70% H_2SO_4 for 3 hours to remove any residual epoxy deposits before magnetic measurements. During extraction, five samples (18-8-12, 18-15-18, 18-4-8, 1-1-9, and 18-2-12) fragmented into two pieces. The absolute orientation of the grains was not maintained between mounting in the epoxy for the electron microscopy and ion probe measurements and in the glass mount for paleomagnetic measurements. However, the orientation of the grains and the glass mount was kept fixed throughout the paleomagnetic measurements. Heating steps were conducted with an ASC Scientific TD48-SC thermal demagnetizer, which provides temperature control with accuracy of better than $\pm$5C. An IZZI protocol was used in this experiment (Yu et al., 2004). The in-field step used a 50-μT laboratory magnetic field.

Because of the overall weak magnetic moments of the samples (between 6.05×10^{-15} and 4.15×10^{-12} Am^2), NRM measurements were conducted with the SQUID microscope (Weiss et al., 2007) in the MIT Paleomagnetism Laboratory. The configuration used in these experiments, including the sample holder and the mount with the zircon crystals, yields an approximate distance from the SQUID sensor to the midplane of the sample of $\sim$360 μm [see Fig. S3 from Borlina et al. (2020)]. This distance includes

the sensor to the window separation (∼200 μm), the thickness of the Corning Eagle XG glass left at the bottom of the wells (∼60 μm), and half of the size of the grain (∼100 μm).

2.3.6 Quantum Diamond Microscopy

After paleomagnetic measurements, select grains were extracted from the glass mount, placed in epoxy EPO-TEK 301, and polished again. We used the QDM (Glenn et al., 2017) in the Harvard Paleomagnetics Laboratory to constrain the location of the magnetization carriers within the grains. Samples were measured in contact with the sensing diamond after a 0.4-T IRM was applied in the out-of-plane direction using an ASC model IM-10-3 impulse magnetizer. We measured the magnetic field intensity at a height of ∼5 µm above the sample along the [111] direction of the diamond crystal lattice using projective magnetic microscopy with a resolution of 1.17 micrometers per pixel (Glenn et al., 2017). We isolated the remanent field signal of ferromagnetic grains by measuring the sample successively under two mutually antiparallel 0.9-mT bias fields and computing the out-of-plane magnetic field using a spectral algorithm (Lima and Weiss, 2016). The absolute orientation of the grains differed between the SQUID microscopy measurements and these QDM measurements.

2.3.7 Transmission Electron Microscopy

TEM was conducted in the Wolfson Electron Microscopy Suite at the University of Cambridge. Our TEM analysis targeted locations based on the QDM maps previously measured. The TEM foil was prepared using a dual-beam focused ion beam microscope FEI Helios NanoLab (Hillsboro, OR, USA) with an area of ∼60 μm^2 and a depth of ∼7 μm. An in-situ lift-out technique was used to site-specifically extract the foil from the place with magnetic signals mapped with the QDM, and a cleanup procedure with low acceleration voltage was used to reduce surface damage of the foil. The TEM sample was examined using a FEI Tecnai Osiris TEM with an extreme Schottky field emission gun. The instrument was equipped with four

large-area energy-dispersive x-ray spectrometer detectors, providing a fast chemical compositional measurement. The analysis was carried out at scanning TEM mode at 200 kV, where both bright-field and high-angle annular dark-field images were acquired.

2.4 Results

We extracted the zircon crystals from the pebble conglomerate that we sampled in 2012 at the Hadean zircon discovery locality at Erawandoo Hill [site W74 (Weiss et al., 2015, 2016))] using nonmagnetic techniques described above. From these samples, 3754 zircons were washed with HCl acid and mounted in nonmagnetic epoxy, polished to approximately their midplanes, and dated using U-Pb chronometry. Grains found to have U-Pb ages older than 3.5 Ga (a total of 250) were analyzed using backscattered scanning electron (BSE) microscopy, cathodoluminescence (CL) imaging, and Li-ion imaging. BSE and CL images were used to assess the likelihood of secondary CRM by identifying zircon overgrowths, recrystallization zones, metamictization, cracks, and secondary deposits of minerals in void spaces (Corfu et al., 2003). The goal of Li-ion imaging was to constrain the possibility of secondary TRM by providing estimates of the peak metamorphic temperatures experienced by zircons (Trail et al., 2016).

We defined a set of selection criteria that enables the identification of detrital zircon grains minimally affected by secondary TRM and CRM overprints Fig. 2-1 (1) U-Pb age discordance $<$10%; (2) lack of visible cracks, metamictization, and secondary deposits in BSE images and the presence of zonation in CL images interpreted as a primary igneous texture; and (3) presence of detectable primary Li zoning with thickness of $<$20 μm as observed by Li-ion imaging (11). Criterion (3) indicates the absence of TRM overprints acquired during $\gtrsim$1 million years (Ma) long, $\gtrsim$550°C metamorphic events under the assumption that natural Li diffusivity is similar to experimentally determined values (Tang et al., 2017). Note that these three criteria are based on measurements that only probe the polished surface of the grain (i.e., do not survey the full grain volume). Furthermore, the analytical methods used for criterion

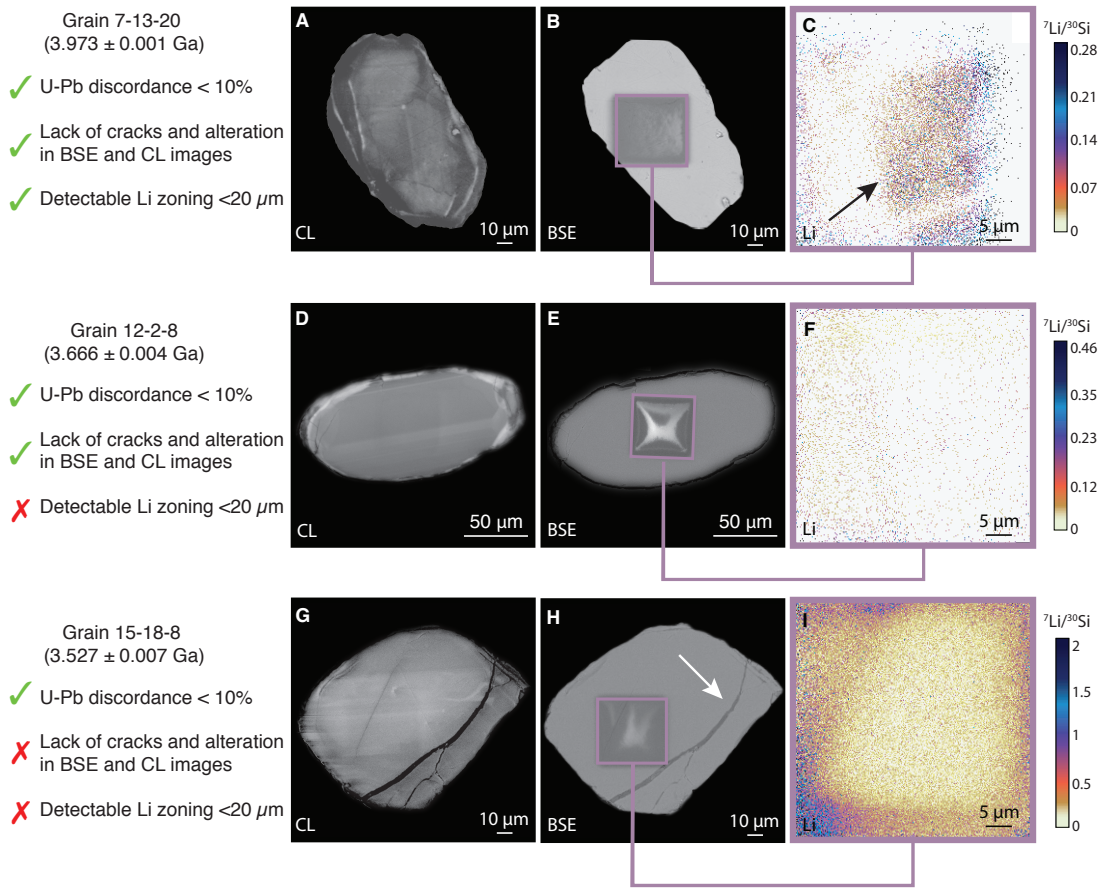

Figure 2-1: **Examples of grains that pass and fail the selection criteria**. (**A** to **C**) Example of a zircon grain (7-13-20; 3.973 ± 0.001 Ga) that passes all selection criteria: U-Pb age discordance <10%, presence of zonation in CL (A), no signs of secondary deposits on the exposed surface from BSE (B), and <20-μm-thick Li zonation banding (black arrow), indicating that the sample may not have been fully thermally remagnetized since crystallization (C). (**D** to **F**) Example of a zircon grain (12-2-8; 3.666 ± 0.004 Ga) that passes some of the selection criteria: U-Pb age discordance <10%, presence of zonation in CL (D), no signs of secondary deposits on the exposed surface from BSE (E), and no observed Li zonation (F). (**G** to **I**) Example of a zircon grain (15-18-8; 3.527 ± 0.007 Ga) that fails most of the selection criteria: U-Pb age discordance <10%, absence of igneous zonation (G), presence of secondary mineral filling cracks at the lower right side of the grain (white arrow) (H), and no observed Li zonation (I).

(2) are unable to resolve the <1 μm-diameter single-domain magnetite grains that would carry stable primary magnetization. Thus, these criteria likely are necessary but not sufficient requirements for identifying a zircon with primary NRM.

Of a total of 250 zircon grains, only 3 grains passed all of the above selection cri-

teria. We selected these 3 grains, along with 53 grains that failed one or more criteria (including 13 subsamples from 6 grains), for subsequent paleomagnetic studies. As a control to confirm that our polishing and ion and electron microprobe measurements do not fundamentally alter the zircons' NRMs, we also analyzed an additional 21 grains in their natural unpolished forms from the same host rocks using nonmagnetic methods, 4 of which were acid-washed. We conducted paleomagnetic analyses on a total of 77 grains.

NRMs of the zircons ranged between 6.05×10^{-15} and 4.15×10^{-12} Am^2, and their magnetic moments were analyzed using SQUID microscopy as described above (Weiss et al., 2007; Lima and Weiss, 2016). Following methods previously developed for the Bishop Tuff zircons (Fu et al., 2017), we obtained paleointensity estimates for the 77 grains using the in-field zero-field zero-field in-field (IZZI) double-heating protocol (Yu et al., 2004) with partial TRM (pTRM) alteration checks at every other heating step starting at 300^oC.

We defined paleomagnetic quality criteria that are permissive compared with those of typical paleointensity studies of younger rocks [see the supplementary materials of Borlina et al. (2020) for a discussion on this]. This is because the overall goal of this study was to establish the presence or absence of a geodynamo at >3.5 Ga ago, which only requires paleointensities with order-of-magnitude uncertainties. Therefore, paleointensity estimates were considered acceptable when a sample (a) had a difference ratio sum $\leq$25% (Tauxe and Staudigel, 2004) and (b) gained a moment in the direction of the laboratory field during in-field steps with a maximum angular deviation $\leq15^o$ (Kirschvink, 1980). Criterion (a) indicates that minimal thermochemical alteration occurred during the paleointensity experiments, while criterion (b) provides evidence that the sample can record an ancient field's direction and intensity (while not requiring the presence or absence of such a field when the zircon acquired its magnetic record). In summary, samples that pass our initial selection criteria and paleomagnetic criteria are candidates for providing a robust constraint on the dynamo at the time of their crystallization. Conversely, samples with unstable NRM would either indicate the absence of a dynamo (if the sample passes the selection

and paleomagnetic criteria) or that the sample is unsuitable for paleointensity experiments (either because of poor magnetic recording properties and/or sample alteration during laboratory heating). Following the paleointensity experiments, we analyzed selected grains with quantum diamond magnetometry (QDM) (Glenn et al., 2017) coupled with transmission electron microscopy (TEM) to elucidate the origin of the magnetic sources within the grains.

Of the 77 zircon grains analyzed for paleointensity estimations, only a total of 6 grains passed the two paleomagnetic criteria. We found that 63 of the 77 samples failed paleomagnetic criterion (a), indicating alteration during our experiments. In addition, we found that 54 samples have poor magnetic recording properties, as indicated by their failure of paleomagnetic criterion (b). Among the six grains that passed both paleomagnetic criteria, only two passed all five combined selection and paleomagnetic criteria (Fig. 2-2). Even if we were to exclude Li zonation as one of the selection criteria, there would be no additional grains that would pass the other selection and paleomagnetic criteria (Tang et al., 2017). In addition, our analyses of the unpolished control grains confirm that polishing the grains did not increase the incidence of alteration during experiments or the magnetic recording quality [see the supplementary materials of Borlina et al. (2020) for a discussion on this].

The two grains that passed the five combined criteria were sample 7-13-20, with a U-Pb age of 3.973 $\pm$ 0.001 Ga, and sample 8-2-11, with a U-Pb age of 3.979 $\pm$ 0.007 Ga. Fig. 2-2 summarizes the selection process starting from the initial 3754 grains and ending at these 2 grains. Figures 2-3 and 2-4 show BSE, CL, Li, and paleomagnetic data for these two grains. The two grains each have at least two NRM components. Sample 7-13-20 (Fig. 2-3) has a low-temperature component that unblocked between room temperature and 200^{o}C, a medium-temperature component that unblocked between 200^o and 300^{o}C, and a high-temperature component that unblocked between 300^o and 580^{o}C. Sample 8-2-11 (Fig. 2-4) has a low-temperature component that unblocked between room temperature and 510^{o}C and a high temperature component that unblocked between 510^o and 580^{o}C. The 580^{o}C peak demagnetization temperature of the NRMs for both samples indicates that the high-temperature components

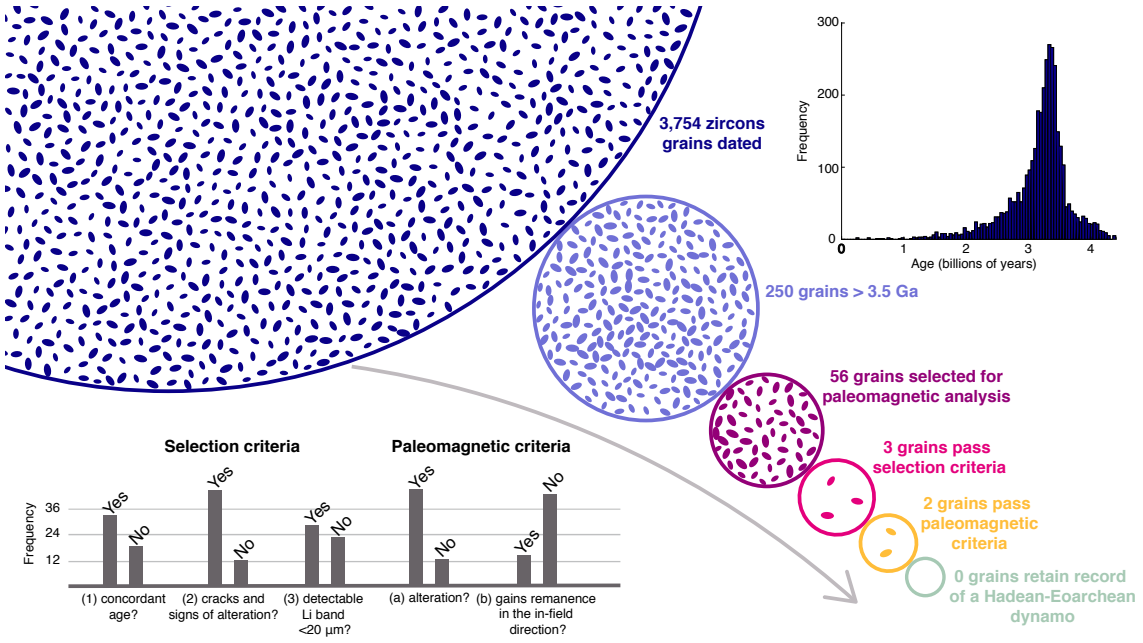

Figure 2-2: **Summary of zircon selection from the initial 3754 dated grains.** Each circle shows the number of zircon grains remaining after each selection step. The histogram on the top right shows the measured age distribution of the 3754 grains. From the 250 grains that were older than 3.5 Ga, we selected all grains that passed all the selection criteria (3 grains) and an additional set of 53 grains. The histograms at the bottom left show the number of grains that satisfy the various selection criteria [(1) U-Pb age discordance <10%; (2) lack of visible cracks, metamictization, and secondary deposits; and (3) detectable primary Li zoning with thickness of <20 μm] and paleomagnetic criteria [(a) the NRM component had a difference ratio sum 25%, and (b) the sample gained a moment in the direction of the laboratory field during in-field steps with a maximum angular deviation 15o over the same temperature range as the NRM component] for the 56 grains selected for paleomagnetic analysis. Only two grains pass all the selection and paleomagnetic criteria. In addition to the 56 polished grains shown here, 21 whole grains were also analyzed paleomagnetically as a control. No grain showed evidence for a Hadean-Eoarchean dynamo.

are carried by nearly pure magnetite.

Figure 2-5 shows an example of a grain that passes all of the selection criteria but fails all of the paleomagnetic criteria. Most of our grains present NRM demagnetization similar to the one in Fig. 2-5: unstable demagnetization, thermochemical alteration in the laboratory, and no in-field acquisition of remanence.

Subsequent to the paleointensity studies, grains 7-13-20 and 8-2-11 were analyzed in more detail to elucidate the nature and origin of their ferromagnetic inclusions.

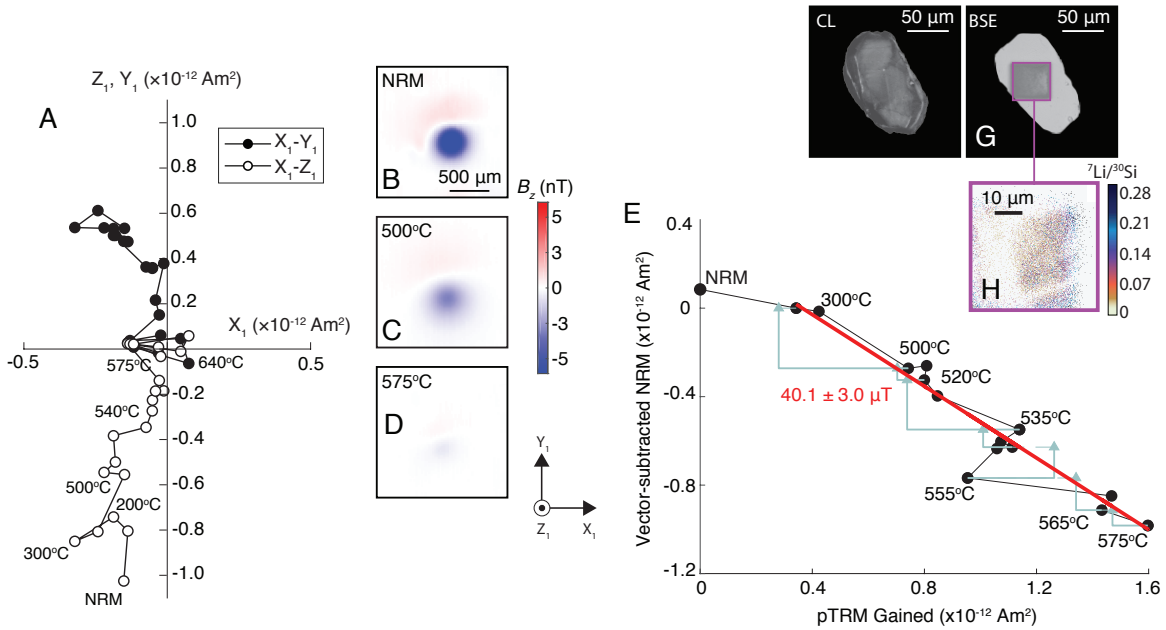

Figure 2-3: **Paleomagnetic data for zircon grain 7-13-20 (3.973 ± 0.001 Ga) that passes all selection and paleomagnetic criteria.** (**A**) Orthographic projection of NRM vector endpoints during thermal demagnetization. Closed symbols show the X-Y projection of the magnetization; open symbols show Z-Y projection of the magnetization. Selected demagnetization steps are labeled. (**B** to **D**) Out-of-the-page magnetic field component (B_z) maps measured at a height of 360 μm above the grains obtained with the SQUID microscope for the NRM, 500^{o}C, and 575^{o}C steps. We use a "1" subscript on X_1, Y_1, and Z_1 to denote the fact that the grain orientations during the thermal demagnetization and paleointensity experiments are different from the grain orientations during the BSE, CL, and Li measurements and during the QDM measurements (Fig. 2-6). (**E**) Vector-subtracted NRM from the 300^{o}C step versus pTRM grained during progressive laboratory heating. Blue triangles show pTRM checks. The red line shows the measurements used to compute paleointensity values (300^o to 580^{o}C). (**F** to **H**) CL, BSE, and Li images of the grains.

First, the isothermal remanent magnetization (IRM) of the samples was imaged with QDM (Glenn et al., 2017) to determine the location of the magnetization sources (Fig. 2-6). Following this, we used TEM to investigate internal regions with the strongest magnetization. We found no evidence of primary ferromagnetic inclusions. Instead, we observed magnetite crystals (identified using Moiré diffraction interferometry) (Tang et al., 2019) growing inside voids fed by iron that diffused along the regions of intersecting dislocations. We also identified magnetite crystals with high

aspect ratios, crystallographically aligned with the host zircon, and growing along dislocation cores [Fig. 2-6; see also (Tang et al., 2019)]. The alignment, aspect ratios, and locations of the magnetite grains within regions of recovery from accumulated radiation damage demonstrate that the grains are secondary in origin (White et al., 2017; Timms et al., 2012; Piazolo et al., 2016). No evidence has been put forth to support the speculation that they formed by exsolution and/or vapor deposition (Tarduno et al., 2020). The presence of secondary magnetite is not linked to alteration during laboratory heating steps, as demonstrated by the fact that these two grains passed paleomagnetic criterion (a) and that they contain voids with a diversity of shapes and sizes that commonly are empty or filled with phases other than magnetite, most commonly baddeleyite and ilmenite (Geisler et al., 2007). The magnetite apparently formed as a result of natural fluid alteration at an unknown time during the last 3.9 Ga, at which time their bulk host zircons would have acquired a secondary CRM.

2.5 Discussion

The data presented here suggest that the vast majority of Jack Hills zircons are not suitable for paleointensity studies of the Hadean-Eoarchean magnetic field. In particular, only 2 of 77 grains passed our five selection and paleomagnetic criteria. These two grains yielded results similar to those previously reported for Jack Hills zircons (Tarduno et al., 2015, 2020) and that were interpreted to be a record of a Hadean-Eoarchean dynamo: initial NRM intensities of $\sim 1 \times 10^{-12}$ Am^2, no signs of alteration, and stable NRM demagnetization exhibiting multiple components. However, close examination of both of our grains shows that their magnetic carriers are most likely secondary in origin. Therefore, the ages of their NRMs are unknown and certainly younger than their U-Pb ages. Their multicomponent NRMs are consistent with being CRMs overprinted by pTRMs because of heating events in the Jack Hills outcrop or else by younger CRMs. The presence of a CRM means that the thermal paleointensity experiments, which implicitly assume that the NRM is a TRM, will yield unreliable

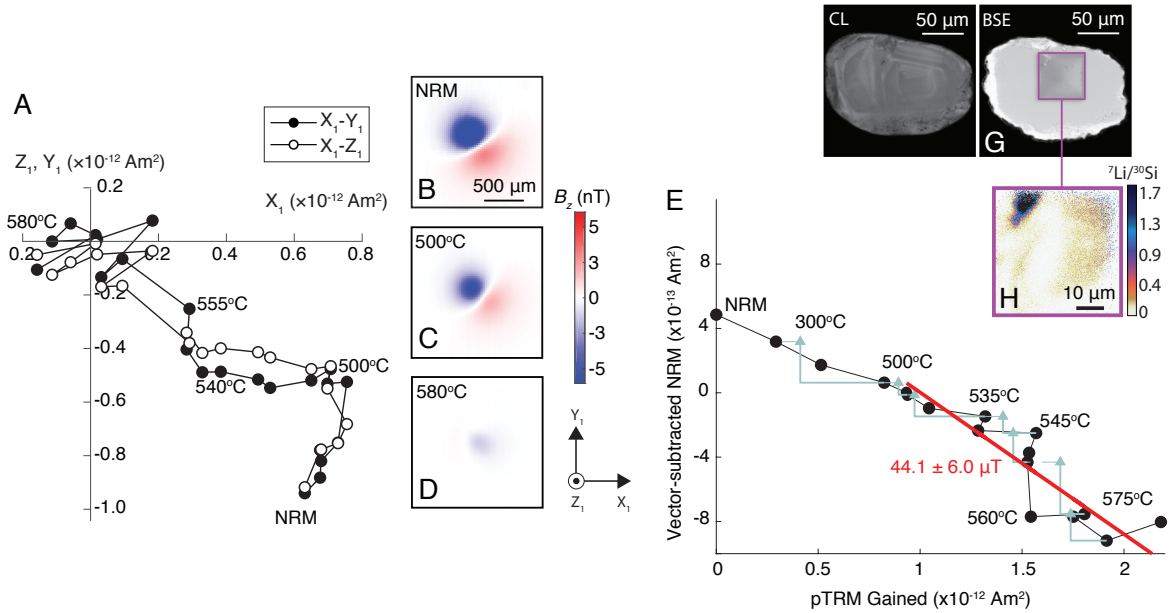

Figure 2-4: **Paleomagnetic data for zircon grain 8-2-11 (3.979 ± 0.007 Ga) that passes all selection and paleomagnetic criteria.** (**A**) Orthographic projection of NRM vector endpoints during thermal demagnetization. Closed symbols show the X-Y projection of the magnetization; open symbols show Z-Y projection of the magnetization. Selected demagnetization steps are labeled. (**B** to **D**) Out-of-the-page magnetic field component (B_z) maps measured at a height of 360 μm above the grains obtained with the SQUID microscope for the NRM, 500^{o}C, and 580^{o}C steps. We use a "1" subscript on X_1, Y_1, and Z_1 to denote the fact that the grain orientations during the thermal demagnetization and paleointensity experiments are different from the grain orientations during the BSE, CL, and Li measurements and during the QDM measurements (Fig. 2-6). (**E**) Vector-subtracted NRM from the 510^{o}C step versus pTRM grained during progressive laboratory heating. Blue triangles show pTRM checks. The red line shows the measurements used to compute paleointensity values (510^o to 580^{o}C). (**F** to **H**) CL, BSE, and Li images of the grains.

paleointensity values. We also note that unlike the previous studies (Tarduno et al., 2015, 2020), we found that the majority of grains analyzed paleomagnetically have poor demagnetization and remagnetization behavior. In conclusion, the existence of the dynamo before 3.5 Ga has yet to be established.

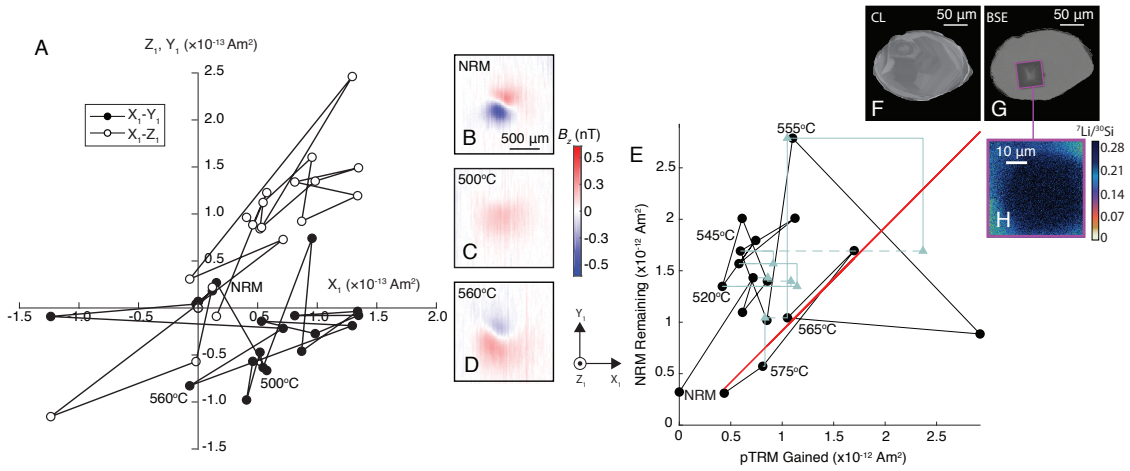

Figure 2-5: **Paleomagnetic data for zircon grain 15-1-7 (4.094 ± 0.005 Ga) that passes all selection and paleomagnetic criteria.** (**A**) Orthographic projection of NRM vector endpoints during thermal demagnetization. Closed symbols show the X-Y projection of the magnetization; open symbols show Z-Y projection of the magnetization. Selected demagnetization steps are labeled. (**B** to **D**) Out-of-the-page magnetic field component (B_z) maps measured at a height of 360 μm above the grains obtained with the SQUID microscope for the NRM, 500^{o}C, and 560^{o}C steps. We use a "1" subscript on X_1, Y_1, and Z_1 to denote the fact that the grain orientations during the thermal demagnetization and paleointensity experiments are different from the grain orientations during the BSE, CL, and Li measurements and during the QDM measurements (Fig. 2-6). (**E**) Vector-subtracted NRM from the 510^{o}C step versus pTRM grained during progressive laboratory heating. Blue triangles show pTRM checks. The red line shows the measurements used to compute paleointensity values (550^o to 580^{o}C). (**F** to **H**) CL, BSE, and Li images of the grains.

2.6 Conclusion

We suggest that the difference in results between our study and that of (Tarduno et al., 2015, 2020) may be due to our different measurement protocol, in which we washed the grains using concentrated (6 M) HCl to remove considerable amounts of secondary magnetic deposits before paleomagnetic measurements, used high-sensitivity magnetic microscopy that enabled measurements of samples with up to 1000 times weaker NRMs, and used QDM and TEM to constrain whether the magnetic carriers are primary in origin. Elucidating the early evolution of the geodynamo may require as yet unidentified detrital minerals that are less prone to radiation damage.

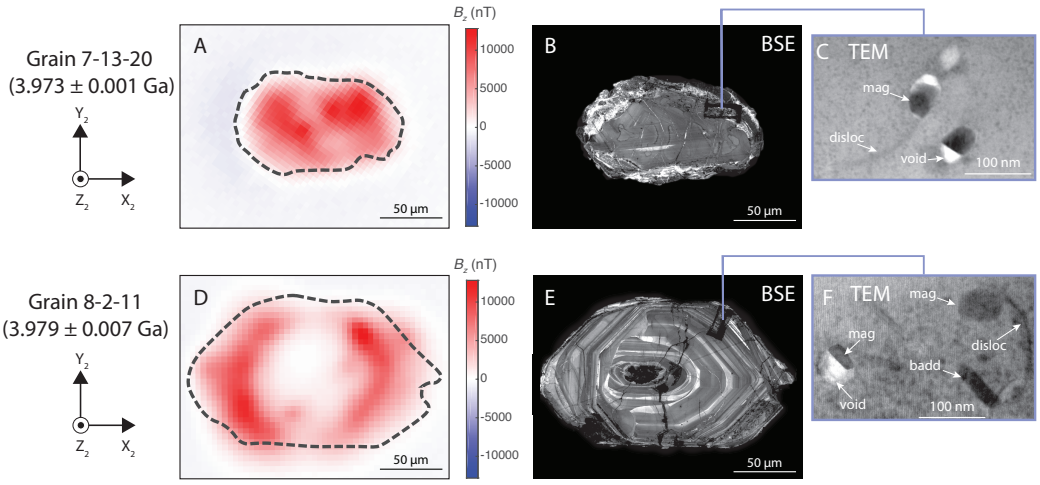

Figure 2-6: **Magnetite grains located in dislocations and filling parts of voids postdating igneous formation of the zircon host**. (**A** to **C**) Zircon grain 7-13-20. (**D** to **F**) Zircon grain 8-2-11. (A and D) QDM maps of the out-of-the-page magnetic field component (B_z) of an IRM applied to the grain used to locate magnetic sources at a height of 5 μm above the samples. We use X_2, Y_2, and Z_2 to denote that the grain orientations for these measurements differ from those during the paleointensity experiments (Figs. 2-3 to 2-5). (B and E) BSE images of the grains. The grains were repolished after the paleomagnetic experiments and before these BSE images. Note the difference when compared with the earlier BSE images of the same grains in Figs. 2-3 and 2-3; the images here expose several cracks that were not previously visible. (C and F) TEM analyses conducted in the vicinity of the strongest magnetic region of the grain by extracting rectangular focused ion beam sections (from rectangular regions visible in the BSE images). Magnetite ("mag") grains are seen to be forming inside voids that intersect dislocations ("disloc") and growing along dislocation cores that formed during recovery. Magnetite commonly is associated with baddeleyite ("badd"), a secondary product formed after recovery from radiation damage (Geisler et al., 2007), pointing to the fact that the magnetite crystals were not present in the zircon structure when the zircon crystal formed.

Part III

Solar Nebula Magnetic Fields

Chapter 3

Paleomagnetism of Calcium-aluminium-rich Inclusions

3.1 Chapter Introduction

Magnetic fields have been proposed to play a central role in the evolution of protoplanetary disks by transporting mass and angular momentum. Paleomagnetic studies of meteorites have shown that magnetic fields of ∼50-100 μT existed within 7 AU of the Sun at ∼2-3 million years (Ma) after the formation of calcium-aluminum-rich inclusions (CAIs), dispersing by ∼4 Ma after CAI formation. Nonetheless, the existence of magnetic fields and their role prior to 2 Ma after CAI formation remains undetermined. In this chapter, I seek to establish the magnetic field of the solar nebula during its first ∼20-50 thousand years by obtaining paleomagnetic measurements of CAIs. This might also shed light on CAI's poorly-understood formation and transport mechanisms. Our results indicate the presence of magnetic fields during the very beginning of the solar system and is likely the oldest known paleomagnetic record yet identified from any sample. When coupled to models that describe magnetically-driven accretion in protoplanetary disks, our results suggest that CAIs likely acquired their magnetic record at >8 AU. Given that previous isotopic, mineralogical and redox studies favor a formation of CAIs <0.1 AU from the Sun, our records suggest that CAIs acquired magnetization through reheating during or after transport to the outer

solar system, potentially associated with magnetized disk winds and stellar outbursts. Ongoing studies will investigate the CAI's isotopic composition and rock magnetic properties to determine the nature and origin of their magnetization.

3.2 Introduction

Calcium-aluminium-rich Inclusions (CAIs) were the first solids to form in the solar system (Krot, 2019). They have the oldest ages of any other inclusion in the solar system, dating back to ∼4567-4568 million years (Ma) (Connelly et al., 2017; Bouvier et al., 2011). CAIs are very diverse in terms of mineralogical composition, but they all contain one or more high temperature minerals such as corundum, hibonite, perovskite and/or melilite, potentially also containing clinopyroxene, anorthite, spinel, Fe-Ni metal, forsterite, and enstatite (Krot, 2019). CAIs formed through condensation, evaporation, aggregation and melting in a gas of solar composition near the proto-Sun (Krot, 2019). The formation of CAIs was fast, ∼10-50^{o}C hr^{-1} (Richter et al., 2002; Simon et al., 2019; Davis and MacPherson, 1996), and after their initial formation, secondary heating events likely happened within ∼0.2 Ma after CAI formation (Scott and Krot, 2013; Gounelle et al., 2009; Kita et al., 2013; Krot, 2019; MacPherson, 2013; McSween, 1999).

Although numerous petrological and geochronological studies have been conducted on CAIs [e.g., (Kita et al., 2013; Chi et al., 2009; MacPherson et al., 2017; Sugiura and Krot, 2007; McKeegan et al., 2000; Brennecka et al., 2018, 2020; Ebert et al., 2018)] along with a preliminary paleomagnetic study on an altered CAI from CV chondrites (Smethurst and Herrero-Bervera, 2002), no systematic paleomagnetic study of CAIs has been conducted to date. Here, we conduct paleomagnetic studies with CAIs to understand their formation mechanisms and to determine how they were transported to the >3 AU region of the solar nebula. The latter issue is of particular interest because while CAIs are expected to form close to the proto-Sun, they are currently found more commonly in carbonaceous chondrites, meteorites that likely formed >3 AU (Krot, 2019).

While some mechanisms account for both formation and transport of CAIs, others explain formation and transport independently. The X-winds (Shu et al., 1996) and the magnetically-driven disk wind (Salmeron and Ireland, 2012) mechanisms describe both formation and transport of CAIs. In the X-wind model, refractory inclusions are thermally processed <0.1 AU, then ejected to outer areas of the disk through magnetocentrifugal outflows. This model predicts that chondrules and refractory inclusions recorded fields of >80 to 400 μT while thermally processed at <0.1 AU from the proto-Sun (Shu et al., 1996). However, this model has been generally dismissed because if fails to explain several key observations about CAI formation [see Desch et al. (2010) and Krot et al. (2009) for a complete discussion on this].

Alternatively, magnetically-driven disk winds have been invoked to explain the formation of chondrules and refractory inclusions (Salmeron and Ireland, 2012; Scott et al., 2018). In this scenario, magnetically-driven winds that are active within several AU of a Young Stellar Object can lift dust up to ∼0.2 AU of the midplane of the disk, causing it to heat up to temperatures as high as ∼2000 K. The dust cools down as it returns to the disk due to drag at larger radial distances than their starting place. In this scenario, the magnetic record is that of the solar nebula at a few AU from the proto-Sun, which is expected to be of a few hundreds of μT (see discussion).

A mechanism that includes only formation is the proposed idea that CAIs formed close to proto-Jupiter due to temperatures associated with the formation of the gas giant (Brennecka et al., 2018). In this mechanism, CAIs would have recorded the ambient nebular field of a few hundreds of μT present in the 1-10 AU region.

Finally, a proposed mechanism of CAI transport is meridional flow, where viscous transport through magnetorotational instabilities leads to a outward meridional flow in the midplane region (Ciesla, 2007). Nonetheless, such meridional flow was not identified in global simulations of turbulence driven by the magnetorotational instability (Fromang et al., 2011). Moreover, in the recently more favored scenario of disk accretion driven by magnetized disk winds (Bai, 2017), transport of solids is more complex and outward transport appears inefficient (Hu and Bai, 2021).

Here, we discuss the first extensive study of CAIs as potential paleomagnetic

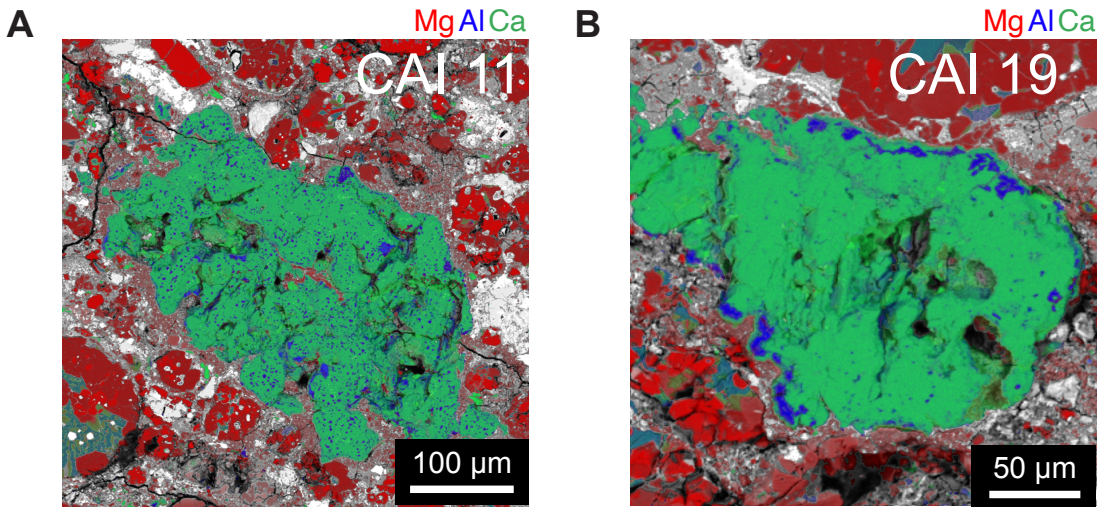

Figure 3-1: **Example of compositional maps from two selected CAIs used in this study.** (**A**) CAI 11 is a hibonite-bearing CAI. (**B**) CAI 19 is a melilite-rich CAI. Red indicates Mg, blue indicates Al and green indicates Ca.

targets. We used a meteorite that has experienced little alteration and metamorphism in the parent body Dominion Range (DOM) 08006 (3.00), and in fact one of the least altered samples available in the meteorite record (Davidson et al., 2019). We present our results and discuss them in the context of the different mechanisms for formation and transport of CAIs in the early solar system.

3.3 Methodology

3.3.1 Identification, Selection and Extraction of CAIs

We conducted an extensive survey among inclusions from two thick sections of DOM 08006 obtained from the same parent sample described in Chapter 4 and Borlina et al. (2021c). We targeted the thick sections by obtaining mineral maps, similar to the ones shown in Figs. 3-1A-B, and mineralogical identification. To obtain these, we used a EOL JXA-8200 Superprobe electron probe microanalyzer (EPMA) using wavelength dispersive spectroscopy (WDS) in the MIT Electron Microprobe Facility. Backscattered electron (BSE) images were obtained with the same instrument. The EPMA was operated at an accelerating voltage of 15 kV and a beam current of 10

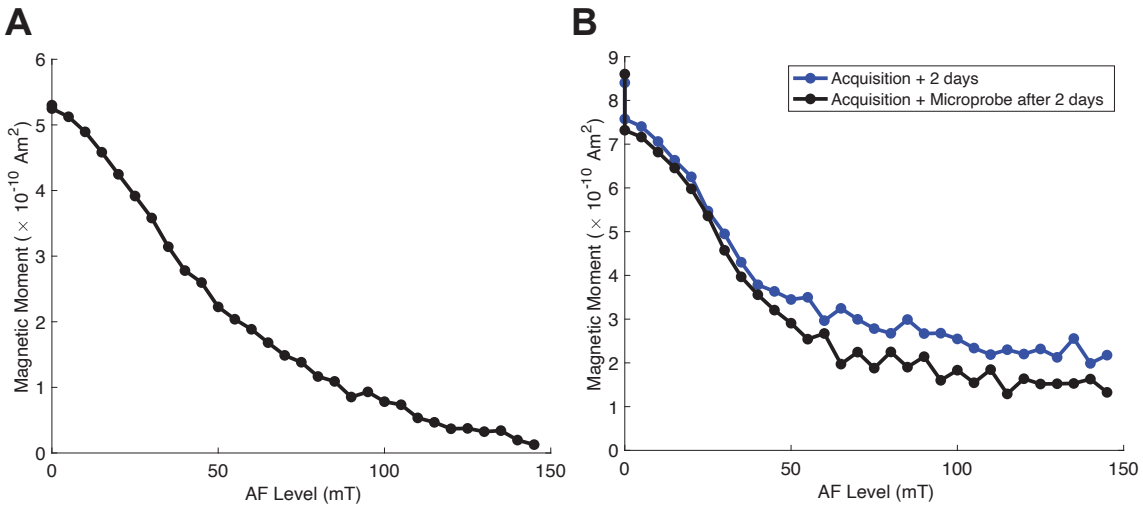

Figure 3-2: **AF demagnetization of ARMs from two distinct Mudtank zircon grains after microprobe work.** (**A**) ARM was applied and immediately after microprobe work was performed on this sample. We do not observe any difference between the value of the NRM and that immediately before ARM demagnetization providing evidence that the microprobe does not remagnetize or overprint the samples. (**B**) Same as (**A**), but this time we waited two days between ARM application, microprobe work and ARM demagnetization (black line). The blue line shows an example of ARM application, two-days waiting period and ARM demagnetization. The behavior of the two lines is very similar, providing further evidence that the microprobe does not remagnetize or overprint the NRM of the samples.

nA, and natural and synthetic standards were used for calibration. The counting times were typically 40 seconds per element, and the 1σ standard deviation of the accumulated counts were 0.5 to 1.0% from counting statistics. The raw data were corrected for matrix effects using the CITZAF package (Armstrong, 1995).

Prior to use the microprobe, we used test samples to establish if the microprobe would remagnetize CAIs priot to our paleomagnetic experiments, potentially eliminating any original natural remanent magnetization (NRM). To achieve this, we applied anhysteretic remanent magnetizations (ARMs) with AC fields of 2600 G and DC fields of 200 μT to zircon grains from Mudtank Australia (see Borlina et al. (2020) for more details of these samples). Fig. 3-2 shows the result of these experiments. Fig. 3-2A shows ARM application, followed by microprobe work, followed by ARM demagnetization. We observe no variation on the NRM value between initial application and after microprobe work. Fig. 3-2B shows ARM application followed by

microprobe work and ARM demagnetization after two days from the initial ARM application (black line). The decay between the initial ARM application and that measured two days after, following microprobe work, is similar to what is observed in that of an ARM application, followed by two days of waiting, and ARM demagnetization (blue). These observations suggest that conducting microprobe work prior to NRM demagnetization does not erase or overprint the potential NRM recorded in the samples.

We identified a total of 25 CAIs. Following the classification of Zhang et al. (2020), we observed 14 melilite-rich CAIs, 7 hibonite-bearing CAIs, 2 grossite-bearing CAIs and 2 pyroxene-anorthite CAIs. We selected five CAIs to conduct paleomagnetic studies with: CAI 6 (melilite-rich), CAI 10 (hibonite-bearing), CAI 11 (hibonite-bearing), CAI 18 (melilite-rich) and CAI 19 (melilite-rich). Fig. 3-3 shows the BSE images along with the WDS interpretation for all samples studied here. After identification, all CAIs were extracted following the procedures described in Borlina et al. (2021c). We also attempted to conduct an unidirectionality test with one of the CAIs. Because the nebular field is expected to have been directionally homogeneous on submillimeter length scales, a nebular TRM should be unidirectional within each CAI (Borlina et al., 2021c). For this test, we split CAI 18 into two subsamples, CAI 18a and CAI 18b, after extraction.

3.3.2 Paleomagnetism

We used alternating fields (AFs) to demagnetize the CAIs in steps of 5 mT, using an automatic 3-axis degausser system integrated into the 2G Enterprises Superconducting Rock Magnetometer 755R (Kirschvink et al., 2008) at MIT. We demagnetized the samples with repeated AF applications to reduce spurious ARM (Stephenson, 1993). The maximum AF field necessary to demagnetize the samples varied among our samples. Sample CAI 6 was demagnetized up to 145 mT, CAI 10 was demagnetized up to 100 mT, CAI 11 was demagnetized up to 105 mT, CAI 18a was demagnetized up to 225 mT, CAI 18b was demagnetized up to 70 mT and CAI 19 was demagnetized up to 145 mT. For each AF step, we measured the magnetic field of each sample three

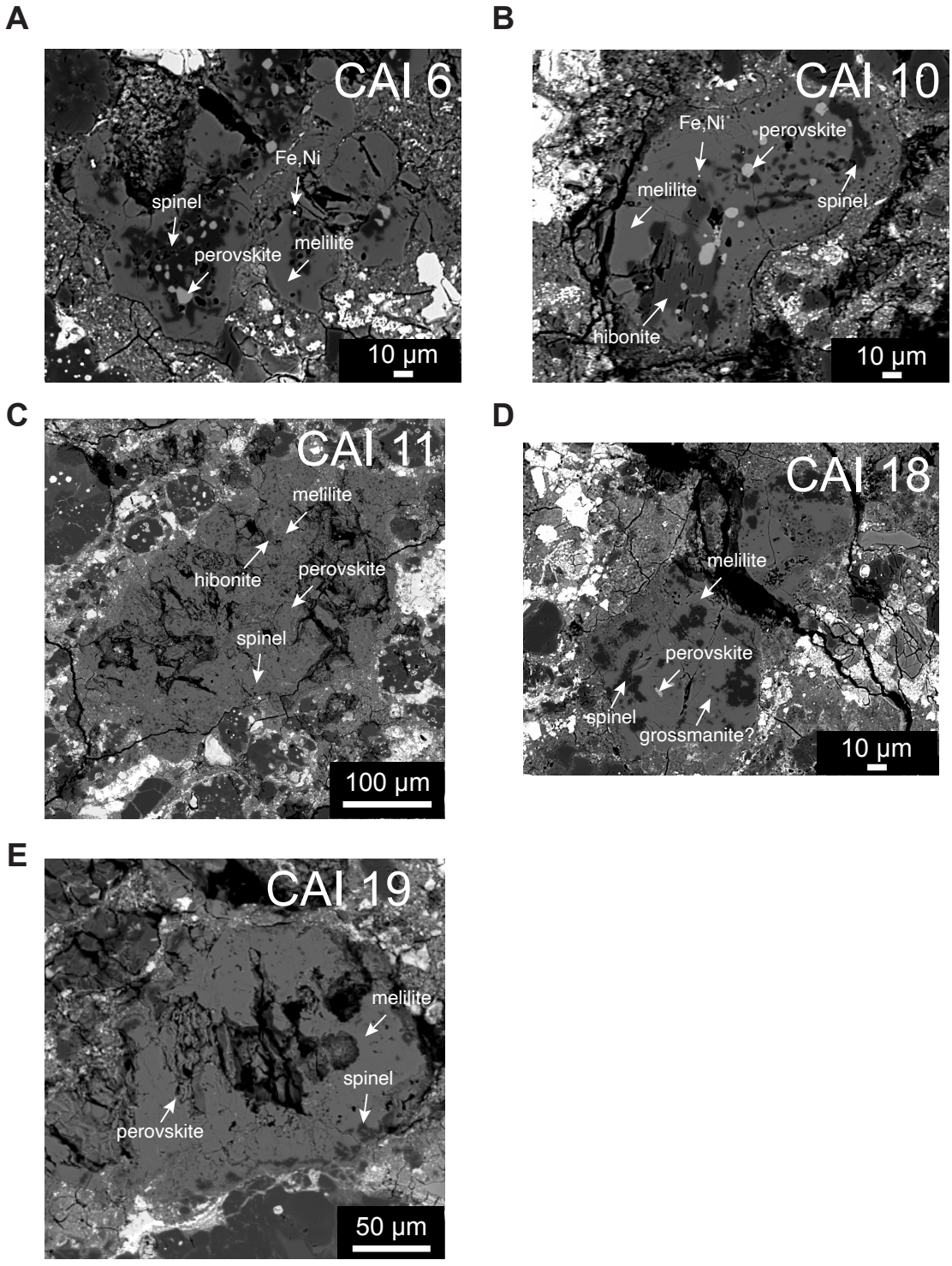

Figure 3-3: **BSE images and WDS interpretations for all CAIs used in this study**.(**A**) CAI 6 is a melilite-rich CAI. (**B**) CAI 10 is a hibonite-bearing CAI. (**C**) CAI 11 is a hibonite-bearing CAI. (**D**) CAI 18 is a melilite-rich CAI. (**E**) CAI 19 is a melilite-rich CAI.

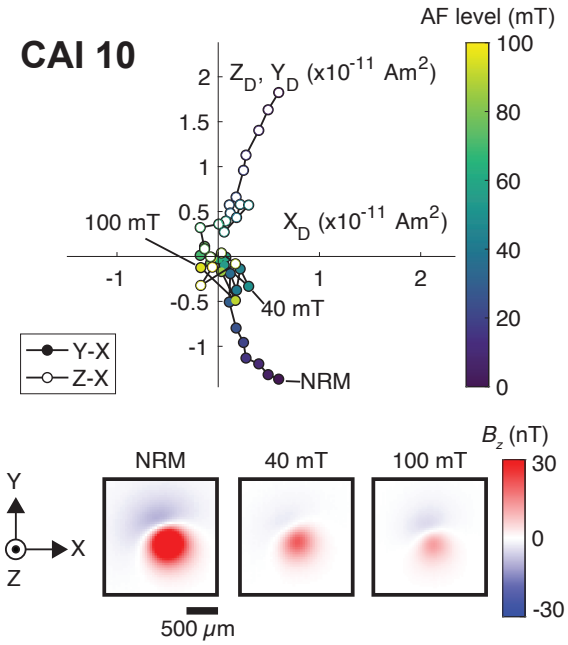

Figure 3-4: **AF demagnetization of CAI 10.** Orthographic projections of NRM vector endpoints during alternating field (AF) demagnetization showing averaged measurements for repeated AF steps. Closed symbols show the Y-X projection of the magnetic moment, and open symbols show Z-X projection of the magnetic moment. Selected demagnetization steps are labeled. Color scales show the AF levels. Out-of-the-page magnetic field component (B_z) maps for selected steps measured at a height of ∼300 μm above the chondrules obtained with the SQUID microscope. Each map represents one of three maps associated with different applications of the AF field to obtain each step shown in the orthographic projection.

times. Each measurements was conducted after applications of the AF in the X, Y, and Z directions.

NRM measurements were obtained using the superconducting quantum interference device (SQUID) microscope and the quantum diamond microscope (QDM) in the MIT Paleomagnetism Laboratory (Weiss et al., 2007; Glenn et al., 2017; Fu et al., 2020c). CAI 11 was measured with the QDM from 0-45 mT and from 45-105 mT with the SQUID microscope. All other samples were measured with the SQUID microscope only. Measurements of the samples' magnetic fields were obtained at an effective sensor-to-sample distance of ∼300 μm with the SQUID microscope and ∼30 μm with the QDM. Most sources were found to be dipolar and we used a previously described inversion technique to obtain the magnetic moment from the magnetic field

(Lima and Weiss, 2016; Fu et al., 2020c). We upward-continued non-dipolar maps and used the inversion technique described in Fu et al. (2020c) to obtain magnetic moments. After obtaining magnetic moments from each AF step, we averaged across the three repeated AF steps. The directions of NRM components were calculated using principal components analysis (Kirschvink, 1980). If a NRM component had a deviation angle less than the maximum angle deviation, then this component was inferred to be the characteristic component and therefore anchored to the origin (Kirschvink, 1980; Tauxe and Staudigel, 2004).

To obtain paleointensities, we used the ARM method (Fu et al., 2014; Tikoo et al., 2014; Borlina et al., 2021c) for which:

$$B_{paleo} = \frac{B_{lab}}{f'} \frac{\Delta NRM}{\Delta ARM} \tag{3.1}$$

where B_{paleo} is the ancient magnetic field recovered from the experiment, B_{lab} is the 200-μT ARM bias magnetic field applied to the sample, ΔNRM and ΔARM are the respective changes in magnetic moment during the demagnetization of the NRM and the ARM, and f' is the ratio of TRM to ARM. The ARM was applied with a peak AF field of 260 mT for all samples, except CAIs 11 (peak 105 mT) and 19 (peak 145 mT). We also demagnetized an ARM from CAI 19 with a bias field of 200 μT and peak AF field of 260 mT and we did not observe variations in the demagnetization behavior of this sample when compared to the that with a peak field of 145 mT. We AF demagnetized the ARM using the same sequence used for the NRM. All samples used for paleointensity determination were nearly dipolar sources, such that we used the inversion technique for dipolar sources described above. Because the only potential magnetic carriers in CAIs are likely to be Fe-Ni metal grains, we adopted an f' of 1.34 (Tikoo et al., 2014; Krot, 2019). Paleointensities fits followed the procedures described in Borlina et al. (2021c).

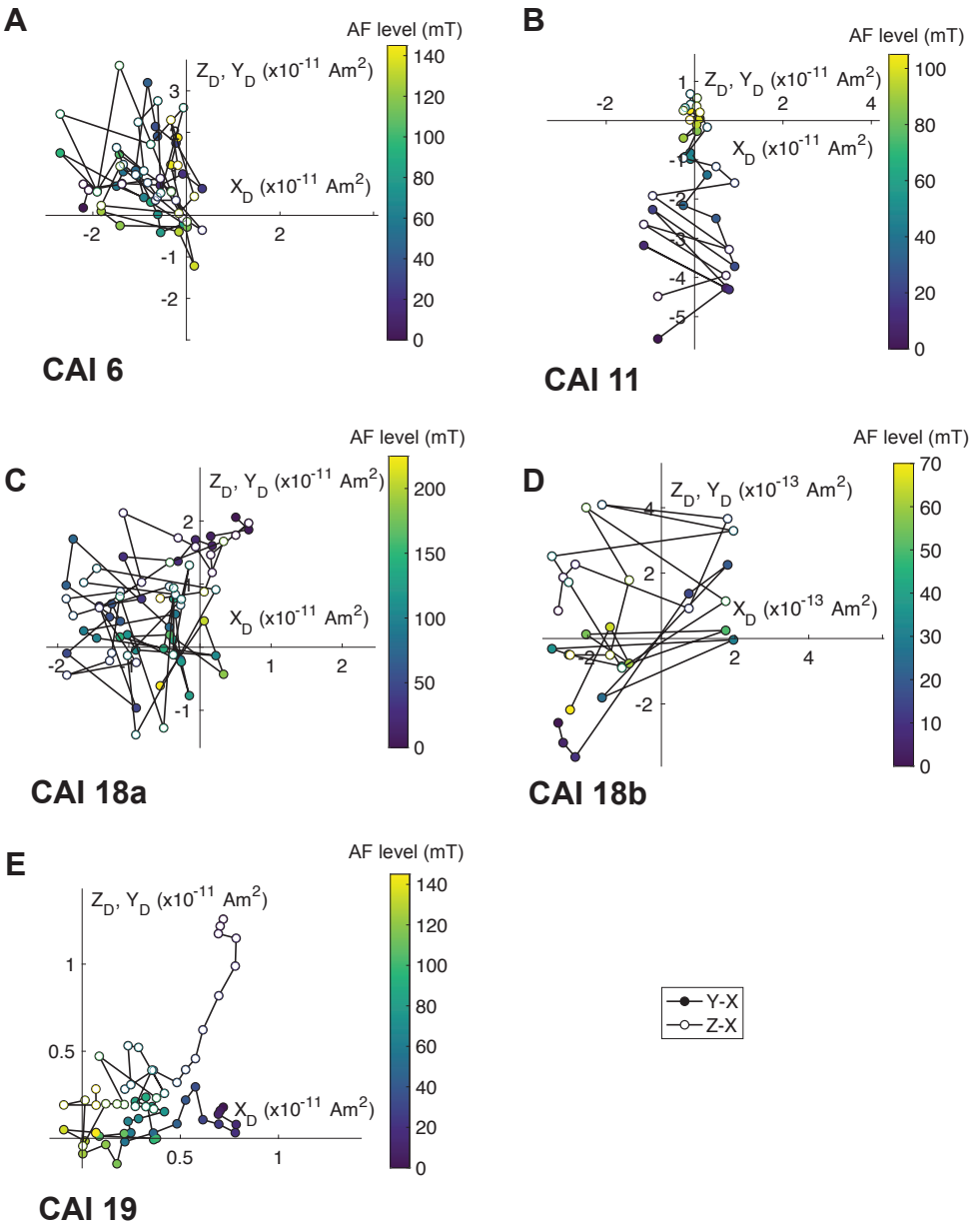

Figure 3-5: **AF demagnetization of CAIs** (**A**) CAI 6, (**B**) CAI 11, (**C**) CAI 18a, (**D**) CAI 18b and (**E**) CAI 19. Orthographic projections of NRM vector endpoints during alternating field (AF) demagnetization showing averaged measurements for repeated AF steps. Closed symbols show the Y-X projection of the magnetic moment, and open symbols show Z-X projection of the magnetic moment. Color scales show the AF levels.

3.4 Results

AF demagnetizations are shown in Figs. 3-4 and 3-5. Fig. 3-4 shows the NRM demagnetization of CAI 10 data along with SQUID microscope maps of selected steps. The remaining NRM demagnetizations are shown in Fig. 3-5. Table 3.1 shows the results of the principal components analysis. Overall, all CAIs, with the exception of CAI 11, show a low coercivity (LC) component that is completely removed by 30 mT. Three CAIs showed high coercivity (HC) components that were completely demagnetized by 145 mT. The remaining three CAIs did not have HC components. Fig. 3-6 show the LC and HC components of the CAIs (red) including maximum deviation angles. In the HC plot, faded red datapoints indicate the fits from the non-magnetized components. Directions from dusty olivine chondrules obtained from Borlina et al. (2021c) are presented in black. The random direction of the HC components presented in Fig. 3-6 further support that that these inclusions were not remagnetized since accretion to the parent-body. In fact, a conglomerate test that included both CAIs and dusty olivine chondrules, in total seven samples, indicates that we cannot reject the hypothesis that both sets of directions are random with 95% confidence, since the length of the resultant vectors is 0.46, which is less than that of the critical length of 4.13 for 7 samples (Watson, 1956; Borlina et al., 2021c). An unidirectionality test conducted with CAI 18 turned out to be inconclusive since this particular sample did not record a component. Nonetheless, the fact that the HC components from CAI 18a and CAI 18b are non-magnetized suggest that both subsamples could have experienced the same field conditions during acquisition of the TRM.

We obtained paleointensities from all CAIs (Figs. 3-7 and 3-8; Table 3.3). CAIs 10, 11 and 19 recorded a mean field of 73.9 ± 11.3 μT. If accounted for spinning during acquisition of the magnetization, we have a magnetic field record of $147.7 \pm 22.7\mu$T. For the CAIs that we did not observe HC components (CAI 6, CAI 18a and CAI 18b) we conducted repeated ARM acquisitions to establish the weakest magnetic field that they could record. These acquisitions are presented in Fig. 3-10 and the upper limits

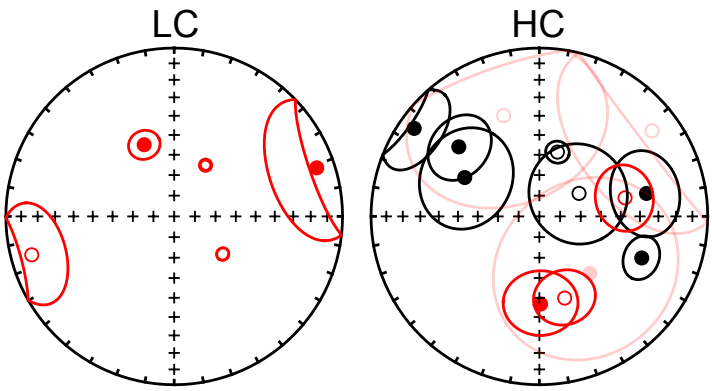

Figure 3-6: **Direction of the LC and HC components of CAIs.** Shown are equal area stereographic projections containing directions calculated from principal components analysis and their corresponding maximum angular deviations. Red datapoints show directions from CAIs and black datapoints show directions from dusty olivine chondrules from Borlina et al. (2021c). Shaded red datapoints show principal component analysis for non-magnetized ranges of the CAIs. The scattered HC directions from different chondrules and CAIs indicate that the meteorites were not remagnetized since the inclusions accreted to the parent-body.

of the magnetic field recorded by the CAIs that they provide is summarized in Table 3.3. Measurements of ARM acquisitions of CAI 6 suggest an upper limit of ∼100 μT, while the same acquisitions for subsamples of CAI 18 suggest an upper limit of ∼20 μT. Both of these values include a correction for spinning during acquisition of the magnetic field. The observation that both subsamples of CAI 18 record the same upper limit to the field further suggest that they experienced the same field conditions during acquisition of the TRM.

3.5 Discussion

The distribution of magnetic fields recorded by the CAIs could favor a diversity of mechanisms and locations for CAI formation. Nonetheless, conducting a Kolmogorov-Smirnov test with the paleointensities and assuming the upper limits of CAIs 6, 18a and 18b, we cannot reject the hypothesis that these paleointensities come from a normal distribution. This suggests that the spread in paleointensities among CAIs could come from a normal distribution of paleointensities across the mean solar nebula

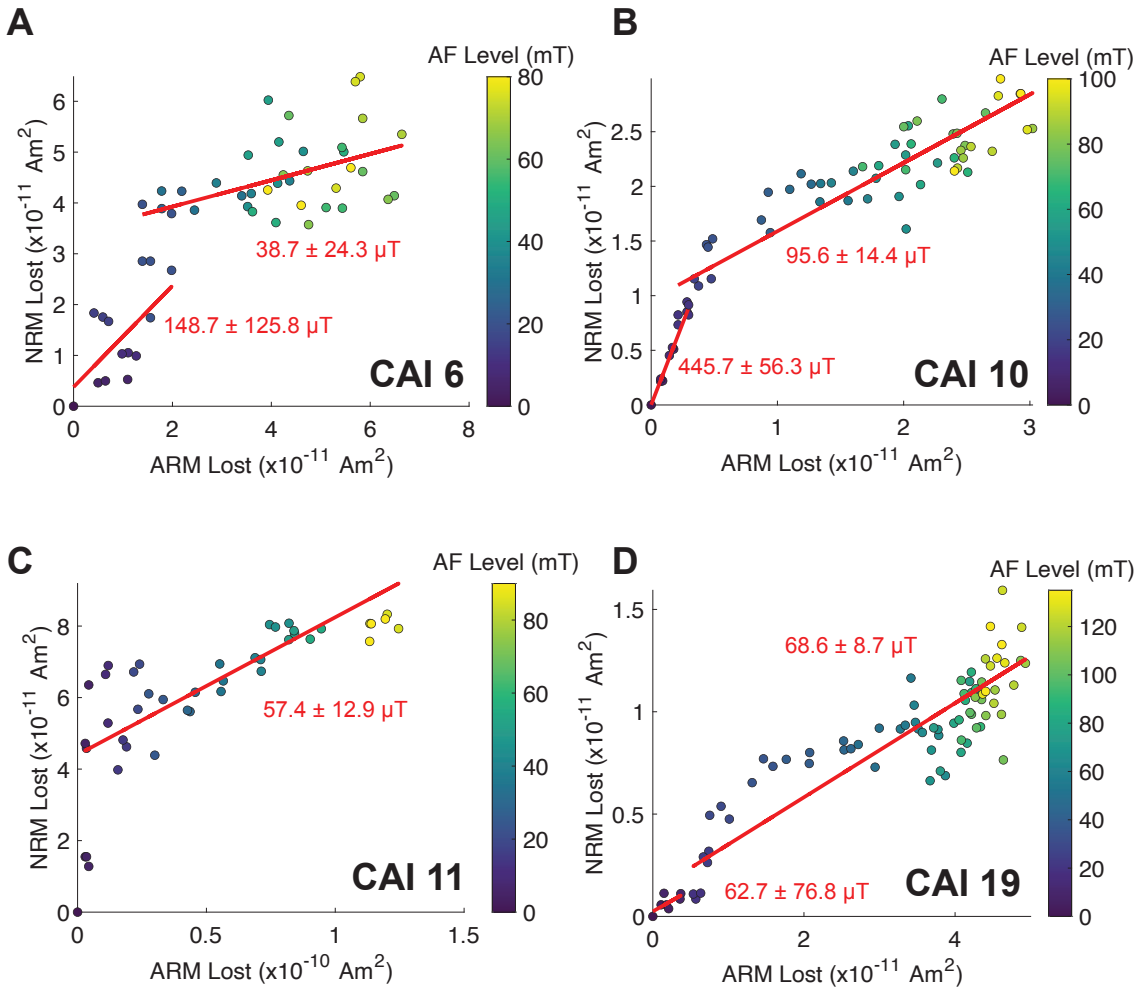

Figure 3-7: **Paleointensity experiments of CAIs 6, 10, 11 and 19**. Shown are NRM lost versus ARM lost during AF demagnetization of CAIs. (**A**) CAI 6. (**B**) CAI 10. (**C**) CAI 11. (**D**) CAI 19. Red line shows the least squares fit over the coercivity range used to calculate the paleointensity.

field, resulting from the distribution of spin axis directions of CAIs during acquisition of the magnetic field (Fu et al., 2014).

Focusing on the paleointensities recorded in CAIs 10, 11 and 19, they suggest that a mean field of 147.7 ± 22.7 μT was present at the time of their record acquisition. During this early phase, the proto-Sun was likely to be a Class 0 or 1 Young Stellar Object with accretion rates that fluctuated within a few to 10^5 years (Krot, 2019; Brennecka et al., 2020; Audard et al., 2014). In Fig. 3-10, we compare our measurements with models that describe how magnetic fields under different configurations

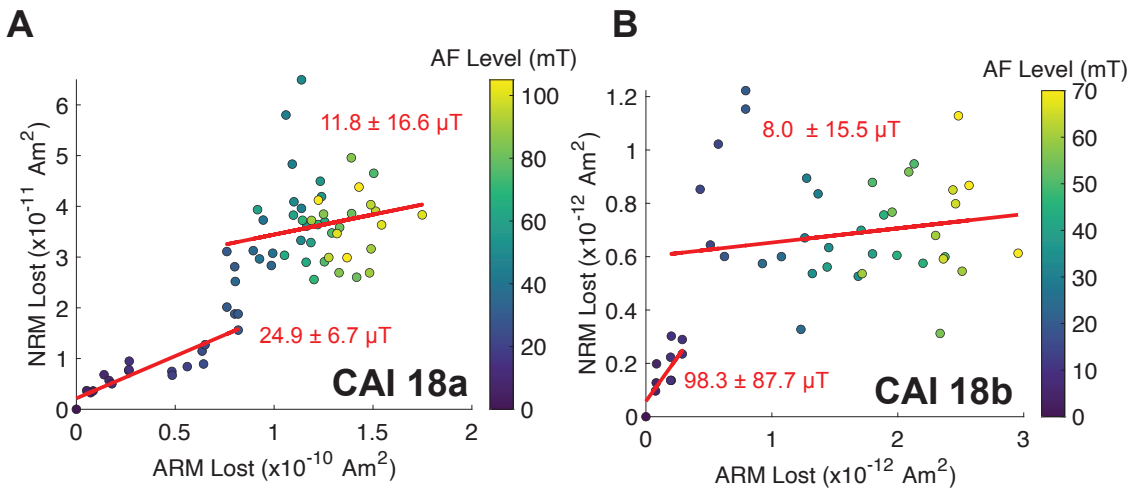

Figure 3-8: **Paleointensity experiments of CAIs 18a and 18b**. Shown are NRM lost versus ARM lost during AF demagnetization of CAIs. (**A**) CAI 18a. (**B**) CAI 18b. Red line shows the least squares fit over the coercivity range used to calculate the paleointensity.

are expected to scale with radius in the early solar system. For a spatially constant accretion rate, the field intensity should decay as $\sim$R$^{-5/4}$ or $\sim$R$^{-11/8}$, where R is the radial distance from the Sun, depending on whether accretion is primarily driven by the radial-toroidal ($R\varphi$) or vertical-toroidal ($z\varphi$) components of the Maxwell stress (Fig. 3-10) (Weiss et al., 2021). We assumed two accretion rates for these models: one typical of class 0-1 objects of $\sim 10^{-6}$ $M_{\odot}$ year^{-1} (Cieza et al., 2016) and another one of $\sim 10^{-4}$ $M_{\odot}$ year^{-1} typical of an outburst by class 0-1 objects (Audard et al., 2014). We highlight that these models assume that nebular fields decay smoothly, an assumption that has been questioned a few Ma later in the lifetime of the solar nebula (Borlina et al., 2021c; Fu et al., 2021).

Because of the fluctuation in accretion rate associated with Young Stellar Objects outbursts, we have to determine how fast the magnetic records were acquired during CAI formation. A longer cooling rate might suggest that these records are time-averages of the field, while a shorter cooling rate might indicate an instantaneous record. The cooling rates of the different types CAIs found in CO chondrites have not been determined, however we can use the experimentally determined cooling

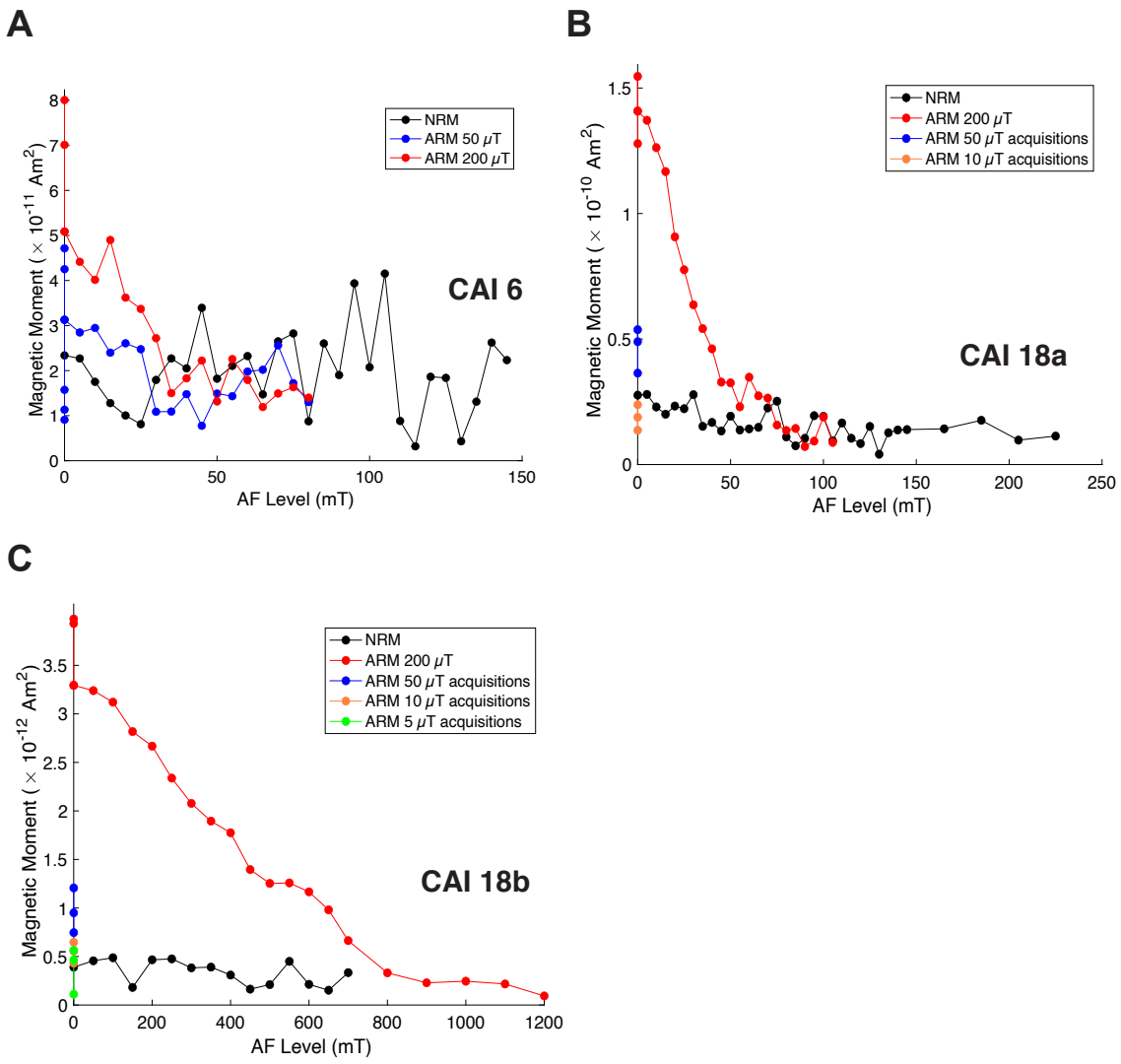

Figure 3-9: **NRM and ARM demagnetizations and multiple ARM acquisitions at different bias levels for CAIs 6, 18a and 18b.** AF demagnetization of NRM and 200 μT-ARM are shown for (**A**) CAI 6, (**B**) CAI 18b and (**C**) CAI 18b. ARM acquisitions at biases levels of 200 and 50 μT are shown for (**A**) CAI 6, ARM acquisitions at biases levels of 200, 50 and 10 μT are shown for (**B**) CAI 18a and ARM acquisitions at biases levels of 200, 50, 10 and 5 μT are shown for (**C**) CAI 18b.

rate of type B CAIs of $\sim 10^{o}$C hr^{-1} as a baseline for that of CAIs from CO chondrites (Richter et al., 2002; Simon et al., 2019). This cooling rate would suggest that if CAIs cooled below the Curie temperature of kamacite of $\sim$760 ^{o}C, or $\sim$1033 K, the magnetic record would have been acquired over several days, suggesting an instantaneous record of the nebular field. We note that the midplane temperatures of the disk are likely

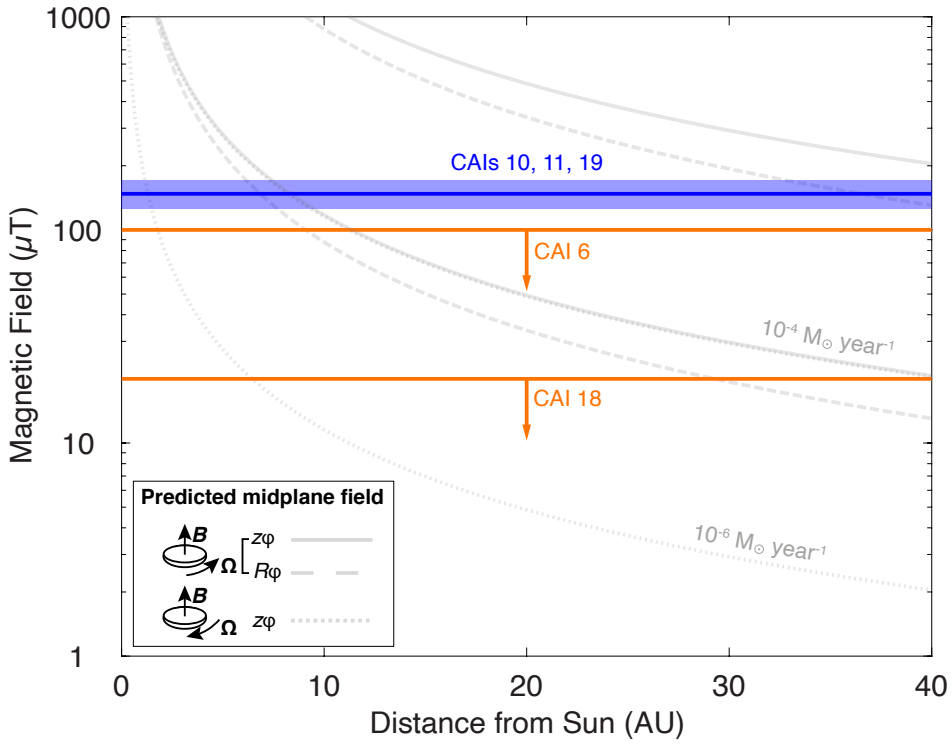

Figure 3-10: **Comparison between paleomagnetic constraints and model predictions for the solar nebula magnetic field intensity.** Shown are paleointensity records obtained in these study. Blue line shows the mean paleointensity and 95% confidence error from the CAIs 10, 11 and 19. Orange lines shows the upper limits of CAIs 6 and 18. Solid and dashed lines show predicted midplane magnetic field, due to vertical-toroidal [$z\varphi$; equation 3 of Weiss et al. (2021)] and radial-toroidal [$R\varphi$; equation 2 of Weiss et al. (2021)] Maxwell stresses, respectively, assuming the nebular magnetic field and sense of disk rotation are aligned. Dotted lines show the field due to vertical-toroidal Maxwell stresses [$z\varphi$; equation 3 of Weiss et al. (2021)] assuming the nebular magnetic field and sense of disk rotation are antialigned. Top and bottom curves were calculated assuming accretion rates of 10^{-4} and 10^{-6} $M_\odot$ year^{-1} respectively.

to be below that of the Curie temperature of kamacite for most regions of the disk (Wood, 2000; Weiss et al., 2021). We discuss below how outbursts could change the temperature of the disk.

Comparing our measurements with the models from Fig. 3-10, the magnetic records of CAIs were likely acquired in the >1.3 AU. In fact, previous magnetic measurements suggest that the solar nebula was in an aligned configuration (Borlina et al., 2021c). Under this configuration, CAIs would have acquired their magnetic

record >8 AU.

There are two main scenarios that could explain acquiring a magnetic record from >8 AU. In scenario (1), CAIs formed and cooled below the Curie temperature of kamacite somewhere >8 AU from the proto-Sun. This scenario is unlikely because the beryllium and oxygen isotopic systematics, and the redox state of pyroxenes of CAIs point to refractory inclusions forming close to the proto-Sun, much less than 8 AU (MacPherson et al., 2005; McKeegan et al., 2000; Krot, 2019; Righter et al., 2016) rather than close to proto-Jupiter. In scenario (2), CAIs could have formed and potentially cooled below the Curie temperature of kamacite close to the proto-Sun, transported to the >8 AU region and re-heated above the Curie temperature of kamacite during transport, acquiring a magnetic record from the >8 AU region. This scenario is consistent with formation through magnetized disk winds, which could have operational in the 1-10 AU region, forming and/or transporting CAIs in the early solar system (Salmeron and Ireland, 2012).

An adapted version of Scenario (2) includes the variation in temperatures associated with Young Stellar Object outbursts. Observations of how outbursts of Young Stellar Object affect the water snow-line in protoplanetary disks indicate that outburst can move the water snow-line of a system with a Young Stellar Object of $1.3 M_{\odot}$ to ∼42 AU (Cieza et al., 2016). This suggests that CAIs could have been transported outwards through a mechanism that might not heat the inclusions above the Curie temperature of kamacite, but temperature fluctuations in the disk associated with the proto-Sun could increase the temperature of the disk above that of the Curie temperature of kamacite. The magnetic record would have been acquired when the disk cools down below the Curie temperature of kamacite.

Overall, our paleomagnetic measurements are consistent with CAIs forming within and/or being heated due to magnetically-driven disk winds and outbursts, acquiring a magnetization from their settling location, in the >8 AU region. This interpretation does not preclude that CAIs could have formed through other mechanisms.

3.6 Conclusion

We present here the first comprehensive paleomagnetic study of CAIs from CO chondrites to investigate the magnetism of the solar nebula during the very beginning of the solar system. We conducted paleomagnetic measurements with six CAIs, with three of them showing records of the nebula field with an average intensity of 147.7 $\pm$ 22.7 μT, while the other three (two of them being subsamples from one CAI) place upper limits on the nebular field of 10-20 μT. When coupled with models that predict what the expected decay of the protoplanetary disk should be during the time the disk is Class 0-1, we observe that CAIs acquired their magnetic record >8 AU. This record is consistent with formation/heating due to magnetically-driven winds and/or stellar outbursts.

Table 3.1: **Summary of components from AF demagnetization of CAIs.** The first column lists the sample name, the second column lists the name of the component (LC for low coercivity and HC for high coercivity), the third column lists the range used to calculate the fit in mT, the fourth, fifth and sixth columns show the results of the principal component analysis which includes the declination, inclination and maximum angle deviation (MAD), the seventh column lists the deviation angle (DANG) for the component, the eighteenth column denotes whether the component is anchored (Y for yes and N for no).

Sample	Component	Range (mT)	Declination (°)	Inclination (°)	MAD (°)	DANG (°)	Anchored?
CAI 6	LC	0-20	254.9	-13.4	19.8	-	-
	HC*	20-145	138.4	52.7	45.3	-	N
CAI 10	LC	0-15	127.8	-60.1	2.9	-	-
	HC	15-85	162.8	-47.9	14.1	16.7	Y
CAI 11	HC	0-90	179.2	46.8	16.8	18.2	N
CAI 18a	LC	0-30	71.2	11.5	27.5	-	-
	HC*	30-105	340.5	-36.6	45.3	-	N
	HC*(?)	30-225	66.8	-72.1	45.3	-	N
CAI 18b	LC	0-10	337.3	51.9	7.3	-	-
	HC*	10-70	52.8	-17.1	42.1	-	N
CAI 19	LC	0-10	31.5	-60.8	2.5		-
	HC	20-135	77.8	-46.8	15	2.2	Y

Table 3.2: **Summary of paleointensities from AF demagnetization of CAIs.** The first column lists the sample name, the second column lists the name of the component (LC for low coercivity and HC for high coercivity), the third column lists the range used to calculate the fit in mT, the fourth column shows the number of datapoints used to calculate the fit, fifth and sixth columns show the calculated paleointensity and the 95% confidence interval of the paleointensity, and the seventh column shows the fit used to calculate the paleointensity where OLS for ordinary least square and RMA reduced major axis.

Sample	Component	Range (mT)	N	Paleointensity (μT)	95% Confidence Interval (μT)	Fit
CAI 6	LC	0-20	13	148.7	125.8	OLS
	HC	20-80	38	38.7	24.3	OLS
CAI 10	LC	0-15	10	445.7	56.3	OLS
	HC	15-85	45	95.6	14.4	RMA
CAI 11	LC	0-5	4	852.5	3900	OLS
	HC	5-90	38	57.4	12.9	RMA
CAI 18a	LC	0-30	19	24.9	6.7	OLS
	HC	30-105	48	11.8	16.6	OLS
CAI 18b	LC	0-10	7	98.3	87.7	OLS
	HC	10-70	39	8	15.5	OLS
CAI 19	LC	0-10	7	62.7	76.8	OLS
	HC	20-135	72	68.6	8.7	RMA

Table 3.3: **Summary of high-coercivity paleointensities and upper limits from AF demagnetization of CAIs.** The first column lists the sample name, the second column lists the range used to calculate the fit in mT, the third and fourth columns show the calculated paleointensity and the 95% confidence interval of the paleointensity, and the fifth column shows the corrected paleointensity for each CAI.

Sample	Range (mT)	Paleointensity (μT)	95% Confidence Interval (μT)	Corrected Paleointensity (μT)
CAI 6	20-80	$<$50	-	$<$100
CAI 10	15-85	95.6	14.4	191.2
CAI 11	5-90	57.4	12.9	114.8
CAI 18a	30-105	$\lesssim$10	-	$\lesssim$20
CAI 18b	10-70	$\lesssim$10	-	$\lesssim$20
CAI 19	20-135	68.6	8.7	137.2

Chapter 4

Paleomagnetism of Dusty Olivine Chondrules from CO Chondrites

4.1 Chapter Introduction

Astronomical observations and isotopic measurements of meteorites suggest that sub-structures are common in protoplanetary disks and may even have existed in the solar nebula. Here, we conduct paleomagnetic measurements of chondrules in CO carbonaceous chondrites to investigate the existence and nature of these disk sub-structures. We show that the paleomagnetism of chondrules in CO carbonaceous chondrites indicates the presence of a 101 $\pm$ 48 μT field in the solar nebula in the outer solar system ($\sim$3 to 7 AU from the Sun). The high intensity of this field relative to that inferred from inner solar system ($\lesssim$3 AU) meteorites indicates a factor of $\sim$5 to 150 mismatch in nebular accretion between the two reservoirs. This suggests substantial mass loss from the disk associated with a major disk substructure, possibly due to a magnetized disk wind.

4.2 Introduction

Observations from the Atacama Large Millimeter/submillimeter Array have shown that substructures, mostly in the form of rings and gaps, are prevalent in protoplanetary disks (Andrews, 2020). Isotopic studies of meteorites and their components have been interpreted as evidence that two isotopically distinct regions existed within ∼7 astronomical units (AU) from the young Sun (see the Supplementary Materials), known as the noncarbonaceous (<3 AU) and carbonaceous reservoirs (3 to 7 AU) (Kruijer et al., 2020; Scott et al., 2018), that existed during the protoplanetary disk phase of the solar system (i.e., solar nebula). It has been proposed that these two reservoirs were separated by a gap in the disk, perhaps generated by the growth of Jupiter (Kleine et al., 2020) and/or a pressure local maximum in the disk (Brasser and Mojzsis, 2020). Alternatively, these two reservoirs may have formed because of a migrating snowline with no persistent disk gap (Lichtenberg et al., 2021). Because the evolution of protoplanetary disks is thought to depend on the coupling of the weakly ionized gas of the disk with large-scale magnetic fields (Bai and Goodman, 2009; Bai, 2017; Turner et al., 2014; Weiss et al., 2021), we can search for evidence of disk substructures and explore their origin by studying the paleomagnetism of meteorites that formed in each reservoir.

Previous paleomagnetic measurements of LL chondrites, derived from the noncarbonaceous reservoir, indicate the presence of a disk midplane magnetic field of 54 ± 21 μT at 2.0 ± 0.8 million years (Ma) after the formation of calcium-aluminum–rich inclusion (CAIs) (Fu et al., 2014; Kita and Ushikubo, 2011). These paleointensities, which were measured from individual chondrules that carry thermoremanent magnetization (TRM) acquired before their accretion onto the LL parent body, provide evidence for the existence of a nebular magnetic field in the noncarbonaceous reservoir. Paleomagnetic studies of CM (Cournede et al., 2015), CR (Fu et al., 2020b), and CV (Fu et al., 2021) chondrites indicate a field in the carbonaceous reservoir of >6 μT at ∼3 Ma after CAI formation, <8 μT at ∼3.7 Ma after CAI formation (Weiss et al., 2021; Schrader et al., 2017), and ≥40 μT sometime between ∼3-40 Ma

after CAI formation (Fu et al., 2021; Carporzen et al., 2011). However, these records have several key limitations. For instance, the records in CM and CV chondrites are postaccretional chemical remanent magnetizations acquired during parent-body alteration (Cournede et al., 2015). This poses two problems: The magnetic record could have been imparted by a parent-body dynamo field rather than from the solar nebula field and the retrieved paleointensity is likely a lower limit (Weiss et al., 2021). In addition, the age of the CR record is within error of the estimated lifetime of nebula (Wang et al., 2017), such that it may not constrain the strength of the nebular field during the main period of disk accretion (Weiss et al., 2021). Therefore, the intensity of the nebular field in the carbonaceous reservoir is currently poorly constrained.

To obtain robust paleointensity records from the midplane of the solar nebula in the carbonaceous reservoir, we conducted paleomagnetic studies on two CO carbonaceous chondrites: Allan Hills (ALH) A77307 (type 3.03) and Dominion Range (DOM) 08006 (type 3.00) (Bonal et al., 2007; Davidson et al., 2019; Alexander et al., 2018; Scott et al., 1992; Alexander et al., 2007). We selected these meteorites because they experienced low peak metamorphic temperatures (200° to 300°C), minor parent-body aqueous alteration, shock pressures below 5 GPa, and minimal terrestrial weathering (weathering grades A/B and Ae, respectively) (Bonal et al., 2007; Davidson et al., 2019; Alexander et al., 2018; Scott et al., 1992; Alexander et al., 2007). Therefore, they are unlikely to have been magnetically overprinted following accretion onto the CO parent body, with DOM 08006 in particular being one of the least altered known meteorites (Davidson et al., 2019). Following the previous paleomagnetic study of LL chondrules, we targeted dusty olivine chondrules because they contain high-fidelity paleomagnetic recorders in the form of fine-grained (∼25 to 1000 nm) kamacite (α-Fe) crystals formed before accretion onto the parent body (Fu et al., 2014; Shah et al., 2018; Einsle et al., 2016; Lappe et al., 2011, 2013). Because chondrules cooled quickly in the protoplanetary disk environment [100° to 1000°C hour^{-1}; (Scott and Krot, 2013)], they should carry a near-instantaneous TRM record of the nebular field (Fu et al., 2014; Desch et al., 2012, 2010). Al-Mg dating of CO chondrules indicate that this record was acquired 2.2 ± 0.8 Ma after CAI formation (Kita and Ushikubo,

2011)[1].

We extracted six 100- to 300-μm-diameter dusty olivine chondrules from both meteorites: two from ALHA77307 (DOC1 and DOC2) and four from DOM 08006 (DOC3, DOC4, DOC5, and DOC6). Three of the DOM 08006 chondrules were split into two subsamples each (DOC3a, DOC3b, DOC5a, DOC5b, and DOC6a, DOC6b) to produce nine total subsamples from both meteorites used for paleomagnetic measurements. All chondrules and chondrule fragments were mutually oriented during extraction and paleomagnetic measurements.

Given the chondrules' weak natural remanent magnetization (NRM) (ranging from 1.3×10^{-10} down to 1.7×10^{-12} Am^2 before demagnetization), we obtained magnetic measurements using the superconducting quantum interference device (SQUID) microscope and quantum diamond microscope (QDM) in the Massachusetts Institute of Technology (MIT) Paleomagnetism Laboratory (see Materials and Methods) (Weiss et al., 2007).

4.3 Methodology

4.3.1 Chondrule extraction and orientation

Bulk samples of ALHA77307,157 (0.57 g) and DOM 08006,102 (2.8 g) were obtained from the NASA Johnson Space Center. At MIT, oriented thick sections were cut from these using a wire saw cooled with ethanol during cutting. Each thick section had an average area of 4 cm^2 and a thickness of $\sim$500 μm. The thick sections were then polished down to 1-μm roughness, and dusty olivine chondrules were identified using reflected light microscopy. Overall, we found that dusty olivine chondrules are very rare among CO chondrites, with a frequency of only $\sim$1 out of 100 chondrules ($\sim$0.005 inclusion mm^{-3}). The six dusty olivine chondrules used in this study were obtained from two thick sections from ALHA77307 and eight from DOM 08006. We note that some thick sections did not contain identifiable dusty olivine chondrules.

[1]Recent high-precision Al-Mg ages of LL chondrules support a shorter formation interval than previous Al-Mg ages. See Supplementary Text for more information.

All extracted chondrules were at least 3 mm away from the fusion crust of the parent sample (table S1).

Figure S1 shows the procedure for chondrule extraction. Before extraction, the thick section surface orientation was documented using imaging with a petrographic microscope (step 1, fig. S1). A region of ∼300 to 500 μm in thickness was excavated around the target chondrule using a degaussed carbide dental drill bit (step 2, fig. S1). After excavation, we used two different techniques to extract the chondrules. In the first technique, chondrule samples DOC1, DOC2, DOC3a, and DOC3b were extracted using a degaussed dental drill then glued to the quartz disk using cyanoacrylate cement. While the glue hardened, we oriented the sample by comparing its surface with the previously acquired image of the chondrule in situ. In the second technique, chondrule samples DOC4, DOC5a, DOC5b, DOC6a, and DOC6b each had a ∼400 μm by 400 μm by 1000 μm non-magnetic quartz glass coverslip glued with cyanoacrylate cement onto their top surfaces (step 3, fig. S1). We then marked the glass with a marker to orient it with respect to the thick section. The chondrules were then extracted using a degaussed dental drill bit and mounted on a quartz glass with cyanoacrylate cement. After extraction, we added Kapton tape as standoffs that were at least 2 mm away from the samples (step 4, fig. S1). The standoffs were added such that they were slightly higher than the samples, protecting the samples from rubbing against the SQUID microscope window during the magnetic measurements. Table S1 shows the orientations of the chondrules during the SQUID microscope measurements. We estimate that the extraction and mounting techniques can add up to 15° of total angular uncertainty.

4.3.2 Paleomagnetism

We used AFs to demagnetize the chondrules in steps of 5 or 10 mT, using an automatic 3-axis degausser system integrated into the 2G Enterprises Superconducting Rock Magnetometer 755R (Kirschvink et al., 2008) at MIT. We demagnetized the samples with repeated AF applications to reduce spurious ARM and used the Zijderveld-Dunlop averaging method to correct for gyroremanent magnetization (Stephenson,

1993). The maximum AF field necessary to demagnetize the samples varied among our samples. Sample DOC1 was demagnetized up to 400 mT, DOC2 up to 410 mT, DOC3a up to 100 mT, DOC3b up to 60 mT, DOC4 up to 100 mT, DOC5a up to 60 mT, DOC5b up to 75 mT, DOC6a up to 70 mT, and DOC6b up to 100 mT. For each AF step, we measured the magnetic field of each sample six times: once after applications of the AF in the X, Y, and Z directions successively, twice after applications in the X direction, twice after applications in the Y direction, and once after an application in the Z direction.

NRM measurements were obtained using the SQUID microscope in the MIT Paleomagnetism Laboratory (Weiss et al., 2007). Measurements of the samples' magnetic fields were obtained at an effective sensor-to-sample distance of $\sim$300 μm (Weiss et al., 2007). For samples found to be dipolar magnetic field sources (DOC1, DOC2, DOC3a, DOC3b, DOC4, DOC5b, and DOC6b), we used a previously described inversion technique to obtain the magnetic moment from the magnetic field (Lima and Weiss, 2016). For samples DOC5a and DOC6a, whose fields were found to be nondipolar, we upward-continued the magnetic maps by 150 μm and retrieved their dipole moments using averages from a first- to the fifth- and second-degree multipole model, respectively. After obtaining magnetic moments from each AF step, we averaged across the six steps and sometimes also across AF levels. The directions of NRM components were calculated using principal components analysis (Kirschvink, 1980). The demagnetization projections are shown in figs. S2 and S3. If a NRM component had a deviation angle less than the maximum angle deviation, then this component was inferred to be the characteristic component and therefore anchored to the origin (Kirschvink, 1980; Tauxe and Staudigel, 2004). Table S1 shows the results of the principal components analysis including the levels that were averaged.

To obtain paleointensities, we used the ARM method (Fu et al., 2014; Tikoo et al., 2014) for which:

$$B_{paleo} = \frac{B_{lab}}{f'} \frac{\Delta NRM}{\Delta ARM} \tag{4.1}$$

where B_{paleo} is the ancient magnetic field recovered from the experiment, B_{lab} is the 200-μT ARM bias magnetic field applied to the sample, ΔNRM and ΔARM are the respective changes in magnetic moment during the demagnetization of the NRM and the ARM, and f' is the ratio of TRM to ARM. The ARM was applied with a peak AF field of 145 mT for DOC1 and DOC2, 100 mT for DOC3a, 60 mT for DOC3b, 100 mT for DOC4, 75 mT for DOC5b, and 100 mT for DOC6b. We AF demagnetized the ARM using the same sequence used for the NRM. All samples used for paleointensity determination were nearly dipolar sources, such that we used the inversion technique for dipolar sources described above. Following previous paleomagnetic studies of dusty olivine chondrules, we adopted an experimentally determined value for f' of 1.87 (Fu et al., 2014; Lappe et al., 2013).

Figures S5 and S6 show the results of the paleointensity experiments. For all samples except DOC3a, we fit for $\Delta NRM/\Delta ARM$ using reduced major axis least squares. For DOC3a, we used ordinary least squares because the correlation parameter was <0.6 (Smith, 2009). ΔNRM was calculated by vector subtraction from the first demagnetization step in the HC component fit, while ΔARM was calculated by subtraction from the first acquired ARM step. Table S5 shows a summary of the paleointensities and their quality criteria.

4.3.3 Mineralogy

Mineral compositions (fig. S4 and tables S3 and S4) were analyzed on a JEOL JXA-8200 Superprobe electron probe microanalyzer (EPMA) using WDS in the MIT Electron Microprobe Facility. BSE images were obtained with the same instrument (fig. S4). The EPMA was operated at an accelerating voltage of 15 kV and a beam current of 10 nA, and natural and synthetic standards were used for calibration. The counting times were typically 40 s per element, and the 1σ SDs of the accumulated counts were 0.5 to 1.0% from counting statistics. The raw data were corrected for matrix effects using the CITZAF package (Armstrong, 1995). To identify the origin of the magnetic signal of these two samples, we mapped the magnetization of chondrules using the QDM at MIT (fig. S4) (Fu et al., 2020c; Glenn et al., 2017). The sensor to

sample distance was ∼5 μm, and the map resolution was 1.17 μm. The QDM maps were obtained after the demagnetization of an ARM applied to DOC2 (200 μT bias with an AF of 145 mT) to 145 mT (fig. S4C) and after the application of an ARM (200 μT bias with an AF of 100 mT) to DOC6b (fig. S4F).

4.4 Results

Backscattered electron microscopy (BSE) images and compositional analysis using wavelength dispersive spectrometry (WDS) indicate that the chondrules contain numerous submicrometer diameter inclusions of nearly pure-Fe kamacite (see the Supplementary Materials). Furthermore, QDM imaging confirms that the magnetization-carrying capacity of the chondrules is dominated by these grains rather than by any multidomain metal grains and/or secondary ferromagnetic minerals (see the Supplementary Materials). These fine metal grains are expected to have formed during subsolidus reduction of the chondrules before their accretion on the parent body (Lappe et al., 2011). On the basis of their size and composition, many of these grains are predicted to be in the single vortex size range and smaller, which has been shown to have the potential to carry paleomagnetic records over a period longer than the lifetime of the solar system (Fu et al., 2014; Nagy et al., 2019a).

Our alternating field (AF) demagnetization showed that some subsamples carried a low-coercivity (LC) component blocked up to <20 mT (Fig. 4-1 and figs. S2 and S3). The LC component may be a viscous remanent magnetization acquired on Earth and/or a weak-field isothermal remanent magnetization acquired during sample handling. After the removal of the LC component, all subsamples were found to contain high-coercivity (HC) components blocked up to at least 50 mT (Fig. 4-1 , figs. S2 and S3, and table S1), with two subsamples having HC components blocked up to 160 and 270 mT (Fig. 4-1 and fig. S2).

The high AF-stability of the HC components coupled with the pristine conditions of the meteorites suggest that the HC components are likely records of the nebular field. To further test this conclusion, we conducted unidirectionality tests and

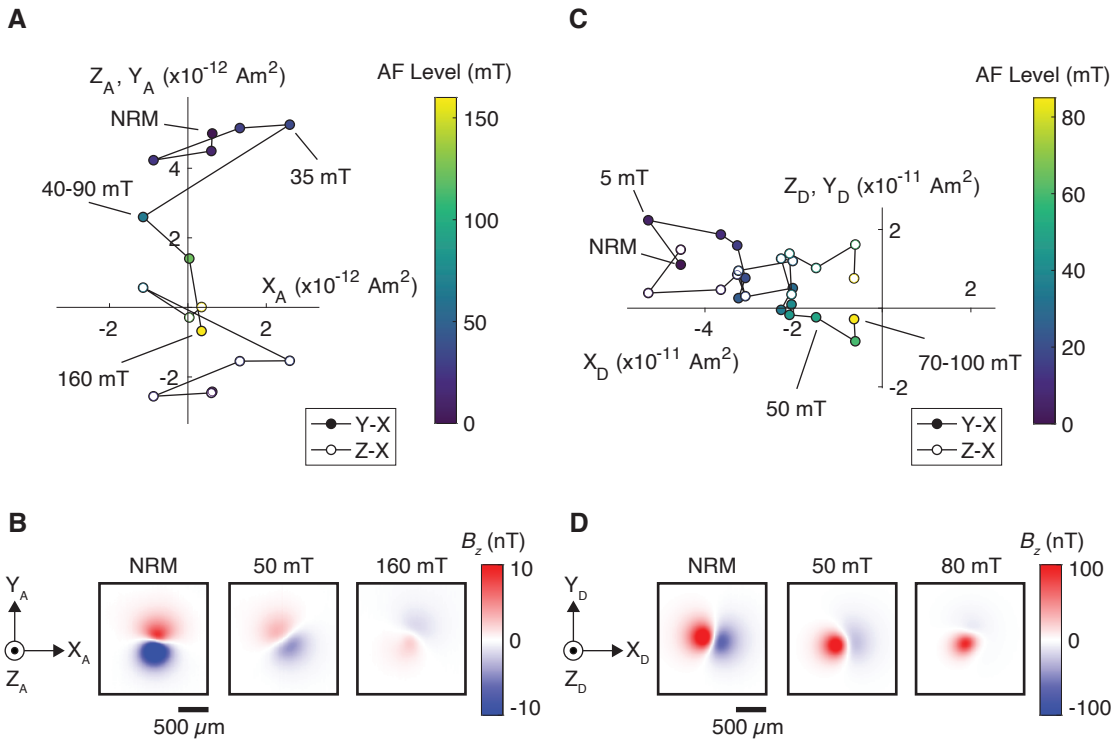

Figure 4-1: **AF demagnetization of CO dusty olivine chondrules.** (**A** and **B**) DOC1 from ALHA77307. (**C** and **D**) DOC4 from DOM 08006. (A and C) Orthographic projections of NRM vector endpoints during alternating field (AF) demagnetization showing averaged measurements for repeated AF steps and across AF levels. Closed symbols show the Y-X projection of the magnetic moment, and open symbols show Z-X projection of the magnetic moment; subscripts "A" and "D" denote separate coordinate systems for ALHA77307 and DOM 08006, respectively. We interpret the steps between NRM and 160 mT for DOC1 and between 50 and 850 mT for DOC4 as constituting the HC components. Selected demagnetization steps are labeled. Color scales show the AF levels. (B and D) Out-of-the-page magnetic field component (B_z) maps for selected steps measured at a height of ∼300 μm above the chondrules obtained with the SQUID microscope. Each map represents one of six maps associated with different applications of the AF field to obtain each step shown in the orthographic projection.

conglomerate tests (see the Supplementary Materials). Because the nebular field is expected to have been directionally homogeneous on submillimeter length scales, a nebular TRM should be unidirectional within each chondrule. Our measurements confirm this: Pairs of subsamples of three DOM 08006 chondrules have HC directions within each other's maximum angles of deviation (Fig. 4-2). In addition, if the chon-

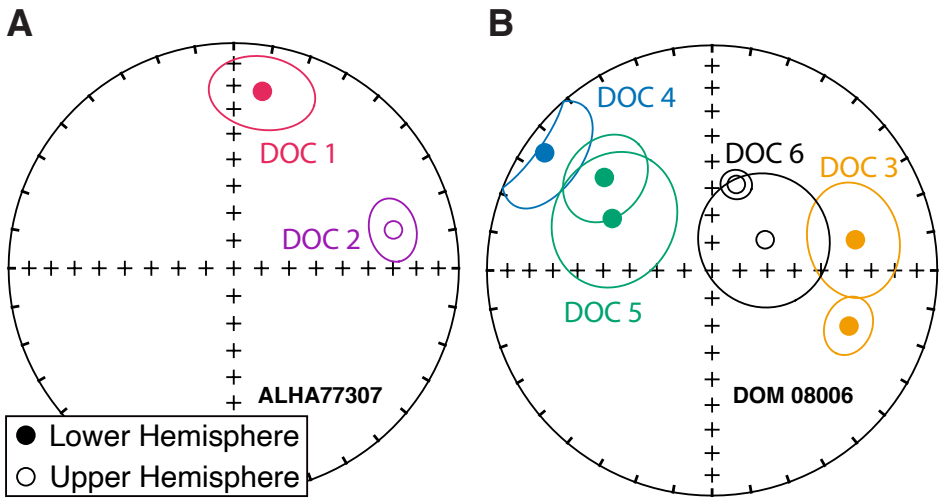

Figure 4-2: **Direction of the HC components of the dusty olivine chondrules from CO chondrites.** (**A**) ALHA77307. (**B**) DOM 08006. Shown are equal area stereographic projections containing directions calculated from principal components analysis and their corresponding maximum angular deviations. Points with different colors are from different individual chondrules, while points with identical colors are subsamples from an individual chondrule. The scattered directions from different chondrules in (A) and (B) indicate that the meteorites were not remagnetized since the chondrules accreted. The clustered directions among subsamples of the same chondrules in (B) are consistent with that expected for a TRM acquired during primary cooling in the solar nebula.

drules have not been remagnetized since parent body accretion (including on their parent body and after arrival on Earth), then they should collectively exhibit random magnetization directions. Our measurements of two chondrules from ALHA77307 and four chondrules from DOM 08006 (Fig. 4-2) confirm this: We cannot reject the hypothesis that both sets of directions are random with 95% confidence (Watson, 1956) (see the Supplementary Materials). In summary, the unidirectionality and conglomerate tests strongly support the conclusion that the chondrules carry robust paleomagnetic records of the solar nebula magnetic field acquired before accretion onto their parent bodies.

To determine the paleointensity of the recorded field, we compared the AF demagnetization of the NRM to that of an anhysteretic remanent magnetization (ARM) acquired in a bias field of 200 μT and a peak AF of up to 145 mT for seven chondrules [following previous studies (Tikoo et al., 2014)]. Paleointensity estimates were

estimated assuming a ratio of ARM to TRM of 1.87 as previously measured for dusty olivine chondrules (see Materials and Methods). The resulting mean HC paleointensity estimates from two ALHA77307 chondrules and five DOM 08006 chondrules are 30 ± 10 μT and 59 ± 31 μT, respectively. Combining the seven samples and accounting for chondrule spinning during TRM acquisition [which decreases the background nebular field intensity recorded by the chondrule by an average factor of 2 (Fu et al., 2014)], we obtained a grand mean paleointensity of the background nebular field of 101 ± 48 μT (table S2).

4.5 Discussion

Together with the previous paleomagnetic study of CM chondrites (Cournede et al., 2015), the magnetic record from CO chondrules strongly supports the presence of a nebular magnetic field in the carbonaceous reservoir at ∼2 to 3 Ma after CAI formation. Furthermore, the data from the CO chondrules provide the first accurate constraints on the intensity of the nebular magnetic field in the carbonaceous reservoir. In particular, the CO chondrule paleointensities are >16 times higher than the lower limit measured from bulk CM chondrites, which highlights the importance of measuring TRMs to obtain robust magnetic records. The identification of magnetic fields in the noncarbonaceous and carbonaceous reservoirs suggests a widespread role for magnetically driven accretion in the early solar system.

The structures and evolution of protoplanetary disks are governed by the mechanisms that drive disk accretion, likely mediated by magnetic fields. The accretion rate scales quadratically with field strength in the disk midplane with a prefactor depending on disk microphysics (especially ionization and field orientation). For a spatially constant accretion rate, the field intensity should decay as $\sim R^{-5/4}$ or $\sim R^{-11/8}$, where R is the radial distance from the Sun, depending on whether accretion is primarily driven by the radial-toroidal ($R\varphi$) or vertical-toroidal ($z\varphi$) components of the Maxwell stress (Fig. 4-3) (Weiss et al., 2021). Because of the Hall effect, the predicted field intensity is a factor of up to ∼10 higher if the background field threading the disk is

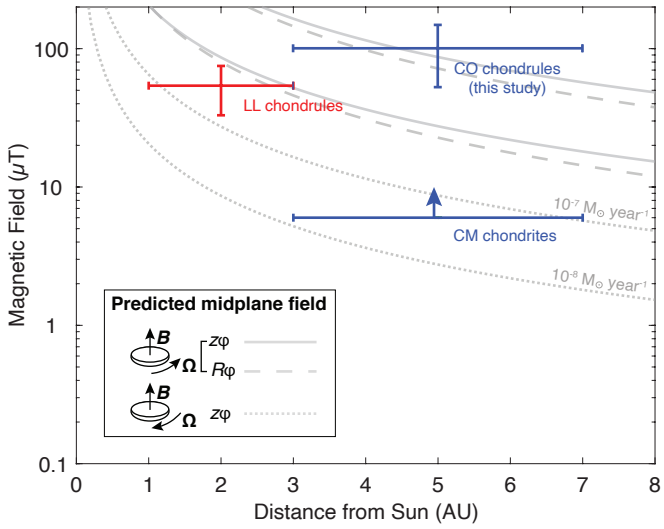

Figure 4-3: **Comparison between paleomagnetic constraints and model predictions for the solar nebula magnetic field intensity.** Shown are paleointensity records from the first 3 Ma after CAI formation: LL chondrules (Fu et al., 2014), CM chondrites (Cournede et al., 2015), and CO chondrules (this study). Solid and dashed lines show predicted midplane magnetic field, due to vertical-toroidal [$z\varphi$; equation 3 of Weiss et al. (2021)] and radial-toroidal [$R\varphi$; equation 2 of Weiss et al. (2021)] Maxwell stresses, respectively, assuming the nebular magnetic field and sense of disk rotation are aligned. Dotted lines show the field due to vertical-toroidal Maxwell stresses [$z\varphi$; equation 3 of Weiss et al. (2021)] assuming the nebular magnetic field and sense of disk rotation are antialigned. Top and bottom curves were calculated assuming accretion rates of 10^{-7} and 10^{-8} $M_\odot$ year^{-1} respectively.

aligned with disk rotation axis compared to the antialigned case. Given typical astronomically observed disk accretion rates of $\sim 1\times10^{-8}$ $M_\odot$ year^{-1} (Hartmann et al., 1998), the measured CO paleointensity strongly favors the scenario of aligned polarity (Fig. 4-3), which would otherwise lead to an unreasonably large accretion rate ($\sim 1\times10^{-5}$ $M_\odot$ year^{-1}).

Considering the mean paleointensities from LL and CO chondrules, we find that the accretion rate was highly variable in the early solar system: for a disk with aligned polarity and a net vertical magnetic field ($z\varphi$ only), the accretion rates are $\sim 4^{+4}_{-2}\times10^{-9}$ $M_\odot$ year^{-1} in the noncarbonaceous reservoir and $\sim 1^{+2}_{-0.6}\times10^{-7}$ $M_\odot$ year^{-1} in the carbonaceous reservoir (Fig. 4-3). The observed factor of $\sim$5 to 150 variation in the magnetically driven accretion rate between the two reservoirs could reflect variations in the accretion rate in time and/or in space. Temporal variations

would be broadly consistent with astronomically observed accretion bursts in protoplanetary disks that occur on a timescale of hundreds of years (Hartmann et al., 2016). However, our Monte Carlo simulations suggest that the probability that the observed changes in accretion are due to temporal fluctuations is <0.4% (see the Supplementary Materials). Thus, our results favor the presence of a spatial mismatch in the magnetically driven accretion rates between the two reservoirs. This spatial mismatch in the accretion rate has also been observed in recent paleomagnetic measurements of the CV chondrite Allende (Fu et al., 2021). While a spatial variation in accretion rate has also been proposed to explain the anomalously weak fields recorded by CR chondrules, it was not possible to conclusively differentiate between varying accretion rates or a null magnetic record because of the prior dissipation of the solar nebula in those samples (Weiss et al., 2021).

The observed mismatch in the accretion rates requires a mechanism that removed mass from the accretion flux between the carbonaceous and the noncarbonaceous reservoirs. If proto-Jupiter or another giant planet was present between the two reservoirs, then it is possible that part of this accretion flux was intercepted and accreted onto the growing planet. However, if the mismatch was completely due to accretion onto proto-Jupiter, that would require a growth time scale of just ∼10,000 years for the planet. This is several orders of magnitude faster than the several–million year time scale predicted by the core accretion model, the favored mechanism for Jupiter formation (Atreya et al., 2018). Alternatively, a large fraction of accretion mass flux could be lost through a disk outflow. A substantial mass loss has been predicted in theoretical models of photoevaporation leading to inside-out disk clearing [e.g., (Clarke et al., 2001; Owen et al., 2012; Picogna et al., 2019)]. On the other hand, given the likely role magnetic fields in driving disk accretion, photo-evaporation and magnetized disk winds may operate concurrently (Wang et al., 2019; Bai, 2016), leading to magnetothermal disk winds whose mass loss rates are comparable to or exceed that of observed accretion rates of protoplanetary disks. This is sufficient to account for our observed mismatch in accretion rates and potentially lead to the formation of an inner cavity (i.e., extreme version of a gap) (Suzuki et al., 2016). Note,

however, that this scenario does not preclude a role for Jupiter in gap formation. Its presence would likely accelerate the formation of the cavity (Rosotti et al., 2013), transforming the solar nebula into a transition disk.

In summary, we present a robust record of magnetic fields in the carbonaceous reservoir of the solar nebula. When compared to previous measurements of magnetic fields from the noncarbonaceous reservoir and models that describe the magnetic field in protoplanetary disks, we observe that the accretion rate in the carbonaceous reservoir is several times higher than that of the noncarbonaceous reservoir, implying the presence of a mismatch in accretion rates. This mismatch may be associated with disk mass loss through the presence of a gas giant, photoevaporation, and/or magnetized winds. These mechanisms could produce a disk substructure like those observed astronomically and like that inferred from the isotopic dichotomy measured among various meteorites in the early solar system.

Chapter 5

Paleomagnetism of CO chondrites

5.1 Chapter Introduction

The evolution and lifetime of protoplanetary disks (PPDs) play a central role in the formation and architecture of planetary systems. Astronomical observations suggest that PPDs go through a two-timescale evolution, accreting onto the star over a few to several million years (Ma) followed by gas-dissipation within $\lesssim$1 Ma. This timeline is consistent with gas dissipation by photoevaporation and/or magnetohydrodynamic winds. Because solar nebula magnetic fields are sustained by the gas of the protoplanetary disk, we can use paleomagnetic measurements to infer the lifetime of the disk. Here we use paleomagnetic measurements of meteorites to investigate whether the disk that formed our solar system had a two-timescale evolution. We report on paleomagnetic measurements of bulk subsamples of two CO carbonaceous chondrites: Allan Hills A77307 and Dominion Range 08006. If magnetite in these meteorites could acquire a crystallization remanent magnetization that recorded the ambient field during aqueous alteration, our measurements suggest that the local magnetic field strength at the CO parent-body location was $<$0.9 μT at some time between 2.7-5.1 Ma after the formation of calcium-aluminum-rich inclusions. Coupled with previous paleomagnetic studies, we conclude that dissipation of the solar nebula in the 3-7 AU region occurred $<$1.5 Ma after the dissipation of the nebula in the 1-3 AU region, suggesting that protoplanetary disks go through a two-timescale evolution in

their lifetime. We also discuss future directions necessary to obtain robust records of solar nebula fields using bulk chondrites, including obtaining ages from relevant chondrites and experimental work to determine how magnetite acquires magnetization during chondrite parent-body alteration.

5.2 Introduction

The lifetimes of protoplanetary disks (PPDs) have important implications for the formation of planetary systems that emerge from them. Determining the lifetime of PPDs (i.e., the dissipation of the gas) constrains the formation time of gas giants and when gas-driven planetary migration can occur. The lifetimes of PPDs have been measured astronomically through observations of dust infrared spectral energy distributions (SEDs) (Haisch et al., 2001; Hernández et al., 2007). SED observations have provided evidence that disks pass through different stages during their evolution from that of protostars to transition disks (disks that have low or no near-infrared excess and high mid- to far-infrared excess) and to debris disks (no remaining gas) (Ercolano and Pascucci, 2017; Owen, 2016). With the exception of a few observed PPDs that are likely in the transition phase, the majority (90%) of observed PPDs are either in PPD phase with a protostar or completely dissipated (Owen, 2016). This observation has been interpreted to suggest that PPDs have a two time-scale evolution during their lifetime: during the first evolutionary stage, which lasts $\sim$ 3-5 million years (Ma), the disk evolves via magnetohydrodynamic and/or hydrodynamic processes, with angular momentum transported outwards that enables accretion onto the star (Armitage and Kley, 2019; Gorti et al., 2016); during the second stage, the remaining gas disperses rapidly, in $\lesssim$ 1 Ma (Ercolano and Pascucci, 2017). Several modes of disk dispersal have been proposed (Ercolano and Pascucci, 2017), including photoevaporation by the central star (Alexander et al., 2006) or a nearby high-mass star (Concha-Ramírez et al., 2019; Scally and Clarke, 2001), magnetohydrodynamic (MHD) winds (Armitage et al., 2013; Bai, 2016; Shadmehri and Ghoreyshi, 2019; Suzuki et al., 2016), planet formation (Zhu et al., 2011), grain growth (Dullemond

and Dominik, 2005)and close-binary effects (Ireland and Kraus, 2008). The two-timescale evolution is generally consistent with gas dissipation by photoevaporation and/or magnetohydrodynamic winds. Because the lifetimes of PPDs are far greater than the times over which we can observe them, testing the two timescale hypothesis through observations of any one PPD is essentially impossible. However, the two-timescale hypothesis can be tested using paleomagnetic measurements of our solar system's PPD, also known as the solar nebula. Due to the coupling of magnetic fields with gas, the nebular magnetic field is a proxy for the presence of gas in the disk, and thus the lifetime of the disk (Wang et al., 2017; Weiss et al., 2021). By obtaining paleomagnetic measurements from meteorites that formed at different times and locations, it is possible to constrain the lifetime and spatial evolution of the PPD of our solar system. Previous paleomagnetic studies of meteorites have provided evidence for a large scale magnetic field present in the disk up to at least $3.9^{+0.4}_{-0.5}$ Ma after the formation of the calcium-aluminum-rich inclusions (CAIs) (Borlina et al., 2021c; Cournede et al., 2015; Fu et al., 2014). Additional studies have also found evidence for the dissipation of the gas at $<$3 AU (inner solar system) by 3.2-5.0 Ma after CAI formation, with Pb-Pb ages indicating a mean dissipation time by 3.71 $\pm$ 0.2 Ma after CAI-formation (Wang et al., 2017; Weiss et al., 2021).

Here we use carbonaceous chondrites to obtain better constraints on the timescale of the dissipation of the solar nebula. Carbonaceous chondrites are unmelted accretional aggregates of refractory inclusions (CAIs and amoeboid olivine aggregates), chondrules and matrix, which likely formed in the 3-7 AU region (i.e., outer solar system). In this study, we investigate the magnetic record of bulk subsamples of carbonaceous chondrites that contain all of these constituents. If not overprinted or remagnetized, chondrules and refractory inclusions are expected to carry pre-accretional magnetic records, while the matrix would recorded a post-accretional magnetic record obtained during parent-body alteration. Paleomagnetic measurements conducted with bulk samples are likely to provide magnetic records from the matrix material, because if chondrules and refractory inclusions are randomly oriented in the bulk and, even if magnetized, the magnetic moments of the inclusions

cancel out and the matrix would dominate the magnetic record (see appendix).

We report on paleomagnetic measurements of bulk matrix-rich material of two carbonaceous chondrites from the CO group. A previous study of the CV chondrite Kaba provided an upper limit on the magnetic field at 3-7 AU of $<$0.3 µT at $4.2^{+0.8}_{-0.7}$ Ma after CAI formation (Doyle et al., 2014; Gattacceca et al., 2016). We further investigate this region by targeting another group of carbonaceous chondrites that likely acquired a post-accretional magnetic record in this region but that, unlike Kaba, are much less likely to carry thermally induced parent-body magnetic overprints. Assuming that magnetite could have acquired its magnetic record during alteration in the parent-body, we show that the matrices of the CO chondrites carry no stable natural remanent magnetization (NRM) despite having high fidelity magnetic recording properties and ferromagnetic minerals that formed after accretion. We show that the lack of magnetization in the matrix of the CO chondrites, together with previous paleomagnetic measurements, suggests that the dissipation of the outer solar system nebula occurred by $\sim$4.2 Ma after CAI formation. By comparing the inner and outer solar system lifetimes of the nebula, we find that the outer solar nebula dissipated $<$1.5 Ma after the dissipation of the inner solar nebula, suggesting that our solar nebula passed through a dual-timescale evolution. We also discuss future work necessary to obtain robust records of the solar nebula by conducting paleomagnetic and rock magnetic measurements of bulk chondrites. This includes obtaining more high-precision ages from relevant meteorites and conducting experimental work to establish the mechanisms for acquisition of magnetic field records during parent-body alteration, including in particular if secondary magnetite can record CRMs imparted by the solar nebula field.

5.3 Methodology

5.3.1 Samples

In this study, we focused on the type 3.03 CO chondrite Allan Hills (ALH) A77307 (Bonal et al., 2007) and on the type 3.00 CO chondrite Dominion Range (DOM) 08006 (Davidson et al., 2019). We selected these samples for several reasons. First, they formed magnetite during aqueous alteration on their parent body, so can potentially provide constraints on the intensity of the local ambient magnetic field present during this process (Doyle et al., 2014). Second, they have ferromagnetic inclusions (e.g., magnetite; see below) with high-fidelity paleomagnetic properties formed during parent-body alteration (Alexander et al., 2018; Davidson et al., 2019). Third, they experienced very minor heating after parent-body aqueous alteration, thereby better preserving a magnetic record dating to the time of this early alteration rather than slightly later during subsequent metamorphic heating and cooling (Davidson et al., 2019).

CO Carbonaceous Chondrites

Subsamples ALHA77307,157 (0.57 g) and DOM 08006,102 (2.8 g) were obtained from the US Antarctic Meteorite program (ANSMET). These were chipped from the meteorite at NASA Johnson Space Center (JSC) and did not contain any faces from band sawing at JSC that could have resulted in thermal remagnetization during cutting [e.g., Mighani et al. (2020); Tikoo et al. (2017)]. Each contained fusion crust on one of their faces.

Both meteorites experienced aqueous alteration and metamorphism on their parent body as indicated by the presence of only a small fraction of metal (2 vol.%) in the matrix and on the edges of chondrules, with most of the metal having been altered to magnetite (Bonal et al., 2016; Davidson et al., 2019). ALHA77307 experienced minor terrestrial weathering (Ae grade) and is estimated to have experienced a peak parent body metamorphic temperature between 200-300 ^{o}C (Bonal et al., 2016) resulting from aqueous alteration and metamorphism on the parent-body. DOM 08006

has experienced minor terrestrial weathering (A/B grade) (Davidson et al., 2019) and has experienced similar or slightly lower peak temperatures in the parent body than ALHA77307 (Alexander et al., 2018). ALHA77307 and DOM 08006 did not exceed peak shock pressures of 5 GPa (Scott et al., 1992; Li et al., 2021). Overall, these observations suggest that ALHA77307 and DOM 08006 potentially carry records of magnetic fields from the early solar system acquired during parent-body aqueous alteration.

The paleomagnetism of the CO chondrites has been briefly studied before [see (Weiss et al., 2010) for complete list of magnetic measurements with CO chondrites]. A previous study conducted thermal demagnetization of saturation magnetization of four CO3 chondrites (Herndon et al., 1976), which found that one contains magnetite as the major magnetic phase, while the remaining samples contained magnetite along with iron metal as the main magnetic phases. Two previous exploratory paleomagnetic studies obtained paleointensities from CO chondrites. Measurements of bulk subsamples of the CO3 chondrite Acfer 333 identified a low coercivity component (0-15 mT) associated with an isothermal remanent magnetization (IRM) (likely from a collectors' hand magnet) and a high coercivity component (30-120 mT) with a paleointensity of 6 µT (Gattacceca and Rochette, 2004). Another study of bulk subsamples of the CO3.05 Yamato 81020 meteorite reported a high blocking temperature (320-640 ^{o}C) component with a paleointensity of 9 μT (Nagata et al., 1991). A paleomagnetic study of dusty olivine chondrules from ALHA77307 and DOM 08006 suggest that these meteorites have not been remagnetized since accretion to the parent-body due to their random high coercivity magnetic directions among mutually-oriented chondrules (Borlina et al., 2021c). Here we focus on using ALHA77307 and DOM 08006 to conduct a detailed paleomagnetic study of bulk samples.

Previous mineralogical and petrological studies of the matrix of DOM 08006 have reported the presence of the ferromagnetic minerals kamacite (Fe_xNi_{1-x}; with x = 92-93), magnetite and pyrrhotite ($Fe_{1-x}S$; with $x \sim 0$) (Alexander et al., 2018; Davidson et al., 2019; Schrader et al., 2021). Similar minerals have been reported for ALHA77307 (Alexander et al., 2018; Davidson et al., 2019; Grossman and Brearley,

2005; Schrader et al., 2021). The amount of magnetite (6-8 wt.%) is higher than sulfide (2-3 wt.%) and metals (1-2 wt.%) in the matrix of DOM 08006 (Alexander et al., 2018). Below we discuss why magnetite is likely to dominate the magnetic record of these samples. Recent FORC analysis of DOM 08006 shows a tri-lobate geometry which is consistent with the magnetic carriers being predominately in vortex states (Sridhar et al., 2021). Because magnetite is the most abundant magnetic recorder and with the highest susceptibility (see below), we conclude that the magnetite grains are dominantly in the vortex state, such that they are robust magnetic recorders with relaxation times greater than the age of the solar system (Nagy et al., 2019b)

Because magnetite formed during parent body alteration (Davidson et al., 2019) and was not subsequently heated above 300 ^{o}C, the magnetic record of these samples should be predominately in the form of crystallization remanent magnetization (CRM). No radiogenic ages have been reported for ALHA77307 and DOM 08006. Previous work determined a ^{5}3Mn-^{5}3Cr age from aqueously formed fayalite of $5.1^{+0.5}_{-0.4}$ (2σ) Ma after CAI-formation from the meteorite MacAlpine Hills (MAC) 88107, a chondrite that formed from precursor material that had isotopic similarities to that of the CO parent-body but has not previously been officially categorized as a CO chondrite (Doyle et al., 2014; Torrano et al., 2021). As such, this measured age is likely a proxy for the youngest possible age of magnetite formation on the CO chondrite parent body. Furthermore, Al-Mg ages of chondrules from CO chondrites suggest that they formed at 2.1 $\pm$ 0.8 Ma after CAI formation (Borlina et al., 2021c; Kita and Ushikubo, 2011) and recent modelling to explain the inventory of CAIs among different chondrite groups suggests that the CO chondrite parent-body accreted at 2.7 Ma after CAI formation (Desch et al., 2018). Thus, we can place a lower limit on the alteration age of the CO chondrites of 2.7 Ma after CAI formation, while an upper limit can be obtained by using MAC 88107's alteration age of 5.1 Ma after CAI formation.

Formation Region of the CO Carbonaceous Chondrites

The existence of a dichotomy in various stable isotopic systems (Kruijer et al., 2020; Scott et al., 2018) provides evidence that carbonaceous and non-carbonaceous meteorites formed in two distinct reservoirs. Although the exact locations for these reservoirs are unclear, it is generally thought that carbonaceous chondrites likely formed at >3 AU (Brasser and Mojzsis, 2020; DeMeo and Carry, 2014; Desch et al., 2018; Kruijer et al., 2020; Morbidelli et al., 2015). Measurements of water contents from CI, CM, CR and LL chondrites provide evidence that carbonaceous chondrites formed at <7 AU (Sutton et al., 2017). Thus, we assume the formation region of the carbonaceous chondrites to be between 3-7 AU. We also assume that chondrite parent bodies originate from the midplane region of the PPD because drag forces on 0.1-mm-sized grains lead them to settle on the midplane of the PPD, resulting in the formation of the parent-bodies in that region (Weiss et al., 2021).

Magnetite as the Main Magnetic Carrier of Bulk Samples

Because bulk samples contain magnetic minerals that are pre-accretional (e.g., kamacite) and post-accretional (e.g., magnetite) in origin, it is important to establish which one of them will dominate the magnetization record. The NRM moment M, measured in the laboratory, is proportional to the magnetic field, B experienced by the sample, through:

$$M = \chi B, \tag{5.1}$$

where χ is the magnetic susceptibility of the sample (Tauxe, 2010):

$$\chi \sim \mu_0 f M_{rs}, \tag{5.2}$$

where μ_0 is the magnetic constant $4\pi\times10^{-7}\mathrm{TmA}^{-1}$, f is a constant proportional to the volume V of the sample (Wieczorek et al., 2012) and M_{rs} is the saturation remanent magnetization which is proportional to the squareness ratio s and the saturation magnetization Ms (Wieczorek et al., 2012). Thus, for a sample that contains magnetite and kamacite, we can determine χ based on the sum of the susceptibilities

of each mineral through:

$$\chi = \chi_{mag} + \chi_{kam}, \tag{5.3}$$

$$\chi_{mag} = \mu_0 V_{mag} s_{mag} M_{s,mag}, \tag{5.4}$$

$$\chi_{kam} = \mu_0 V_{kam} s_{kam} M_{s,kam}, \tag{5.5}$$

where χ_{mag} is the susceptibility of the magnetite and χ_{kam} the susceptibility of kamacite. Taking the ratio between Eqs. 5.4 and 5.5, we have:

$$\frac{\chi_{mag}}{\chi_{kam}} = \frac{V_{mag}}{V_{kam}} \frac{s_{mag}}{s_{kam}} \frac{M_{s,mag}}{M_{s,kam}}. \tag{5.6}$$

From DOM08006, V_{mag}/V_{kam} ∼3-8 (Davidson et al., 2019). Additionally, because most magnetite is likely to be in single-vortex and single-domain state, while kamacite is likely to be multi-domain, we can assume $s_{mag}s_{kam} > 100$ (Dunlop, 2002). Finally, $M_{s,mag} = 480$ kA/m and $M_{s,kam} = 1715$ kA/m (Dunlop and Özdemir, 1997). Thus, $\chi_{mag} > 84\chi_{kam}$, indicating that magnetite will be the main magnetic carrier of the NRM in these samples.

5.3.2 Paleomagnetic and Rock Magnetic Experiments

Sample preparation and paleomagnetic analyses were conducted in the Massachusetts Institute of Technology (MIT) Paleomagnetism Laboratory. Samples from each meteorite were obtained by cutting with a wire-saw cooled with ethanol to avoid acquisition of partial TRM (pTRM) during cutting. We obtained eight mutually oriented samples from ALHA77307 and eleven mutually oriented samples from DOM 08006. Tables 5.1 and 5.2 summarizes the mass and distance from the fusion crust to the outer edge of each sample. Paleomagnetic measurements were obtained in a magnetically shielded room (residual field ∼200 nT) using a 2G Enterprises Superconducting Rock Magnetometer (SRM) 755R equipped with an automatic alternating field (AF) three-

axis degausser and remagnetization system (Kirschvink et al., 2008). The three-axis moment noise level of the MIT 2G SRM is $<1\times10^{-12}$ Am2 (Wang et al., 2017).

We AF demagnetized four samples from ALHA77307 (one containing fusion crust and the remaining from >1.8 mm into the interior) and eight samples from DOM 08006 (one containing fusion crust and the remaining from >1 mm into the interior). These samples were glued with cyanoacrylate cement onto non-magnetic quartz holder with magnetic moments of $<4\times10^{-}12$ Am^2. Samples were demagnetized with AF up to 145 mT to identify NRM components. We measured the magnetic moment after the AF application in each one of three directions and averaged the measurements to reduce spurious anhysteretic remanent magnetization (ARM) and gyroremanent magnetization (GRM) (Stephenson, 1993). We also applied ARMs (AC field of 260 mT and DC bias field of 50 µT) to these samples and AF demagnetized them up to 145 mT. Paleointensities were estimated for these samples using the ARM method (Tikoo et al., 2014).

We thermally demagnetized four samples of ALHA77307 (two containing fusion crust and two interior samples) to identify NRM components and obtain additional paleointensity estimates. We followed the in-field zero-field zero-field in-field (IZZI) double heating protocol to obtain paleointensities (Yu et al., 2004). Heating measurements were performed using an ASC Scientific TD48-SC thermal demagnetizer in air with thermal accuracy better than ±5 ^{o}C. Samples were heated to the set temperature for 20 minutes and cooled within 40 minutes to room temperature. For ALHA77307 and DOM 08006, we initiated the IZZI protocol at 325 ^{o}C and 50 ^{o}C with steps below this being only thermally demagnetized (i.e., only heating in zero-field). The IZZI protocol was conducted in steps of 50 ^{o}C, with a 50 μT bias field and partial TRM (pTRM) checks in 100 ^{o}C steps to estimate whether thermochemical alteration could have occurred during the measurements. Samples were taped to non-magnetic quartz holders for measuring their magnetic moment. Initially, three interior samples of DOM 08006 were thermally demagnetized. However, two of these broke into two mutually oriented subsamples each at 350 ^{o}C, leading to five thermally demagnetized samples. We conducted the IZZI protocol with two of these five

samples. For three samples of ALHA (two fusion crusted and one interior) that we conducted IZZI experiments with, we removed low coercivity components (up to 21 mT) with AF demagnetization prior to the start of the IZZI protocol. We AF demagnetized to the same levels after each in-field step during the protocol. We also thermally demagnetized an ARM application (AC field of 145 mT and DC bias field of 50 μT) of two samples, following AF demagnetization of the NRM, to identify the Curie temperature of the ferromagnetic carriers.

Fits for both the ARM and IZZI paleointensities were obtained either using ordinary least square (OLS) or reduced major axis (RMA) (Borlina et al., 2021c; Smith, 2009). The quality of the results from the IZZI protocol were quantified using the PICRIT03 criteria (Paterson et al., 2014), which quantify thermochemical alteration during the protocol. The ARM method has the advantage over the IZZI protocol of not involving laboratory heating that otherwise can lead to thermochemical alteration. Principal component analysis (PCA) was used to determine the direction and maximum angular deviation (MAD) of the magnetization components identified during the AF and thermal demagnetization (Kirschvink, 1980). To identify any origin trending components, we calculated the deviation angle (DANG). For samples that DANG $<$ unanchored MAD, we calculated the PCA with an anchored fit (Tauxe and Staudigel, 2004).

Nonetheless, because the non-fusion-crusted samples contain CRMs, both the ARM and the IZZI methods cannot reliably reproduce in the laboratory the natural process by which the NRM was acquired by these samples. Therefore, knowledge of the ratio of CRM to ARM and CRM to thermoremance (TRM) is required to obtain paleointensity estimates from these experiments. Unfortunately, these have been poorly constrained by previous studies. Previous studies determined an TRM to ARM ratio f' of 3.33 for magnetite and Fe-Ni bearing samples, which has an estimated 2σ uncertainty that could be of at least a factor of 5 (Weiss and Tikoo, 2014). For alteration timescales of a year to millions of years, such as those experienced by carbonaceous chondrites (Dyl et al., 2012; Ganino and Libourel, 2020; Krot et al., 2006), TRM/CRM can be $\sim$1-2 (McClelland, 1996). For shorter alteration timescales

($\sim 10^3$ s), this ratio can be as large as ∼5-10 (McClelland, 1996). For this study, we assume that TRM∼CRM and we use $f' = 3.33$ for the ARM method. We note that the paleointensities and recording limits described here are likely to be an underestimations and future experiments are necessary to fully determine the CRM to ARM ratio.

We sought to estimate the minimum paleointensity that we could recover from our samples using the ARM method (Bryson et al., 2017; Tikoo et al., 2012). We determined this for each sample by applying a sequence of ARMs (AC field of 145 mT) with DC bias fields ranging from 1 to 10 μT. We then attempted to retrieve these paleointensities using the ARM method described above (using an ARM bias field of 50 μT) in the same coercivity range used to determine the paleointensity. We quantified the accuracy and precision of the retrieved paleointensity estimates with deviation of the retrieved magnetic field from the applied field (D') and the uncertainty of the retrieved field (E) metrics (Bryson et al., 2017; Tikoo et al., 2012). Again, we assumed $f' = 3.33$ such that the range of applied CRM-equivalent paleointensities were 0.3 to 3 μT. For a given sample, we estimate the minimum paleointensity that can be recovered as the lowest value for which a sample having $-0.5 < D' < 1$ and $E < 1$. We also experimentally determined the viscous remanent magnetization (VRM) acquisition and decay rate of one of our samples from DOM 08006 to determine what fraction of the NRM could have been acquired through VRM. We exposed a previously demagnetized sample for 37 days in a terrestrial field of 46 μT and measurements were taken periodically during this time. VRM decay was measured while the sample was kept inside of a magnetically shielded room (∼200 nT) for 14 days and measured periodically. Linear fits were used to calculate the VRM acquisition and decay rates.

5.4 Results

5.4.1 ALHA77307

All AF-demagnetized samples from both the interior and with fusion crust contained a low coercivity (LC) component (blocked up to 58 mT) that had directions with overlapping MADs (Fig. 5-1; Table 5.1). The fusion-crusted samples also contained a high coercivity (HCf) component blocked between 26-410 mT (Fig. 5-1). By comparison, further AF demagnetization of the interior samples to 145 mT demonstrated that they contained no stable magnetization after removal of the LC component (Fig. Figs. 5-1 and 5-3). Using the ARM method, the fusion-crusted samples yielded an apparent paleointensity of 358.5 ± 15.8 μT (these and all other reported uncertainties are 2σ) for the LC component and a paleointensity of 26.7 ± 0.8 muT for the HCf component (Fig. 5-4). The presence of a common LC component among all four samples and the high apparent paleointensity retrieved from the LC component suggest that ALHA77307 was exposed to contamination from a magnet (i.e., IRM) after atmospheric entry. We note that the fact that the fusion crusted samples were not completely remagnetized (i.e., they have both LC IRM overprint and the HCf component) and that the paleointensity of the HCf component has a strength similar to Earth's magnetic field implies that the HCf component is likely a TRM acquired during atmospheric entry. The presence of a HCf component in the fusion-crusted samples and not in interior samples demonstrates that ALHA77307 was not completely remagnetized by the IRM.

The ARM method applied to the apparently non-magnetized high coercivity (HC) range of the interior samples (Fig. 5-4) yielded a paleointensity of 2.2 ± 0.9 μT (Table 5.3). Although the 2σ uncertainty does not formally encompass zero paleointensity, the low paleointensity value and the lack of a unidirectional and stable component in the HC range (Fig. 5-4) suggest that a weak or null field was present when ALHA77307 acquired its magnetic record. Fig. 5-2 and Table 5.3 show that the interior sample (ALHA.d) can record fields >0.9 μT.

Thermal demagnetization of a 50 μT ARM applied to two of the interior sam-

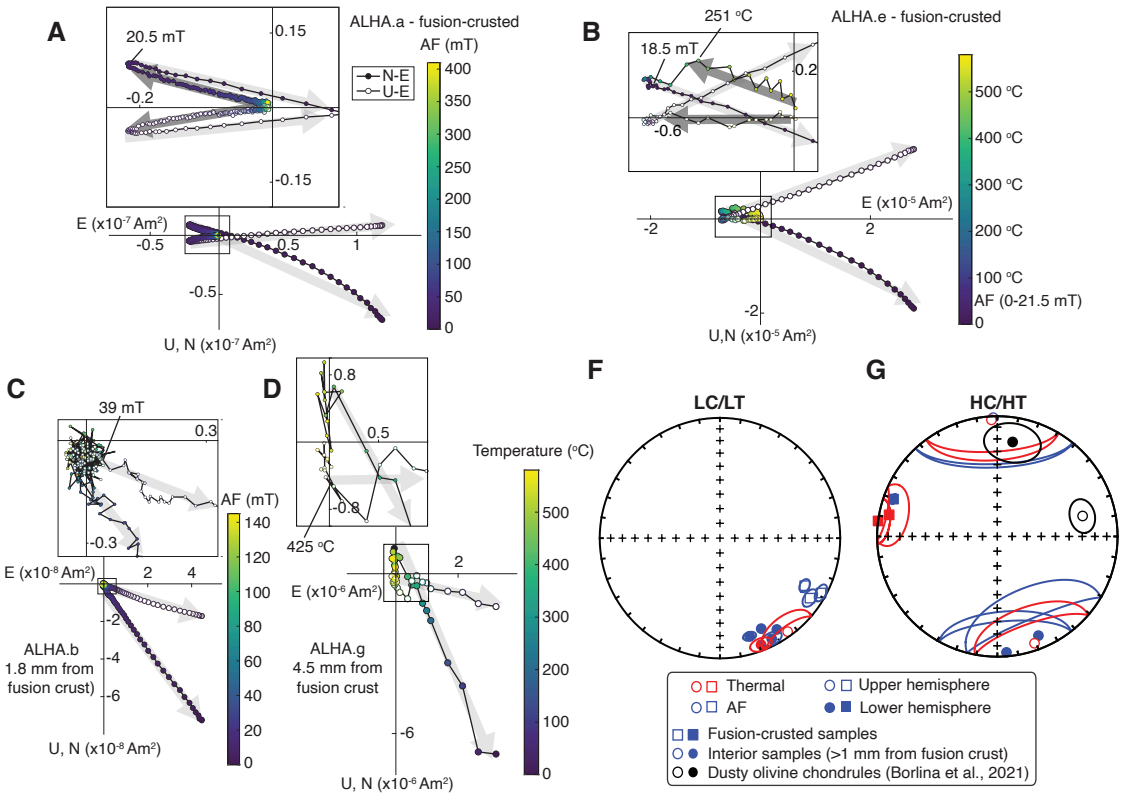

Figure 5-1: **AF and thermal demagnetization of samples from ALHA77307.** Selected orthographic projections of NRM vector endpoints during AF and thermal demagnetization for samples (A) ALHA.a, (B) ALHA.e, (C) ALHA.b and (D) ALHA.g. Closed symbols show the north-east (N-E) projection of the magnetization and open symbols show the up-east (U-E) projection of the magnetization. Selected AF and thermal steps are labeled. (A) and (C) show AF demagnetization from fusion-crusted and interior samples (>1 mm away from fusion crust), respectively. (B) and (C) show thermal demagnetization from fusion-crusted and interior samples, respectively. (F-G) show equal area stereonets with the directions of low coercivity/low temperature (LC/LT) and high coercivity/high temperature (HC/HT) components from all samples measured from ALHA77307. Open and closed symbols represent upper and lower hemispheres, respectively. Red symbols show components from thermal demagnetization, while blue symbols show components from AF demagnetization. Squares show fusion-crusted samples, while circles show interior samples. Black datapoints in equal area stereonet show data from HC components from dusty olivine chondrules from Borlina et al. (2021c).

ples that were previously AF demagnetized, show that the magnetic remanence is carried by sulfide, magnetite (the main magnetic carrier; see above), and Fe-metal, likely awaruite (Fig. 5-5), consistent with the expected mineralogy of CO chondrites. The results of the IZZI protocol are presented in Table 5.4 and Fig. 5-6. After the

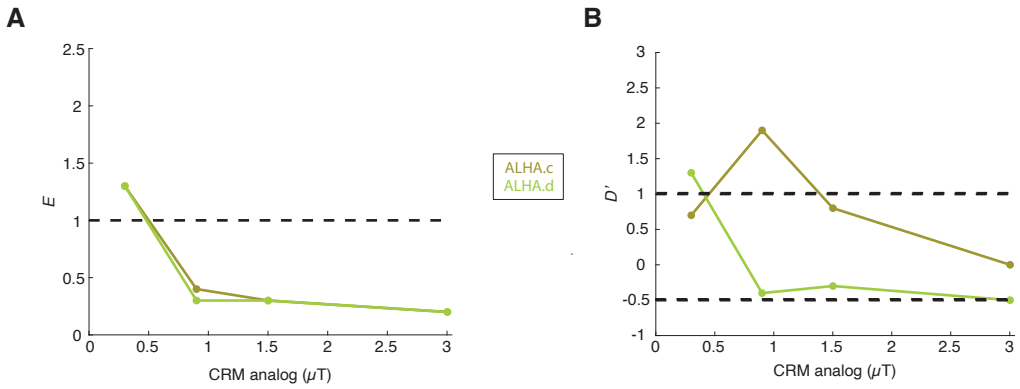

Figure 5-2: E **and** D' **values calculated for samples from ALHA77307.** Values below (A) and between (B) the dashed lines represent reliable paleomagnetic fidelities. The coercivity range, of each sample, used to calculate the paleointensities were used to calculate the E and D' values. The CRM analogs were calculated using $f' = 3.33$ from ARMs (AC field of 145 mT) with DC bias fields of 10, 5, 3 and 1 μT (estimated CRM-equivalent fields of 3, 1.5, 0.9 and 0.3 μT).

removal of the LC component from the fusion crusted samples, we observed high temperature (HTf) components (250-580 ^{o}C) oriented close to the directions of the HCf components (Fig. 5-1). The fusion-crusted samples successfully passed the PICRIT03 criteria, indicating minimum thermochemical alteration during laboratory heating. The paleointensities retrieved from the HTf components were of 13.9 $\pm$ 4.7 μT and 13.9 $\pm$ 5.4 μT (Table 5.4; Fig. 5-6). These are within error of the ARM paleointensities retrieved from the HCf component given the uncertainties in the values of ARM/CRM and TRM/CRM. One interior sample (ALHA.g) had a LT component (0-425 ^{o}C) similar in direction to the LC components of the other samples followed by an origin-trending HT component (425-580 ^{o}C) oriented close to the direction of the laboratory field. The latter may have resulted from thermochemical alteration during the heating experiments (Fig. 5-1D). The other interior sample (ALHA.h; LC removed with AF prior to the IZZI protocol) also had a LT component (51-475 ^{o}C) oriented in the direction of the LC components of the other samples (Fig. 5-3D). Due to thermochemical alteration during heating experiments, both interior samples fail multiple PICRIT03 alteration selection criteria [Table 5.4; Paterson et al. (2014)], which implies that the HT component paleointensities of the interior samples cannot

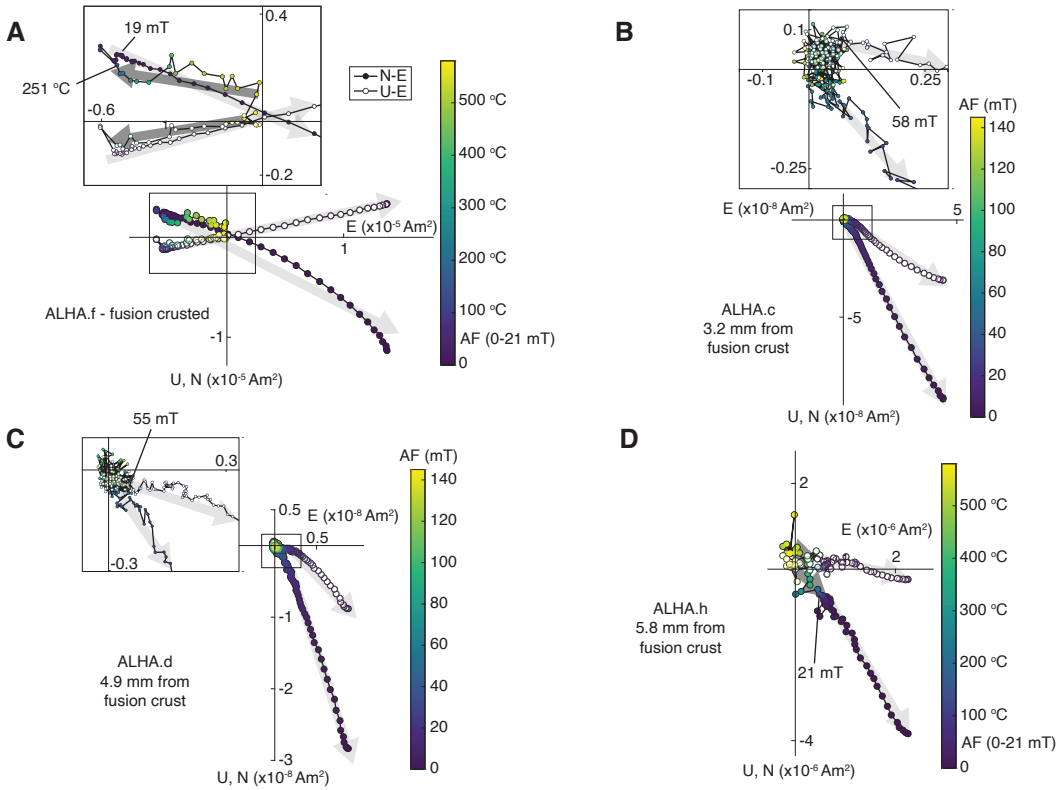

Figure 5-3: **AF and thermal demagnetization of remaining samples from ALHA77307 showing orthographic projections of NRM vector endpoints during AF and thermal demagnetization for samples (A) ALHA.f, (B) ALHA.c, (C) ALHA.d and (D) ALHA.h.** Closed symbols show the north-east (N-E) projection of the magnetization and open symbols show the up-east (U-E) projection of the magnetization. Selected AF and thermal steps are labeled. (A) and (D) show thermal demagnetization from fusion-crusted and interior samples (>1 mm away from fusion crust), respectively. (B-C) show AF demagnetization from interior samples.

be reliably estimated. In summary, the LC/LT component common to all samples is likely an IRM that did not completely overprint the sample, almost certainly acquired during sample handling. The HCf/HTf component, which is only present in the fusion-crusted samples, is consistent with magnetization acquired during heating from atmospheric entry in Earth's magnetic field. The lack of a unidirectional HC magnetization among most interior samples together with fidelity tests indicate that the ancient field environment was less <0.9 μT when ALHA77307 acquired its magnetization.

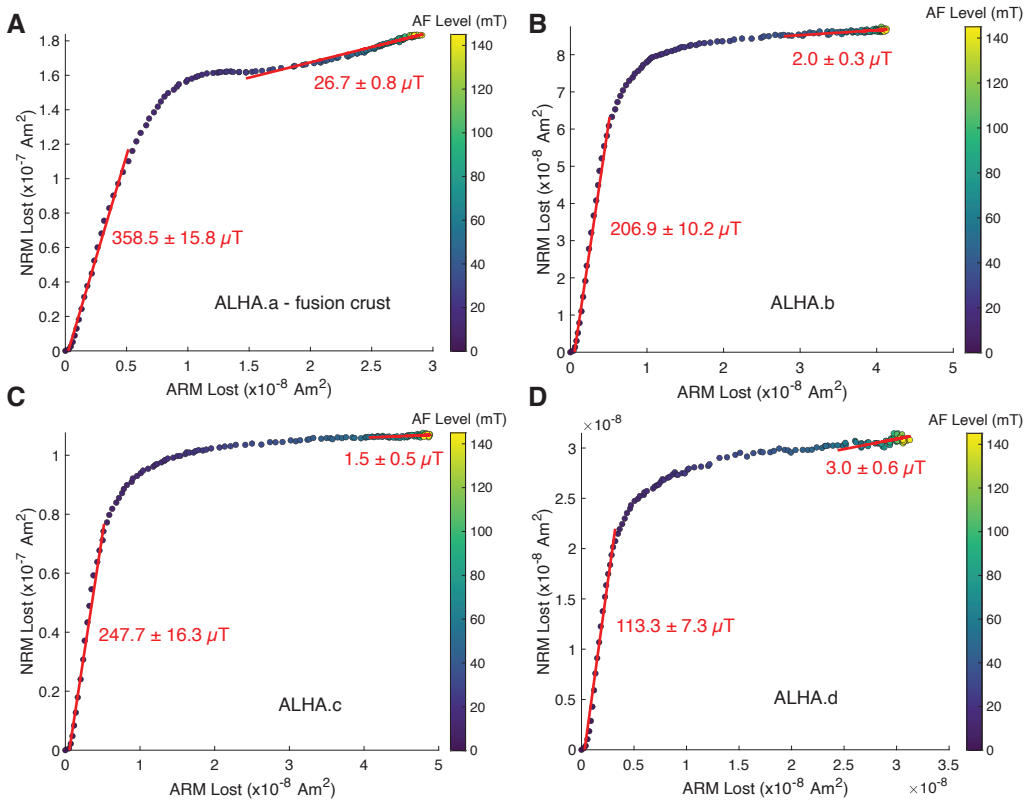

Figure 5-4: **ARM paleointensity experiment for samples (A) ALHA.a, (B) ALHA.b, (C) ALHA.c and (D) ALHA.d from ALHA77307.** Shown is NRM lost during stepwise AF demagnetization up to 145 mT and ARM lost during AF demagnetization up to 145 mT of an ARM (AC field of 145 mT with a DC bias field of 50 μT). Paleointensitites ($f' = 3.33$) and their 95% confidence intervals are reported along with the red line that represents the range of coercivities used to calculate the fit.

5.4.2 DOM 08006

All AF-demagnetized DOM 08006 samples from the interior had a common LC component blocked between 6-28 mT (Figs. 5-7 and 5-8; Table 5.2). The fusion-crusted sample had a single origin-trending HCf component blocked up to 145 mT (Fig. 5-7). Using the ARM method, we obtained a paleointensity of 39.5 ± 0.4 μT for the HTf component of the fusion-crusted sample, consistent with Earth's magnetic field strength as recorded during atmospheric entry (Table 5.3; Fig. 5-9).

Four interior samples had medium coercivity (MC) components with coercivities up to 45 mT (Fig. 5-7), but no stable HC magnetization blocked beyond this. A

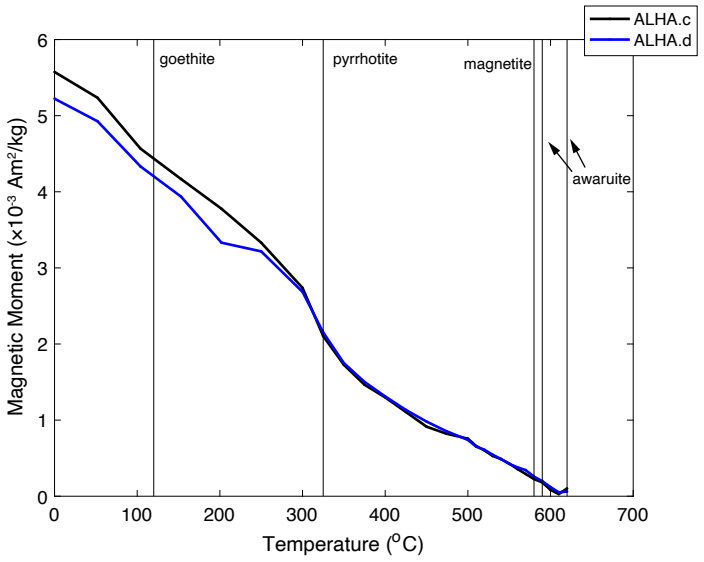

Figure 5-5: **Thermal demagnetization of ARM (AC field of 145 mT with a DC bias field of 50 μT) for samples ALHA.c (black) and ALHA.d (blue).** Shown is magnetic moment as a function of temperature. Vertical lines indicates the Curie temperature of magnetic minerals.

fifth sample had a HC component between 19-145 mT (Fig. 5-8A). The remaining two samples did not carry any components blocked above 15 mT. PCA of the HC range yields scattered directions and MAD values $>40^o$ for most samples (Fig. 5-7; Table 5.2). The LC and MC components are likely associated with viscous remanent magnetization (VRM) and/or low temperature parent body thermochemical alteration. To assess this, we analyzed the VRM acquisition and decay properties of sample DOM.m following the AF demagnetization experiments. We measured a VRM acquisition rate of of 1.15×10^{-6} Am^2 kg^{-1} μT^{-1} and a VRM decay rate that was shallow at first ($\sim10^3$ seconds) with a decay rate of 2.06×10^{-8} Am^2 kg^{-1} μT^{-1}, followed by an increase in the decay rate to a value of 8.17×10^{-7} Am^2 kg^{-1} μT^{-1} (Fig. 5-10). Because Antarctic meteorites typically have terrestrial ages of a few tens of thousands of years (Jull, 2006) with some surviving for up to 2 million years, we estimate that $\sim$52% of the NRM of the DOM.m could have been acquired in 10,000 years on the Earth's surface, consistent with the magnetic moment carried by the LC component.

The ARM method yielded a mean paleointensity of 1.2 ± 1.4 μT for the HC range

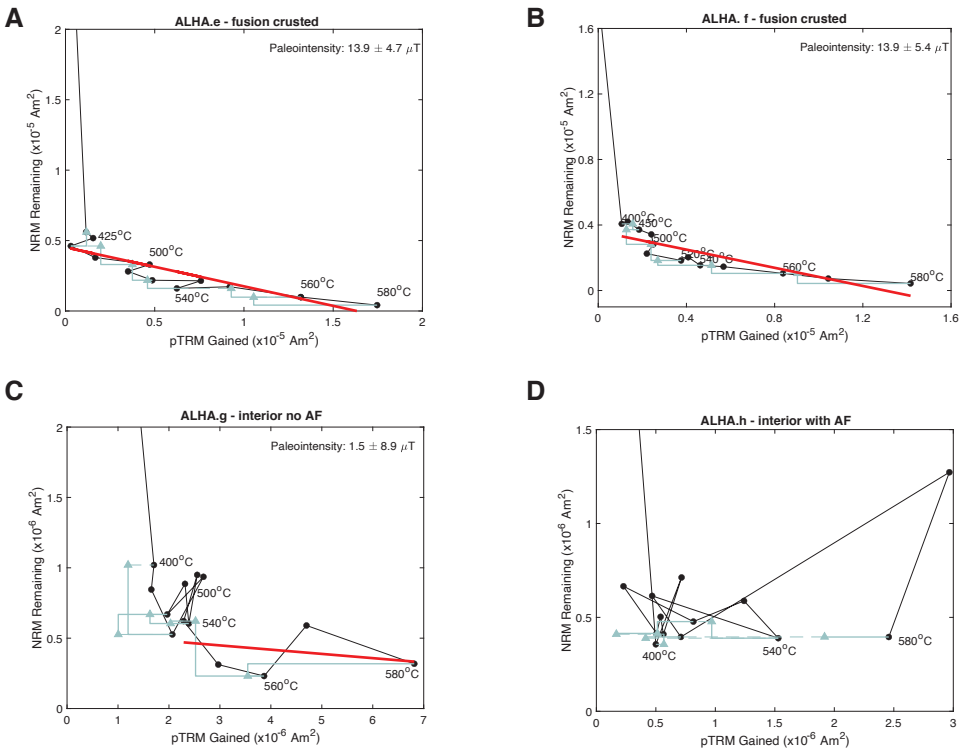

Figure 5-6: **NRM remaining versus partial TRM (pTRM) gained during progressive laboratory heating for samples (A) ALHA.e, (B) ALHA.f, (C) ALHA.g and (D) ALHA.h from ALHA77307.** Blue triangles show pTRM checks. The red lines show the measurements used to compute paleointensity values. (A-B) show fusion-crusted samples that had their LC overprint demagnetized with AF to 21 mT. (C) shows interior sample that did not have the LC overprint removed. (D) shows interior sample that had the LC overprint removed by AF to 21 mT. (A), (B) and (D) were demagnetized to 21 mT pre-in-field steps during the IZZI experiments.

(Figs. 3 and S6; Table 2). Like the interior samples from ALHA77307, the lack of stable, unidirectional components in the HC range, the paleointensities within error of zero retrieved from the ARM method, and the demonstrated capacity for gaining ARM in the same non-magnetized range (Figs. 5-9 and 5-12) indicate that a weak to null field was present when the magnetic record was acquired. We chose to not include DOM.c and DOM.l as part of our paleointensity analysis. DOM.c contains a well constrained HC component (19-145 mT, MAD = 13.9^o) that is not observed in any other sample and records a paleointensity of 4.1 ± 0.2 μT. DOM.l also contained a HC component (28-145 mT, MAD = 21^o) with a distinct direction than that of DOM.c,

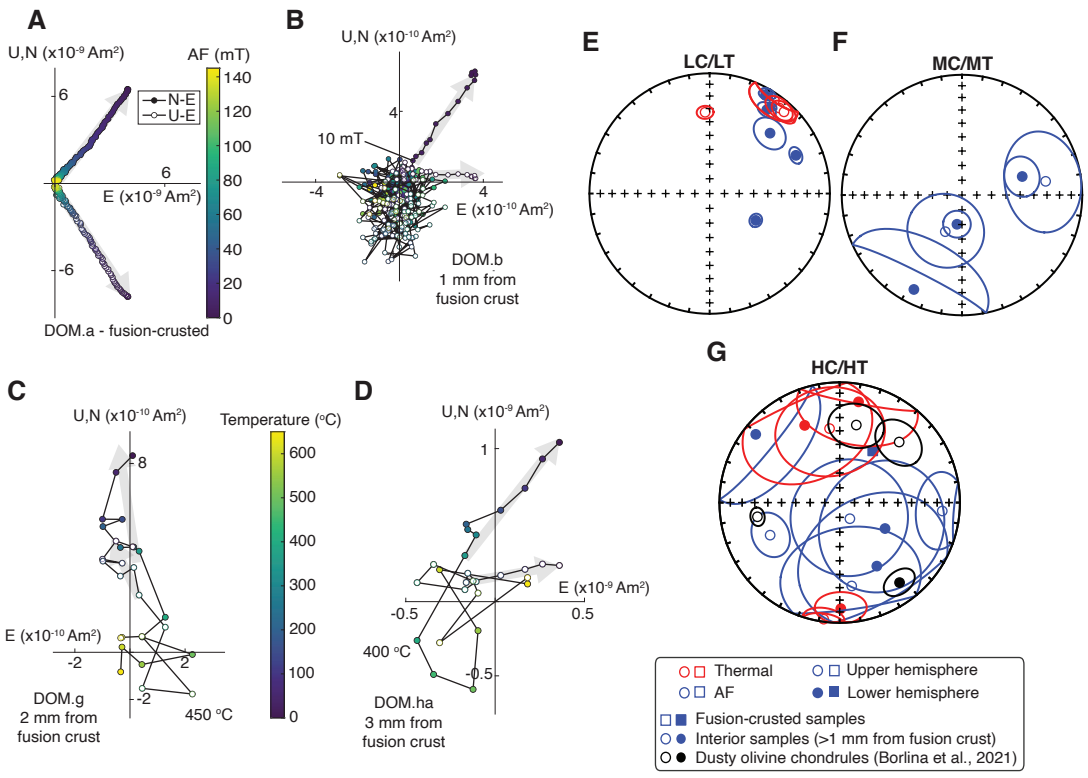

Figure 5-7: **AF and thermal demagnetization of samples from DOM 08006.** Selected orthographic projections of NRM vector endpoints during AF and thermal demagnetization for samples (A) DOM.a, (B) DOM.b, (C) DOM.g and (D) DOM.ha. Closed symbols show the north-east (N-E) projection of the magnetization and open symbols show the up-east (U-E) projection of the magnetization. Selected AF and thermal steps are labeled. (A-B) show AF demagnetization from fusion-crusted and interior samples (>1 mm away from fusion crust), respectively. (C-D) show thermal demagnetization from interior samples. (E-G) show equal area stereonets with the directions of low coercivity/low temperature (LC/LT), medium coercivity/medium temperature (MC/MT) and high coercivity/high temperature (HC/HT) components from all samples measured from DOM 08006. Open and closed symbols represent upper and lower hemispheres, respectively. Red symbols show components from thermal demagnetization, while blue symbols show components from AF demagnetization. Squares show fusion-crusted samples, while circles show interior samples. Black datapoints in equal area stereonet show data from HC components from dusty olivine chondrules from Borlina et al. (2021c).

which yield a paleointensity of 3.4 ± 0.4 μT, which is higher than its fidelity limit of 0.9 μT (Fig. 5-11; Table 5.3). These records are not observed in any of the other subsamples and may be due to the presence of large or highly magnetic chondrules and refractory inclusions in the bulk samples with pre-accretional magnetization and/or

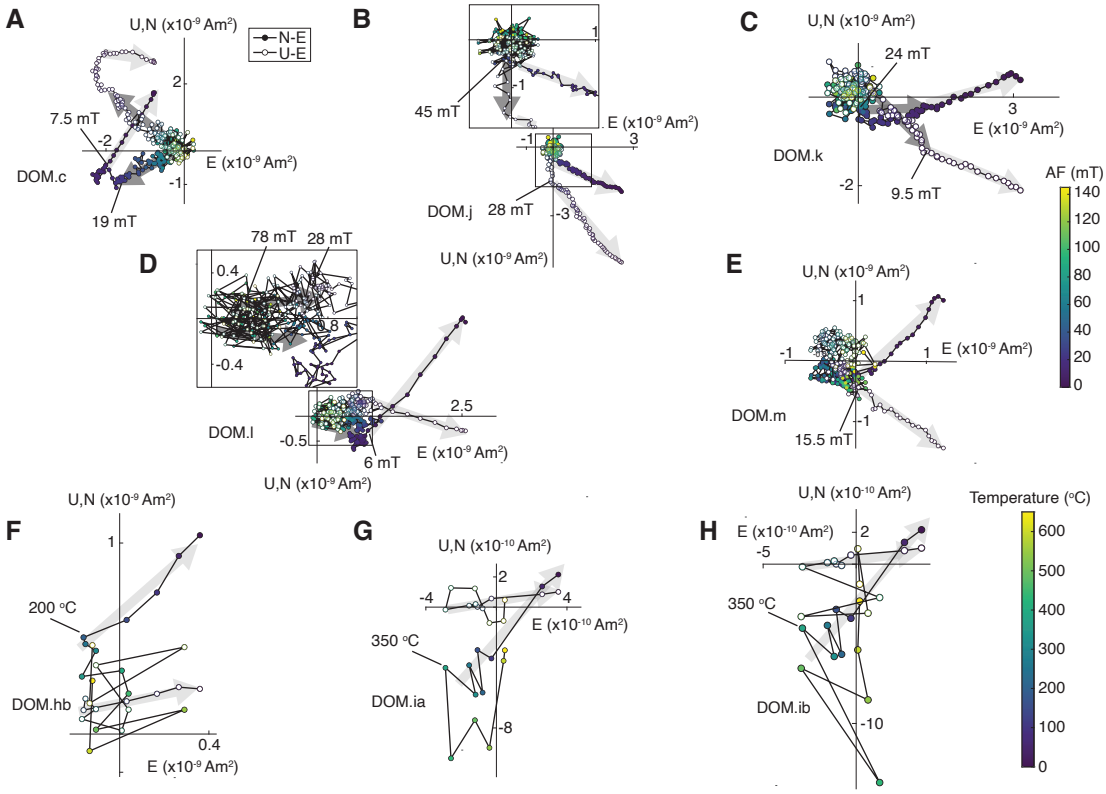

Figure 5-8: **Remaining AF and thermal demagnetization of samples from DOM 08006 showing orthographic projections of NRM vector endpoints during AF and thermal demagnetization for samples (A) DOM.c, (B) DOM.j, (C) DOM.k, (D) DOM.l, (E) DOM.m, (F) DOM.hb, (G) DOM.ia and (H) DOM.ib.** Closed symbols show the north-east (N-E) projection of the magnetization and open symbols show the up-east (U-E) projection of the magnetization. Selected AF and thermal steps are labeled. (A-E) show AF demagnetization from interior samples (>1 mm away from fusion crust). (F-H) show thermal demagnetization from interior samples.

with spurious remanence acquired during AF demagnetization (Weiss et al., 2010). Not including DOM.c and DOM.l results in a mean paleointensity of 0.2 ± 0.4 μT. The fidelity test for interior samples from DOM 08006 (Fig. 5-11; Table 5.3) show that the sample with best fidelity record is DOM.j, recording fields >0.9 µT. We conclude that the HC magnetic record was likely acquired in an environment with paleointensity of <0.9 µT.

The thermal experiments identified LT components (blocked up to 350 ^{o}C) in all samples whose direction is like those of the direction of the LC components (Fig. 5-7). No components were observed blocked above 350 ^{o}C as indicated by a scattered

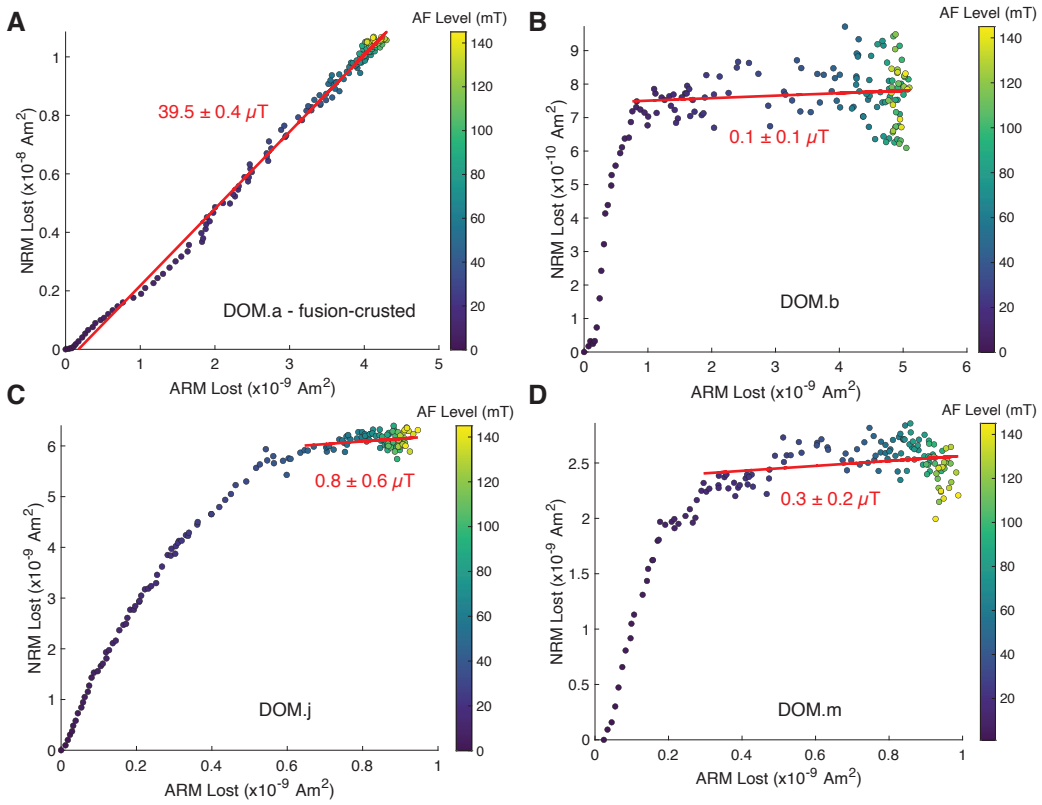

Figure 5-9: **ARM paleointensity experiments for the selected samples (A) DOM.a, (B) DOM.b, (C) DOM.j and (D) DOM.m from DOM 08006.** Shown is NRM lost during stepwise AF demagnetization up to 145 mT and ARM lost during AF demagnetization up to 145 mT of an ARM (AC field of 145 mT with a DC bias field of 50 μT). Paleointensitites ($f' = 3.33$) and their 95% confidence intervals are reported. The red lines represent the range of coercivities used to calculate the fit.

directions and large MADs yielded by PCA fits (Fig. 5-7; Table 5.2). The two samples on which we conducted the IZZI experiment failed multiple PICRIT03 alteration selection criteria. Thus, paleointensities and components direction are unlikely to be robust (Fig. 5-13; Table 5.4).

In summary, the LC/LT/MC/MT components can be associated with low temperature parent body thermochemical alteration and/or VRM acquisition and the fidelity test indicates that the HC range of DOM 08006 recorded a field <0.9 μT.

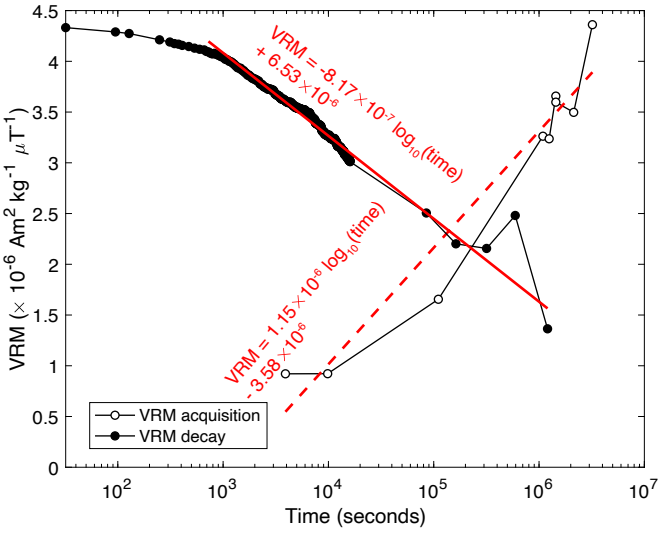

Figure 5-10: **VRM acquisition and decay over a period of ∼40 days of DOM.m, a 1.71 mg sample from DOM 08006.** Closed show measurements of the VRM decay experiment, open symbols show measurements of the VRM acquisition experiment, solid line shows linear fit of the VRM decay experiment, and dashed line shows linear fit of the VRM acquisition experiment.

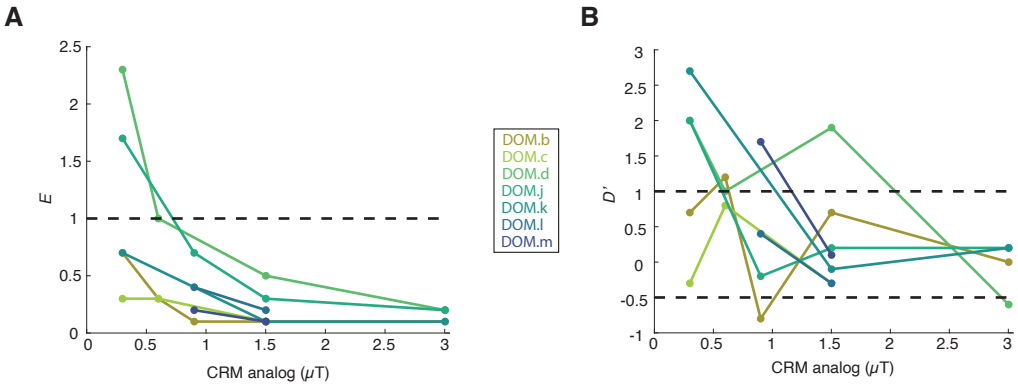

Figure 5-11: E **and** D' **values calculated for samples from DOM 08006.** Values below (A) and between (B) the dashed lines represent reliable paleomagnetic fidelities. The coercivity range, of each sample, used to calculate the paleointensities were used to calculate the E and D' values. The CRM analogs were calculated using $f' = 3.33$ from ARMs (AC field of 145 mT) with DC bias fields of 10, 5, 3 and 1 μT (estimated CRM-equivalent fields of 3, 1.5, 0.9 and 0.3 μT).

5.5 Discussion

In the early solar system, there were at least four sources of magnetic fields that could conceivably have exceeded 0.9 μT: the solar wind magnetic field; impact-generated

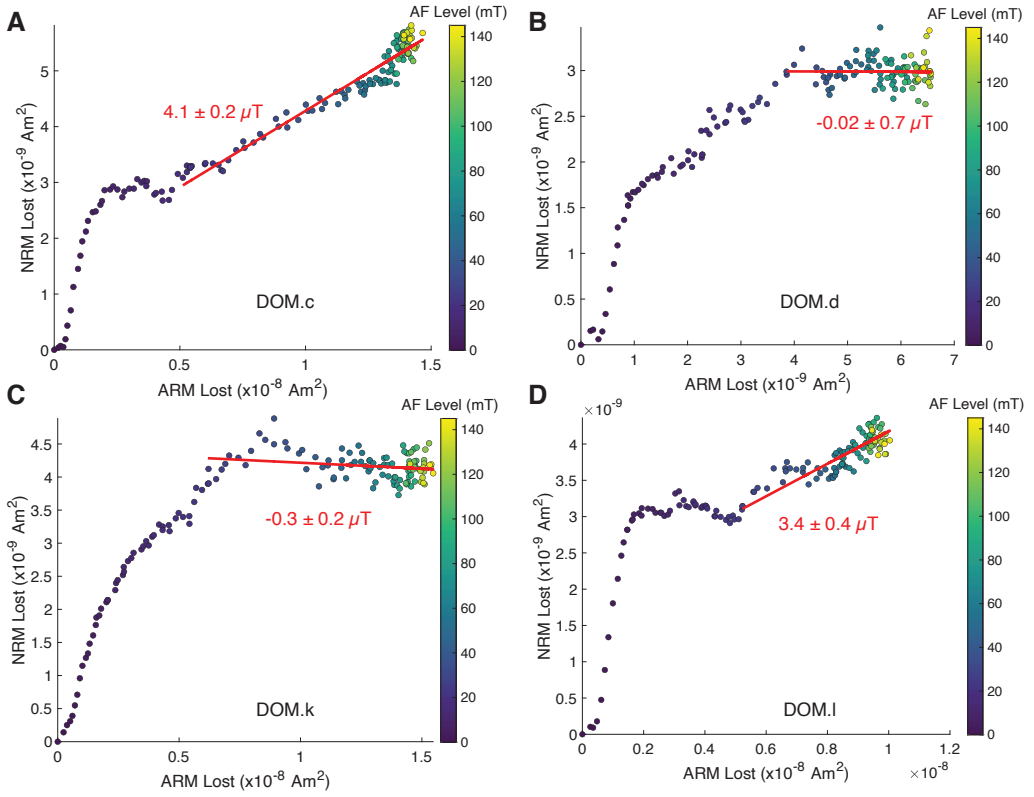

Figure 5-12: **Remaining ARM paleointensity experiments for samples (A) DOM.c, (B) DOM.d, (C) DOM.k and (D) DOM.l from DOM 08006.** Shown is NRM lost during stepwise AF demagnetization up to 145 mT and ARM lost during AF demagnetization up to 145 mT of an ARM (AC field of 145 mT with a DC bias field of 50 μT). Paleointensitites ($f' = 3.33$) and their 95% confidence intervals are reported, along with the red line that represents the range of coercivities used to calculate the fit.

fields; a parent-body core dynamo magnetic field; and the solar nebula magnetic field. Below we discuss the implications of the magnetic record obtained from the CO chondrites and previous measurements for each one of these possibilities. We note that this discussion assumes that the magnetite is capable of having recorded a CRM during parent-body alteration. We discuss below why this might not be the case and future directions to address this.

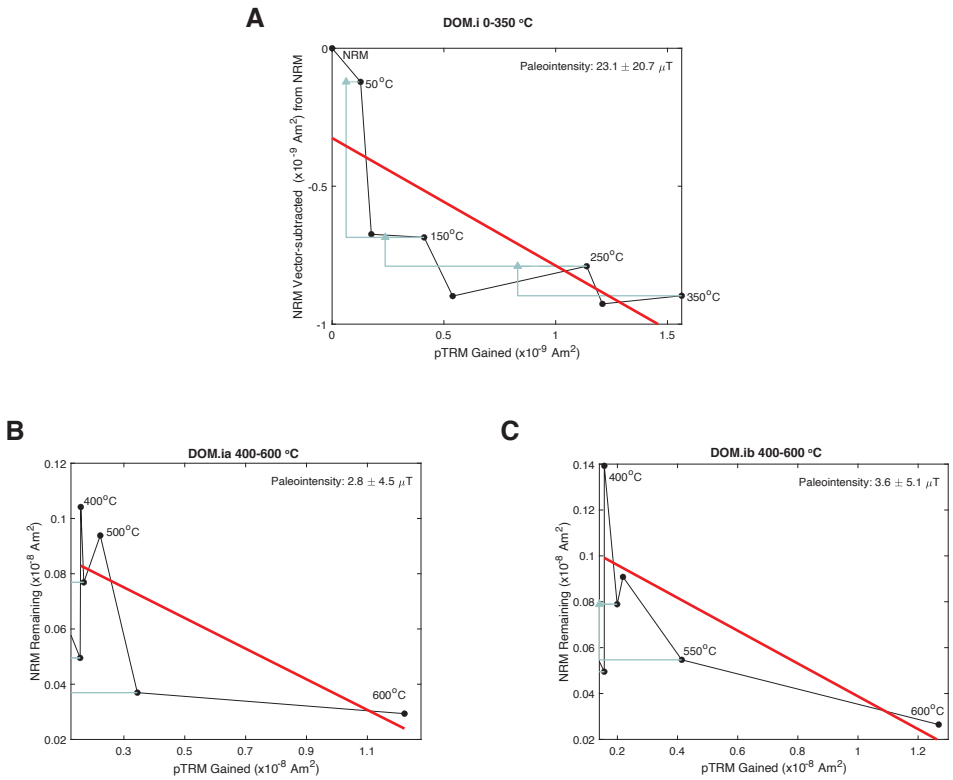

Figure 5-13: **Vector-subtracted NRM from NRM/400 ^{o}C versus partial TRM (pTRM) gained during progressive laboratory heating for samples (A) DOM.i, (B) DOM.ia and (C) DOM.ib from DOM 08006.** Blue triangles show pTRM checks. The red line shows the measurements used to compute paleointensity values. Sample DOM.i split into two subsamples (DOM.ia and DOM.ib) during the 400 ^{o}C step. (A) shows demagnetization of sample DOM.i up to 400 ^{o}C. (B-C) show the remaining demagnetizations for subsamples DOM.ia and DOM.ib.

5.5.1 Implications for the Solar Wind Magnetic Fields

Previous studies have discussed the possibility of the solar wind as a source of remanence recorded by the parent bodies of meteorites (O'Brien et al., 2020; Oran et al., 2018). MHD simulations indicate that the solar wind magnetic field could instantaneously have been amplified to a few μT, but the time-averaged field that would be recorded as a CRM in our meteorites would be several orders of magnitude lower than this value (Oran et al., 2018)). Our findings from CO chondrites place an upper limit to the time-averaged solar wind magnetic field of $<$0.9 μT, consistent with these studies.

5.5.2 Implications for Impact and Dynamos in Planetesimals

Planetesimals have been proposed to have hosted magnetic fields through different mechanisms. A planetesimal dynamo could have been generated by advection of an interior liquid metallic core (Sterenborg and Crowley, 2013). Alternatively, magnetic fields could have been produced transiently during impacts (Weiss et al., 2010). Our records could imply that at the time that the magnetic record was acquired, fields with intensities <0.9 μT (due to a dynamo, crustal remanence from a previous dynamo or impact-generated field) were present on the CO parent. Weak fields such as the upper limit of our measurements are within the values predicted by core dynamo scaling laws (Weiss et al., 2010). Furthermore, models of thermal convection-driven dynamos suggest that field generation could start by 4.5-5 Ma after CAI-formation (Bryson et al., 2019), relatively close to the timing of magnetic acquisition of our samples. In summary, any magnetic field on the parent body at the time of CO magnetization was weaker than <0.9 μT.

5.5.3 Solar Nebular Magnetic Fields and Implications for the Dissipation of PPDs and Planetary Formation

Previous measurements support the presence of nebular fields in the early solar system (Borlina et al., 2021c; Cournede et al., 2015; Fu et al., 2021, 2014). The youngest record of the solar nebula in the inner solar system comes from LL chondrules at 2.03 ± 0.81 Ma after CAI formation (Fu et al., 2014; Weiss et al., 2021), and the youngest record in the outer solar system comes from the CM chondrites at $3.9^{+0.4}_{-0.5}$ Ma after CAI formation (Cournede et al., 2015; Fujiya et al., 2012). We note that I-Xe ages for the CMs have been reported as 2.9 ± 0.39 Ma after CAI formation in the form of an abstract (Pravdivtseva et al., 2013) and recent ^{53}Mn-^{53}Cr ages support a younger alteration time of $3.9^{+0.4}_{-0.5}$ Ma after CAI formation (Fujiya et al., 2012). Fig. 5-14 shows the results of the CO chondrites in context with those of previous studies (Biersteker et al., 2019; Borlina et al., 2021c; Bryson et al., 2017, 2020; Cournede et al., 2015; Fu et al., 2014, 2020b, 2021; Gattacceca et al., 2016; Wang et al., 2017; Weiss

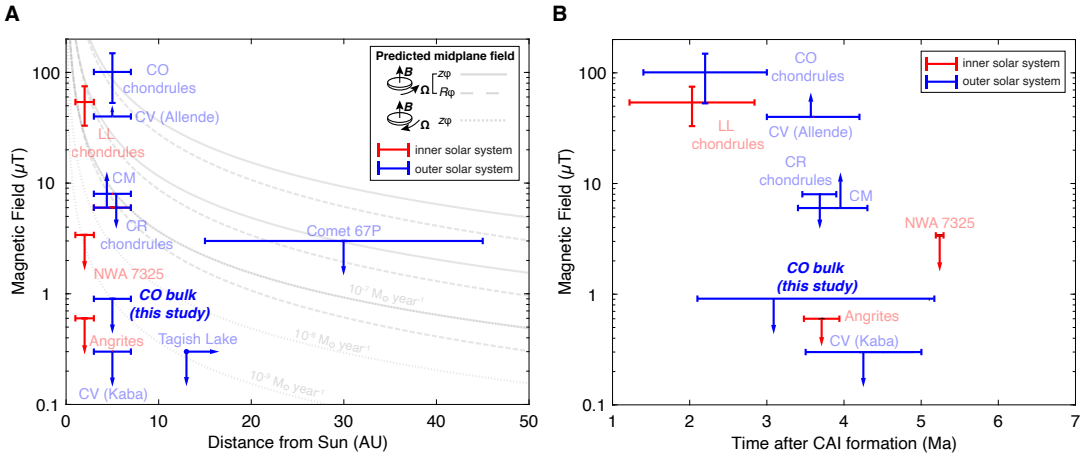

Figure 5-14: **Summary of previous paleomagnetic studies along with results from this study and models of the magnetic field from the solar nebula.** Points show paleomagnetic constraints from LL chondrules (Fu et al., 2014), CO chondrules (Borlina et al., 2021c), bulk NWA 7325 achondrites (Weiss et al., 2017), bulk angrites (Wang et al., 2017), bulk CV (Kaba) chondrites (Gattacceca et al., 2016), Fe-sulfides in CV (Allende) (Fu et al., 2021), CR chondrules (Fu et al., 2020b), Rosetta observations of comet 67P Cheryumov Gerasimenko (Biersteker et al., 2019) and this study. Red symbols show samples that are likely from the inner solar system (<3 AU) and blue symbols show samples that are likely from the outer solar system (>3 AU). (A) Solid lines show predicted midplane magnetic field: solid lines show field due to vertical Maxwell stress [$z\varphi$; eq. 16 of Bai and Goodman (2009)] and dashed lines show field due to radial Maxwell stress ($R\varphi$; eq. 7 of Bai and Goodman (2009)], both assuming the nebular magnetic field and sense of disk rotation are aligned. Dotted lines show the field due to vertical Maxwell stress [$z\varphi$; eq. 7 of Bai and Goodman (2009)] assuming nebular magnetic field and sense of disk rotation are anti-aligned (radial component cancels out for this case). All curves were calculated assuming accretion rates of 10^{-9} (bottom curve), 10^{-8} (middle curve) and 10^{-7} (top curve) $M_\odot$ year^{-1}. (B) Points show paleomagnetic constraints from (A) as a function of age (see text for details on the estimates of the ages).

et al., 2017). We present in Fig. 5-14A magnetic field models as a function of the distance from the Sun. Shown are three set of curves, each assuming magnetic fields drove accretion at rates ranging from 10^-7 to 10^-9 $M_\odot$ year^{-1} as typically observed for actively accreting Young Stellar Objects (Hartmann et al., 1998; Weiss et al., 2021). The first and second curves assume radial-azimuthal and vertical-azimuthal magnetic field stresses driving accretion in the case when the nebular field and the disk angular moment are aligned, while the third curve assumes vertical-azimuthal stresses when the nebular field and the disk rotation are anti-aligned. Recent studies

have supported the presence of magnetic inhomogeneities in the early solar system (Borlina et al., 2021c; Fu et al., 2021), which suggest that magnetic fields might not decay monotonically as proposed by theoretical models of solar nebula magnetic fields.

Measurements from dusty olivine chondrules in LL ordinary chondrites (Fu et al., 2014), are consistent with predictions from magnetically-driven accretion at rates between 10^{-8} and 10^{-7} $M_{\odot}$ year^{-1} and provide lower limits to the accretion rate when compared to that reported by Borlina et al. (2021c) from dusty olivine chondrules in CO chondrites. Comparing the accretion rate inferred from the lower limit of the paleointensity from the LL chondrules (Fu et al., 2014) to the models shown in Fig. 5-14A, we obtain a value of $\sim 10^{-8}$ $M_{\odot}$ year^{-1}. This model assumes an aligned configuration between the magnetic field and rotation of the disk. Under this configuration, a field of $\sim$10 μT would suggest that the solar nebula was still present in the outer solar system. Comparing the CO and CV bulk magnetic records with models that assume accretion rates $>10^{-8}$ $M_{\odot}$ year^{-1}, we observe that the upper limits from this study ($<$0.9 μT) and that of Kaba ($<$0.3 μT) fall below the expected magnetic models by an order of magnitude. Assuming that accretion is magnetically-mediated and that the magnetic field decayed smoothly in the early solar system, the upper limits on the paleointensities of the CO and CV chondrites suggest an absence of nebula in the outer solar system nebula.

^{53}Mn-^{53}Cr ages of fayalite from the CV3 Asuka 881317 indicate an alteration age of $4.2^{+0.8}_{-0.7}$ Ma after CAI formation (Doyle et al., 2014), which is within the error of the I-Xe age from Kaba of 4.50 $\pm$ 1.66 Ma after CAI formation (Pravdivtseva et al., 2013). We note that the Kaba's ^{53}Mn-^{53}Cr age reported in (Gattacceca et al., 2016) used the San Carlos olivine standard that needs to be corrected in future measurements (Doyle et al., 2014). Instead, we adopt the ^{53}Mn-^{53}Cr ages of fayalite from the CV3 Asuka 881317 of $4.2^{+0.8}_{-0.7}$ Ma after CAI formation as the Kaba alteration age (Fig. 5-14B). Together, the CV and CO magnetic data suggest the dissipation of the outer solar system solar nebula by 2.7-5 Ma after CAI-formation, with the CV magnetic record providing the most constrained evidence for the dissipation of the nebula in the

outer solar system of ∼4.2 Ma after CAI-formation. This is broadly consistent with the recent models that suggest that chondrules from the CB carbonaceous chondrites Gujba and Hammadah al Hamra 237, which are thought to have formed, respectively, at $4.6^{+0.5}_{-0.5}$ Ma after CAI formation and $4.5^{+0.9}_{-0.9}$ after CAI formation as a result of high velocity impact between planetesimals in an environment where the nebular gas had already dissipated (Krot et al., 2005) and with simulations of these impacts that indicate that the nebula dissipated by 5 Ma after CAI formation (Johnson et al., 2016).

We can now establish the dissipation time of the solar nebula between the inner and outer solar system as well as within the outer solar system. Magnetic measurements suggest that the inner solar nebula dissipated by 3.71 ± 0.23 Ma after CAI formation (Wang et al., 2017; Weiss et al., 2021). Comparing the angrite age with that of the CV chondrites would suggest that the solar nebula dissipated within <1.5 Ma between the two reservoirs. If, independently, we compare the CM chondrite age with that of the CV chondrites, we obtain a dispersal time in the outer solar system solar nebula of <1.6 Ma after the CM magnetic record. These two upper limits on the differential dissipation time between and within the reservoirs suggest a rapid dissipation of the disk: together with the evidence that the disk existed for at least ∼3 Ma, it overall supports a dual-timescale evolution of the solar system PPD. Models suggest that a two-timescale evolution of the disk is consistent with magnetically-driven and/or photoevaporative winds predominately driving PPD dissipation (Armitage et al., 2013; Clarke et al., 2001; Shadmehri and Ghoreyshi, 2019) with potential influence of external photoevaporation aided by other stars (Concha-Ramírez et al., 2019).

Finally, the dissipation of the disk sets the limit for the accretion of gas to the gas giants (Weiss and Bottke, 2021). Thus, if we take the age of the CVs as the first evidence for the dissipation of the solar nebula in the outer solar system that indicates that the gas giants stopped accreting mass sometime between 3.5-5 Ma after CAI formation.

5.6 Future Directions for Solar Nebula Paleomagnetism

While previous measurements (Cournede et al., 2015; Fu et al., 2021; Gattacceca et al., 2016) and those reported in this study can potentially provide important information about the lifetime of the solar nebula, two key aspects that are fundamental to obtaining robust records of the solar nebula remain largely unconstrained. First, additional high-precision ages from meteorites are necessary. Determining when alteration occurred in various meteorite parent bodies is crucial to establish when CRMs may have been acquired. Future studies that include age measurements of the alteration products in the meteorites (ideally dating the formation of the ferromagnetic minerals of interest), including CO chondrites, will be able to provide the precision necessary to establish more precise timing of the solar nebula dispersal.

Second, as briefly discussed in section 2.2, the CRM to ARM ratio for magnetite that formed during aqueous alteration of metal is undetermined. While chondrules and refractory inclusions likely acquired TRMs due to their pre-accretionary thermal histories, the magnetic record of bulk aqueously altered samples is usually carried in the form of CRMs. Unfortunately, very little is known about the mechanism of CRM acquisition during parent-body alteration and how it can affect the recovered paleointensity. A recent study suggests that magnetite can form through different pathways in chondrites (Sridhar et al., 2021). Magnetite grains in most CM and CO chondrites likely formed through pseudomorphic replacement of metal, while magnetite in framboids and plaquettes, which are found in comparatively high abundance inseveral chondrites including the CM Paris, are thought to have formed through the dissolution of sulfide and precipitation of magnetite in these exotic morphologies. For the case that magnetite forms through replacement of metal, previous studies of alteration pseudomorphic reactions in terrestrial samples have observed that certain minerals can inherent the NRM carried by the precursor phase (Heider and Dunlop, 1987; Jiang et al., 2017). Because FeNi metal across a bulk chondrite subsample is expected to carry a non-uniform remanence (because it will carry several non-unidirectional pre-

accretionary remanences), it is possible that the absence of a remanence recorded by magnetite corresponds to a signal inherited from the metal. This could fundamentally impact the paleointensities obtained from CRMs carried by magnetite in CM chondrites (Cournede et al., 2015), CV chondrites (Fu et al., 2021; Gattacceca et al., 2016) and CO chondrites in this study. For the CMs, for example, the lack of HT components that demagnetize between the Curie temperatures of pyrrhotite and magnetite in most CM chondrites from Cournede et al. (2015) was interpreted to be due to alteration during laboratory heating. A second interpretation is that the magnetite inherited the remanence from its parent metal and, as a result, does not contain a HT component associated with magnetite. This interpretation is consistent with pyrrhotite in CM chondrites carrying a CRM, indicating that a field was seemingly present at some point during the alteration sequence of these meteorites, but there being no record of this remanence in the magnetite among most meteorites in this group. Notably, the magnetite in Paris does appear to carry a CRM, which is consistent with this meteorite containing a large proportion of magnetite framboids and plaquettes that are likely to have recorded more traditional CRMs as the grains in these morphologies grew through their blocking volumes as they were precipitated. This interpretation could also explain the absence of a remanence in the CV Kaba at temperatures above the peak metamorphic temperature reached on the parent body (Gattacceca et al., 2016). This would suggest that the absence of a remanence may in fact not reflect the dissipation of the disk and its associated field, but instead the inability of magnetite to record a remanence when it forms through aqueous alteration of metal. To determine whether robust records of the solar nebula can in fact be recovered from bulk samples of aqueously altered chondrites, it is crucial to conduct experimental work to determine how magnetite in different families of chondrites and how they could acquire CRMs.

5.7 Conclusion

We report paleomagnetic measurements of bulk matrix-rich samples from the CO chondrites ALHA77307 and DOM 08006. Assuming that magnetite could have recorded ambient fields during parent-body alteration, the CO chondrite records indicate that the ambient field was <0.9 μT. Combining these results with previous paleomagnetic measurements, we suggest that the nebular gas in the carbonaceous chondrite region ($\sim$3-7 AU) dissipated within 3.5-5 Ma after CAI formation. Comparing the time of the dissipation of the nebula in the outer solar system with that from the inner solar system indicates that the difference in dissipation ages between the two reservoirs was $<$1.5 Ma. This supports a dual-timescale evolution of the solar system PPD, consistent with magnetically driven winds and/or photoevaporation as processes that mediated the dissipation the solar system PPD. Additionally, the end of the solar nebula indicated that the gas giants stopped accreting by 3.5-5 Ma after CAI formation. We also highlight future work necessary for the field of solar nebula paleomagnetism which includes obtaining more ages from alteration products to obtain high-resolution temporal records from the nebula. We also highlight issues in using magnetite in bulk carbonaceous chondrites to determine nebula field records and the future work necessary for such records to be acquired, as well as obtaining more ages from alteration products to obtain high-resolution temporal records from the nebula. We also discuss how there is a possibility that paleomagnetic measurements of carbonaceous chondrites that have been interpreted as evidence for the absence of a field in the solar nebula, including this study, might be a result of non-ideal magnetic acquisition during parent-body alteration. Overall, future experimental work to understand the mechanisms of CRM acquisition in parent-bodies is critical to reliably obtain records of the solar nebula.

5.8 Appendix

5.8.1 Magnetic record from matrix dominates bulk samples

An average bulk sample used in this study has a volume of ∼1 mm^3 = 1×10^{-9} m^3. In DOM 08006, chondrules represent 67% of the volume in the bulk material with an average radius of 133 μm (Davidson et al., 2019). Assuming that a chondrule is a sphere, the average volume of a chondrule in a CO chondrite is of 9.9×10^{-12} m^3. Thus, a typical bulk size sample from a CO chondrite used in this study has ∼68 chondrules. The expected net moment M of the summation of N chondrules that are randomly located in bulk samples with a magnetic moment m is given as $M = m\sqrt{N}$ (Biersteker et al., 2019; Heslop, 2007). The average value of m for dusty olivine chondrules in CO chondrites is 3.7×10^{-11} Am^2 (Borlina et al., 2021c). If we assume the magnetic moment of dusty olivine chondrules to be representative of all chondrules in CO chondrites, an upper limit of the expected magnetic contribution from all chondrules in a typical bulk size sample is ∼9.6×10^{-10} Am^2 or ∼0.96 Am^{-1}. However, dusty olivine chondrules only represent 1 in 100 chondrules in CO chondrites; if we were to instead assume that only dusty olivine chondrule carry magnetic moments in bulk samples, we obtain a lower limit on the moment contribution from chondrules of ∼3.1×10^{-11} Am^2 or 0.031 Am^{-1}. From the NRM measurements of DOM 08006 reported here, the average bulk sample has an NRM moment of 2.3×10^{-9} Am^2 or magnetization 2.3 Am^{-1}. This value is at least two times greater than 0.96 Am^{-1}, which represents the overestimation of the magnetic moment of the chondrule population, and two orders of magnitude higher than our lower limit of 0.031 Am^{-1}. Thus, matrix material is likely to dominate the magnetic record of bulk samples.

Table 5.1: **PCA fits for ALHA77307**. The first column shows the sample name, the second shows the weight (in mg) of the sample, the third shows the distance from the fusion crust (in mm; "fusion-crusted" if the sample contained fusion crust), the fourth shows the name of the component (LC = low coercivity, MC = medium coercivity, HC = high coercivity, LT = low temperature and HT = high temperature) with "*" indicating a non-magnetized range, the fifth shows the range of levels/temperatures used in the PCA fit (in mT or ^{o}C), the sixth shows the number of data points in the PCA fit, the seventh, eighth and nineth show the declination, inclination and maximum angular deviation (MAD) for the fit without anchoring to the origin, the tenth shows the deviation angle (DANG) between anchored and non-origin-anchored fits, the eleventh, twelfth and thirteenth show the origin-anchored declination, origin-anchored inclination and origin-anchored MAD for the fits, and the fourteenth shows the NRM to ARM (AC field of 145 mT with a DC bias field of 50 μT) ratio.

Sample	Weight (mg)	Distance from fusion crust (mm)	Component	Range (mT or °C)	N	Declination (°)	Inclination (°)	MAD (°)	DANG (°)	Anchored Declination (°)	Anchored Inclination (°)	Anchored MAD (°)	NRM/ARM
ALHA.a	5.51	fusion crusted	LC	0-20.5 mT	41	118.5	-4.9	4.6					4.8
			HC	26-410 mT	125	288.6	9.4	3.4	2.4	289.8	9.1	2.7	
ALHA.b	7.68	1.8	LC	0-39 mT	64	148.1	11.5	1.1	2.5	149	12.1	1.5	2.1
			HC*	39-145 mT	87	175.5	3.7	33.7					
ALHA.c	9.03	3.2	LC	0-58 mT	83	155.5	18.4	1.8	3.4	154.7	17.6	2.2	2.2
			HC*	58-145 mT	68	358	-1.3	40.9					
ALHA.d	6.15	4.9	LC	0-55 mT	80	163.2	15.8	3.6	4.1	161.7	14.8	3.4	1
			HC*	55-145 mT	71	157.5	11.7	38.6					
ALHA.e	1.1	fusion crusted	LC	0-18.5 mT	36	119.3	-20.3	3.9					
			HT	251-580 °C	17	277.4	0	10.9	19.2	290.7	0.7	10.7	
ALHA.f	0.6	fusion crusted	LC	0-19 mT	39	123.7	-11	5.1					
			HT	251-580 °C	20	281.3	9.1	16.1	20.8	294.7	6.7	10.5	
ALHA.g	2	4.5	LT	0-425 °C	11	158.9	5.6	5.7					
			HT*	425-580 °C	12	357.1	-3.3	33.5	34.9	357.8	27.7	19.8	
ALHA.h	0.6	5.8	LC	0-21 mT	42	152.8	6.5	5.5					
			LT	51-375 °C	8	112.9	-2.1	33.9	32.9	144.1	-4.5	14.1	
			HT*	375-570 °C	13	160.8	-6.6	30.5					

Table 5.2: **PCA fits for DOM 08006**. The first column shows the sample name, the second shows the weight (in mg) of the sample, the third shows the distance from the fusion crust (in mm; "fusion-crusted" if the sample contained fusion crust), the fourth shows the name of the component (LC = low coercivity, MC = medium coercivity, HC = high coercivity, LT = low temperature and HT = high temperature), the fifth shows the range of levels/temperatures used in the PCA fit (in mT or ^{o}C), the sixth shows the number of data points in the PCA fit, the seventh, eighth and nineth show the declination, inclination and maximum angular deviation (MAD) for the fit without anchoring to the origin, the tenth shows the deviation angle (DANG) between anchored and non-origin-anchored fits, the eleventh, twelfth and thirteenth show the origin-anchored declination, origin-anchored inclination and origin-anchored MAD for the fits, and the fourteenth shows the NRM to ARM (AC field of 145 mT with a DC bias field of 50 μT) ratio.

Sample	Weight (mg)	Distance from fusion crust (mm)	Component	Range (mT or °C)	N	Declination (°)	Inclination (°)	MAD (°)	DANG (°)	Anchored Declination (°)	Anchored Inclination (°)	Anchored MAD (°)	NRM/ARM
DOM.a	1.03	fusion crusted	HC	0-145 mT	150	32.8	46.9	2.2	1.6	32.6	47.7	1.8	2.75
DOM.b	1.37	1	LC	0-10 mT	20	30.4	3.9	4	12.6	30.4	-4	6.6	0.14
			HC*	10-145 mT	131	147.7	-77.1	40.3					
DOM.c	2.34	2	LC	0-7.5 mT	15	29.6	6.7	3.7					0.04
			HC	19-145 mT	113	236.3	-37.6	17.3	13.3	244.9	-36.3	13.9	
DOM.d	1.61	3.1	LC	0-6 mT	12	34.3	16.8	5.5					0.27
			MC	6-17.5 mT	24	80.7	-30.2	30					
			MC	17.5-32 mT	23	204.5	-62.6	25.6	48.9	303.4	-54.7	13.4	
			HC*	32-145 mT	94	309.1	11	39					
DOM.j	1.75	7.6	LC	0-28 mT	53	120.2	53.4	4.4					0.64
			MC	28-45 mT	18	200.8	75.4	18.8	7.9	189.8	69.9	9.2	
			HC*	45-145 mT	81	149.7	38.7	49					
DOM.k	3.28	6.9	LC	0-9.5 mT	19	66.1	22.6	4.9					0.24
			MC	9.5-24 mT	30	72.9	46.5	12.8	39.5	114	32.1	14.8	
			HC*	24-145 mT	103	171.8	-30.6	42.3					
DOM.l	3.5	5.8	LC	0-6 mT	12	35.6	11.7	2.6					0.33
			MC (?)	6-28 mT	42	207	12.9	40.3					
			HC	28-145 mT	98	100.4	-22.7	35.2	11.3	94.7	-15.5	21	
DOM.m	1.71	4.8	LC	1-15.5 mT	30	45	29.7	10.6	37.9	57.5	50.1	19.8	0.22
			HC*	15.5-145 mT	120	119.8	54.2	44.4					
DOM.g	1.78	2	0-350 °C	8	357.1	-23.2	20.2	10	356.8	-32.8	5		
			HT*	350-650 °C	7	352.2	-37.9	33.8					
DOM.ha	1.13	3	0-350 °C	8	39.2	-9.1	8.2						
			HT*	350-650 °C	7	10.6	15.9	33.4					
DOM.hb	2.23	3.1	0-200 °C	5	42.3	-9	7.4						
			HT*	200-650 °C	10	335.6	30.2	40.2					
DOM.ia	2.71	3.8	0-350 °C	8	34.8	-6.4	13.9						
			HT*	400-600 °C	5	198.8	-6.1	20.1	13.8	187.8	-2.4	10.1	
DOM.ib	0.67	3.8	0-350 °C	8	34.8	-6.4	13.9						
			HT*	400-600 °C	5	171.5	8.8	27.1	10.6	179.4	12.8	13.7	

Table 5.3: **Paleointensities from the ARM experiment with samples from ALHA77307 and DOM 08006**. The first column shows the sample name, the second shows the distance from the fusion crust (in mm; "fusion-crusted" if the sample contained fusion crust), the third shows the range of AF levels used in the paleointensity fit (in mT), the fourth shows the number of datapoints used in the paleointensity fit, the fifth shows the parametric correlation (ρ) between NRM and ARM datasets, the sixth shows the type of fit used to calculate the paleointensity (OLS = ordinary least square; RMA = reduced major axis), the seventh shows the paleointensity (in μT), the eighth shows the calculated 95% confidence interval of the paleointensity fit (in μT) and the nineth shows the recording limit of the sample (in μT). For each sample (ALHA77307 and DOM 08006) we calculated mean paleointensities and the 95% confidence interval.

Sample	Distance from fusion crust (mm)	Range (mT)	N	ρ	Fit Type	Paleofield (μT)	95% conf. int. (μT)	Recording limit (μT)
ALHA.a	fusion crusted	0-10	20	1	OLS	358.5	15.8	-
		26-145	100	0.99	RMA	26.7	0.8	-
ALHA.b	7.68	0-10	20	0.99	OLS	206.9	10.2	-
		39-145	87	0.8	RMA	2	0.3	-
ALHA.c	3.2	0-9	18	0.99	OLS	247.7	16.3	-
		55-145	71	0.5	OLS	1.5	0.5	> 1.5
ALHA.d	4.9	0-10	20	0.99	OLS	113.3	7.3	-
		55-145	71	0.54	OLS	3	0.6	> 0.9
					Mean*	**2.2**	*only high coercvity and no fusion crust	
					95% conf. int	**0.9**		
DOM.a	fusion crusted	0-145	150	1	RMA	39.5	0.4	-
DOM.b	0.9	0-10	20	0.97	OLS	16.4	2.2	-
		10-145	131	0.14	OLS	0.1	0.1	> 1.5
DOM.c	2	0-7.5	15	0.98	OLS	28	3.4	-
		19-145	113	0.97	RMA	4.1	0.2	> 0.3
DOM.d	3.1	0-6	12	0.93	OLS	29.5	8.1	-
		6-17.5	24	0.94	RMA	5.4	0.8	-
		17.5-32	23	0.87	RMA	6.4	1.5	-
		32-145	94	-	OLS	-0.02	0.7	> 3
DOM.j	7.6	0-28	53	1	RMA	18.5	0.6	-
		28-45	18	1	OLS	7.1	1.8	-
		45-145	81	0.27	OLS	0.8	0.6	> 0.9
DOM.k	6.9	0-9.5	19	1	OLS	17.9	1.3	-
		9.5-24	30	0.97	RMA	5.7	0.5	-
		24-145	103	-	OLS	-0.3	0.2	> 1.5
DOM.l	5.8	0-6	12	0.97	OLS	34.1	5.7	-
		28-145	98	0.83	RMA	3.4	0.4	> 0.9
DOM.m	4.8	1-15.5	30	0.94	RMA	12.9	1.6	-
		15.5-145	120	0.3	OLS	0.3	0.2	> 1.5
					Mean**	**1.2**	**only high coercvity and no fusion crust	
					95% conf. int	**1.4**		
					Mean***	**0.2**	***only high coercvity, no fusion crust, DOM.c and DOM.l not included	
					95% conf. int	**0.4**		

Table 5.4: **Paleointensities and calculated paleomagnetic criteria [PICRIT03 from Paterson et al. (2014)] from the IZZI experiment for ALHA77307 and DOM 08006**. The first column shows the sample name, the second shows the distance from the fusion crust (in mm; "fusion-crusted" if the sample contained fusion crust), the third shows the range of temperatures used in the paleointensity fit (in ^{o}C), the fourth shows the number of datapoints used in the fit, the fifth shows the paleointensity (in μT), the sixth shows the calculated 95% confidence interval of the paleointensity fit (in μT), the seventh, eighth, nineth, tenth, eleventh and twelfth show the paleomagnetic parameters DRATS, f, β, q, CDRAT and maximum DRAT from Paterson et al. (2014), and the thirteenth shows the number of partial TRM (pTRM) checks conducted during the IZZI experiment.

Sample	Distance from fusion crust (mm)	Range (^{o}C)	N	Lab field direction (dec,inc) (°)	Paleofield (μT)	95% conf int (μT)	DRATS	f	β	q	CDRAT	max. DRAT	number of pTRM checks
ALHA.e	fusion crust	400-580	13	(360,0)	13.9	4.7	5	1.1	0.3	2.8	5.1	17.8	6
ALHA.f	fusion crust	400-580	13	(360,0)	13.9	5.4	0.5	1	0.4	2.3	0.5	7.8	6
ALHA.g	4.5	540-580	12	(360,0)	1.5	8.9	34.6	0.4	5.9	-0.1	51.9	23.4	6
ALHA.h	5.8	475-580	10	(360,0)	-7.3	10.2	3	1.5	1.4	-0.8	3.9	62.8	6
DOM.ia	3.8	0-350	8	(180,0)	23.1	20.7	35	2.5	0.9	2.2	30.4	17.1	3
		400-600	5		2.8	4.5	13	0.7	1.6	0.2	14.9	4.9	5
DOM.ib	3.8	0-350	8	(180,0)	23.1	20.7	35	2.5	0.9	2.2	30.4	17.1	3
		400-600	5		3.6	5.1	13	0.9	1.4	0.4	14.7	5.3	5

Part IV

Conclusions and Future Research

Chapter 6

Future Research

6.1 Determining the evolution of Earth's magnetic field

Determining the evolution of Earth's magnetic field is crucial to understand how planetary magnetic fields are generated, the thermal structure of planets and the potential impact of magnetic fields in controlling habitability of planets. As discussed in Chapter 2 and Borlina et al. (2020), Earth's oldest relics, the Jack Hills zircon grains, are not robust paleomagnetic targets. In fact, a recent study by Fu et al. (2020a) showed that even 3.5-4.0 billion years (Ga) old zircons from the Barberton Greenstone Belt, South Africa, are not robust paleomagnetic targets. This suggests that the majority of ancient zircon grains are not ideal paleomagnetic targets. Thus, determining what Earth's magnetic field looked like before 3.5 Ga will require identifying new outcrops and/or single crystals that are older than 3.5 Ga and that could have recorded the ancient dynamo. Finally, on-going work is attempting to obtain extremely high-resolution temporal records of short-term variations of Earth's magnetic field that can provide insights about the fundamental mechanisms that drive planetary magnetism (Borlina et al., 2021a).

6.2 Obtaining Solar Nebula Magnetic Records

Future studies should focus on two main directions. The first one involves further exploring the magnetism of CAIs and chondrules. The work presented in Chapter 3 suggests that CAIs can provide records of the very beginning of the solar system. This study opens the possibility to explore the magnetism of CAIs from different families of meteorites. Additionally, the work presented in Borlina et al. (2021c) and Chapter 4 indicate that we can obtain reliable records from $\sim$100 μm chondrules. In lieu of that, there are many families of meteorites that we can target to obtain obtain magnetic records from dusty olivine chondrules. The second direction involves understanding how crystallization remanent magnetization (CRM) is acquired by magnetite in chondrites during parent-body alteration. While previous work and the work in Chapter 5 provide important constraints on how the solar nebula dissipated, there is work that has to be done specifically to obtain more ages of meteorites and experimental work to understand CRM acquisition.

Bibliography

Alexander, C. M. O., Fogel, M., Yabuta, H., and Cody, G. D. (2007). The origin and evolution of chondrites recorded in the elemental and isotopic compositions of their macromolecular organic matter. *Geochimica et Cosmochimica Acta*, 71(17):4380–4403.

Alexander, C. M. O., Greenwood, R. C., Bowden, R., Gibson, J. M., Howard, K. T., and Franchi, I. A. (2018). A mutli-technique search for the most primitive CO chondrites. *Geochimica et Cosmochimica Acta*, 221:406–420.

Alexander, R. D., Clarke, C. J., and Pringle, J. E. (2006). Photoevaporation of protoplanetary discs – II. Evolutionary models and observable properties. *Monthly Notices of the Royal Astronomical Society*, 369(1):229–239.

Anderson, B. J., Johnson, C. L., Korth, H., Purucker, M. E., Winslow, R. M., Slavin, J. A., Solomon, S. C., McNutt, R. L., Raines, J. M., and Zurbuchen, T. H. (2011). The Global Magnetic Field of Mercury from MESSENGER Orbital Observations. *Science*, 333(6051):1859–1862. Publisher: American Association for the Advancement of Science.

Andrews, S. M. (2020). Observations of Protoplanetary Disk Structures. *Annual Review of Astronomy and Astrophysics*, 58(1):483–528. Publisher: Annual Reviews.

Armitage, P. J. and Kley, W. (2019). *From Protoplanetary Disks to Planet Formation: Saas-Fee Advanced Course 45. Swiss Society for Astrophysics and Astronomy*. Saas-Fee Advanced Course. Springer-Verlag, Berlin Heidelberg.

Armitage, P. J., Simon, J. B., and Martin, R. G. (2013). Two Timescale Dispersal of Magnetized Protplanetary Disks. *The Astrophysical Journal*, 778(1):L14. Publisher: IOP Publishing.

Armstrong, J. T. (1995). CITZAF: A package of correction programs for the quantitative Electron Microbeam X-Ray-Analysis of thick polished materials, thin-films, and particles. *Microbeam Analysis*, 4(3):177–200. Publisher: VCH PUBLISHERS INC 303 NW 12TH AVE, DEERFIELD BEACH, FL 33442-1788.

Atreya, S. K., Crida, A., Guillot, T., Lunine, J. I., Madhusudhan, N., and Mousis, O. (2018). weiss. In *Saturn in the 21st Century*, pages 5–43. Cambridge University Press, Cambridge.

Audard, M., Ábrahám, P., Dunham, M. M., Green, J. D., Grosso, N., Hamaguchi, K., Kastner, J. H., Kóspál, , Lodato, G., Romanova, M. M., Skinner, S. L., Vorobyov, E. I., and Zhu, Z. (2014). *Episodic Accretion in Young Stars*. eprint: arXiv:1401.3368. Conference Name: Protostars and Planets VI Pages: 387 ADS Bibcode: 2014prpl.conf..387A.

Bai, X. (2016). Toward a global evolutionary model of protoplanetary disks. *Astrophys. J.*, 821:80.

Bai, X.-N. (2017). Global Simulations of the Inner Regions of Protoplanetary Disks with Comprehensive Disk Microphysics. *The Astrophysical Journal*, 845(1):75. Publisher: IOP Publishing.

Bai, X.-N. and Goodman, J. (2009). Heat and dust in active layers of protostellar disks. *The Astrophysical Journal*, 701(1):737–755.

Bell, E. A., Boehnke, P., Hopkins-Wielicki, M. D., and Harrison, T. M. (2015). Distinguishing primary and secondary inclusion assemblages in Jack Hills zircons. *Lithos*, 234-235:15–26.

Biersteker, J. B., Weiss, B. P., Heinisch, P., Herčik, D., Glassmeier, K.-H., and Auster, H.-U. (2019). Implications of Philae Magnetometry Measurements at Comet 67P/Churyumov–Gerasimenko for the Nebular Field of the Outer Solar System. *The Astrophysical Journal*, 875(1):39. Publisher: American Astronomical Society.

Bonal, L., Bourot-Denise, M., Quirico, E., Montagnac, G., and Lewin, E. (2007). Organic matter and metamorphic history of CO chondrites. *Geochimica et Cosmochimica Acta*, 71(6):1605–1623.

Bonal, L., Quirico, E., Flandinet, L., and Montagnac, G. (2016). Thermal history of type 3 chondrites from the Antarctic meteorite collection determined by Raman spectroscopy of their polyaromatic carbonaceous matter. *Geochimica et Cosmochimica Acta*, 189:312–337.

Borlina, C. S., Lima, E. A., Feinberg, J. M., Lascu, I., Trindade, R. I. F., and Weiss, B. P. (2021a). Using SQUID Microscopy to Obtain High Resolution Paleomagnetic Records from Speleothem. *AGU Fall Meeting*.

Borlina, C. S., Weiss, B. P., Bryson, J. F. J., Bai, X. N., and Lima, E. A. (2021b). Evidence for Non-Steady Accretion in the Solar Nebula Inferred from Paleomagnetism of CO Chondrules. *52nd Lunar and Planetary Science Conference*, page 2546.

Borlina, C. S., Weiss, B. P., Bryson, J. F. J., Bai, X.-N., Lima, E. A., Chatterjee, N., and Mansbach, E. N. (2021c). Paleomagnetic evidence for a disk substructure in the early solar system. *Science Advances*, 7(42):eabj6928. Publisher: American Association for the Advancement of Science.

Borlina, C. S., Weiss, B. P., Lima, E. A., Tang, F., Taylor, R. J. M., Einsle, J. F., Harrison, R. J., Fu, R. R., Bell, E. A., Alexander, E. W., Kirkpatrick, H. M., Wielicki, M. M., Harrison, T. M., Ramezani, J., and Maloof, A. C. (2020). Reevaluating the evidence for a Hadean-Eoarchean dynamo. *Science Advances*, 6(15):eaav9634. Publisher: American Association for the Advancement of Science Section: Research Article.

Bouvier, A., Brennecka, G. A., and Wadhwa, M. (2011). Absolute chronology of the first solids in the solar system. volume 1639, page abstract #9054.

Brasser, R. and Mojzsis, S. J. (2020). The partitioning of the inner and outer Solar System by a structured protoplanetary disk. *Nature Astronomy*, 4(5):492–499. Number: 5 Publisher: Nature Publishing Group.

Brennecka, G. A., Burkhardt, C., Budde, G., Kruijer, T. S., Nimmo, F., and Kleine, T. (2020). Astronomical context of Solar System formation from molybdenum isotopes in meteorite inclusions. *Science*, 370(6518):837–840. Publisher: American Association for the Advancement of Science Section: Report.

Brennecka, G. A., Burkhardt, C., Nimmo, F., Kruijer, T. S., and Kleine, T. (2018). Molybdenum isotopic evidence for a distal formation of refractory inclusions. volume 49, page 2429.

Bryson, J. F. J., Neufeld, J. A., and Nimmo, F. (2019). Constraints on asteroid magnetic field evolution and the radii of meteorite parent bodies from thermal modelling. *Earth and Planetary Science Letters*, 521:68–78.

Bryson, J. F. J., Weiss, B. P., Harrison, R. J., Herrero-Albillos, J., and Kronast, F. (2017). Paleomagnetic evidence for dynamo activity driven by inward crystallisation of a metallic asteroid. *Earth and Planetary Science Letters*, 472:152–163.

Bryson, J. F. J., Weiss, B. P., Lima, E. A., Gattacceca, J., and Cassata, W. S. (2020). Evidence for Asteroid Scattering and Distal Solar System Solids From Meteorite Paleomagnetism. *The Astrophysical Journal*, 892(2):126. Publisher: American Astronomical Society.

Carporzen, L., Weiss, B. P., Elkins-Tanton, L. T., Shuster, D. L., Ebel, D. S., and Gattacceca, J. (2011). Magnetic evidence for a partially differentiated carbonaceous chondrite parent body. *Proc. Natl. Acad. Sci. USA*, 108:6386–6389.

Cavosie, A. J., Wilde, S. A., Liu, D., Weiblen, P. W., and Valley, J. W. (2004). Internal zoning and U–Th–Pb chemistry of Jack Hills detrital zircons: a mineral record of early Archean to Mesoproterozoic (4348–1576 Ma) magmatism. *Precambrian Res.*, 135:251–279.

Chi, M., Ishii, H. A., Simon, S. B., Bradley, J. P., Dai, Z., Joswiak, D., Browning, N. D., and Matrajt, G. (2009). The origin of refractory minerals in comet 81P/Wild 2. *Geochimica et Cosmochimica Acta*, 73(23):7150–7161.

Ciesla, F. J. (2007). Outward Transport of High-Temperature Materials Around the Midplane of the Solar Nebula. *Science*, 318(5850):613–615. Publisher: American Association for the Advancement of Science.

Cieza, L. A., Casassus, S., Tobin, J., Bos, S. P., Williams, J. P., Perez, S., Zhu, Z., Caceres, C., Canovas, H., Dunham, M. M., Hales, A., Prieto, J. L., Principe, D. A., Schreiber, M. R., Ruiz-Rodriguez, D., and Zurlo, A. (2016). Imaging the water snow-line during a protostellar outburst. *Nature*, 535(7611):258–261. Bandiera_abtest: a Cg_type: Nature Research Journals Number: 7611 Primary_atype: Research Publisher: Nature Publishing Group Subject_term: Exoplanets;Interstellar medium;Stars Subject_term_id: exoplanets;interstellar-medium;stars.

Clarke, C. J., Gendrin, A., and Sotomayor, M. (2001). The dispersal of circumstellar discs: the role of the ultraviolet switch. *Monthly Notices of the Royal Astronomical Society*, 328(2):485–491.

Compston, W. and Pidgeon, R. T. (1986). Jack Hills, evidence of more very old detrital zircons in Western Australia. *NATURE*, 321:766–769.

Concha-Ramírez, F., Wilhelm, M. J. C., Portegies Zwart, S., and Haworth, T. J. (2019). External photoevaporation of circumstellar discs constrains the timescale for planet formation. *Monthly Notices of the Royal Astronomical Society*, 490(4):5678–5690.

Connelly, J. N., Bollard, J., and Bizzarro, M. (2017). Pb–Pb chronometry and the early Solar System. *Geochimica et Cosmochimica Acta*, 201:345–363.

Corfu, F., Hanchar, J. M., Hoskin, P. W., and Kinny, P. (2003). Atlas of Zircon Textures. *Reviews in Mineralogy and Geochemistry*, 53(1):469–500.

Cournede, C., Gattacceca, J., Gounelle, M., Rochette, P., Weiss, B. P., and Zanda, B. (2015). An early solar system magnetic field recorded in CM chondrites. *Earth and Planetary Science Letters*, 410:62–74.

Davidson, J., Alexander, C. M. O., Stroud, R. M., Busemann, H., and Nittler, L. R. (2019). Mineralogy and petrology of Dominion Range 08006: A very primitive CO3 carbonaceous chondrite. *Geochimica et Cosmochimica Acta*, 265:259–278.

Davis, A. M. and MacPherson, G. J. (1996). Thermal processing in the solar nebula: Constraints from refractory inclusions. In Hewins, R. H., Jones, R. H., and Scott, E. R. D., editors, *Chondrules and the Protoplanetary Disk*, pages 71–86. Cambridge University Press, Cambridge, UK.

DeMeo, F. E. and Carry, B. (2014). Solar System evolution from compositional mapping of the asteroid belt. *Nature*, 505(7485):629–634. Number: 7485 Publisher: Nature Publishing Group.

Desch, S. J., Kalyaan, A., and Alexander, C. M. O. (2018). The effect of jupiter's formation on the distribution of refractory elements and inclusions in meteorites. *The Astrophysical Journal Supplement Series*, 238(1):11.

Desch, S. J., Morris, M. A., Connolly, H. C., and Boss, A. P. (2010). A critical examination of the X-wind model for chondrules and calcium-rich, aluminum-rich inclusion formation and radionuclide production. *The Astrophysical Journal*, 725(1):692–711.

Desch, S. J., Morris, M. A., Connolly, H. C., and Boss, A. P. (2012). The importance of experiments: Constraints on chondrule formation models. *Meteoritics & Planetary Science*, 47(7):1139–1156.

Dougherty, M. K., Cao, H., Khurana, K. K., Hunt, G. J., Provan, G., Kellock, S., Burton, M. E., Burk, T. A., Bunce, E. J., Cowley, S. W. H., Kivelson, M. G., Russell, C. T., and Southwood, D. J. (2018). Saturn's magnetic field revealed by the Cassini Grand Finale. *Science*, 362(6410):eaat5434. Publisher: American Association for the Advancement of Science.

Doyle, P. M., Jogo, K., Nagashima, K., Krot, A. N., Wakita, S., Ciesla, F. J., and Hutcheon, I. D. (2014). Early aqueous activity on the ordinary and carbonaceous chondrite parent bodies recorded by fayalite. *Nature Commun.*, 6:7444.

Dullemond, C. P. and Dominik, C. (2005). Dust coagulation in protoplanetary disks: A rapid depletion of small grains. *Astron. Astrophys.*, 434:971–986.

Dunlop, D. J. (2002). Theory and application of the Day plot (M_{rs}/M_s versus H_{cr}/H_c) - 1. Theoretical curves and tests using titanomagnetite data. *J. Geophys. Res.*, 107:EPM 4–1–EPM 4–22.

Dunlop, D. J. and Özdemir, O. (1997). *Rock magnetism: Fundamentals and Frontiers*. Cambridge Studies in Magnetism. Cambridge University Press, New York.

Dyl, K. A., Bischoff, A., Ziegler, K., Young, E. D., Wimmer, K., and Bland, P. A. (2012). Early Solar System hydrothermal activity in chondritic asteroids on 1–10-year timescales. *Proceedings of the National Academy of Sciences*, 109(45):18306–18311. Publisher: National Academy of Sciences Section: Physical Sciences.

Ebert, S., Render, J., Brennecka, G. A., Burkhardt, C., Bischoff, A., Gerber, S., and Kleine, T. (2018). Ti isotopic evidence for a non-CAI refractory component in the inner Solar System. *Earth and Planetary Science Letters*, 498:257–265.

Einsle, J. F., Harrison, R. J., Kasama, T., Conbhuí, P. , Fabian, K., Williams, W., Woodland, L., Fu, R. R., Weiss, B. P., and Midgley, P. A. (2016). Multi-scale three-dimensional characterisation of iron particles in dusty olivine: implications for paleomagnetism of chondritic meteorites. *Am. Mineral.*, 101:2070–2084.

Ercolano, B. and Pascucci, I. (2017). The dispersal of planet-forming discs: theory confronts observations. *Royal Society Open Science*, 4(4):170114. Publisher: Royal Society.

Fromang, S., Lyra, W., and Masset, F. (2011). Meridional circulation in turbulent protoplanetary disks. *Astronomy & Astrophysics*, 534:A107. Publisher: EDP Sciences.

Fu, R. R., Drabon, N., Wiedenbeck, M., Brenner, A. R., Lowe, D., and Borlina, C. S. (2020a). Paleomagnetism of 3.5-4.0 Ga zircons from the Barberton Greenstone Belt, South Africa.

Fu, R. R., Kehayias, P., Weiss, B. P., Schrader, D. L., Bai, X.-N., and Simon, J. B. (2020b). Weak Magnetic Fields in the Outer Solar Nebula Recorded in CR Chondrites. *Journal of Geophysical Research: Planets*, (5):e2019JE006260. _eprint: https://agupubs.onlinelibrary.wiley.com/doi/pdf/10.1029/2019JE006260.

Fu, R. R., Lima, E. A., Volk, M. W. R., and Trubko, R. (2020c). High-Sensitivity Moment Magnetometry With the Quantum Diamond Microscope. *Geochemistry, Geophysics, Geosystems*, 21(8):e2020GC009147. _eprint: https://agupubs.onlinelibrary.wiley.com/doi/pdf/10.1029/2020GC009147.

Fu, R. R., Volk, M. W. R., Bilardello, D., Libourel, G., Lesur, G. R. J., and Dor, O. B. (2021). The Fine-Scale Magnetic History of the Allende Meteorite: Implications for the Structure of the Solar Nebula. *AGU Advances*, 2(3):e2021AV000486. _eprint: https://agupubs.onlinelibrary.wiley.com/doi/pdf/10.1029/2021AV000486.

Fu, R. R., Weiss, B. P., Lima, E. A., Harrison, R. J., Bai, X.-N., Desch, S. J., Ebel, D. S., Suavet, C., Wang, H., Glenn, D., Le Sage, D., Kasama, T., Walsworth, R. L., and Kuan, A. T. (2014). Solar nebula magnetic fields recorded in the Semarkona meteorite. *Science*, 346:1089–1092.

Fu, R. R., Weiss, B. P., Lima, E. A., Kehayias, P., Araujo, J. F. D. F., Glenn, D. R., Gelb, J., Einsle, J. F., Bauer, A. M., Harrison, R. J., Ali, G. A. H., and Walsworth, R. L. (2017). Evaluating the paleomagnetic potential of single zircon crystals using the Bishop Tuff. *Earth and Planetary Science Letters*, 458:1–13.

Fujiya, W., Sugiura, N., Hotta, H., Ichimura, K., and Sano, Y. (2012). Evidence for the late formation of hydrous asteroids from young meteoritic carbonates. *Nature Communications*, 3(1):627. Number: 1 Publisher: Nature Publishing Group.

Ganino, C. and Libourel, G. (2020). Fumarolic-like activity on carbonaceous chondrite parent body. *Science Advances*, 6(27):eabb1166. Publisher: American Association for the Advancement of Science.

Gattacceca, J. and Rochette, P. (2004). Toward a robust normalized magnetic paleointensity method applied to meteorites. *Earth and Planetary Science Letters*, 227(3):377–393.

Gattacceca, J., Weiss, B. P., and Gounelle, M. (2016). New constraints on the magnetic history of the CV parent body and the solar nebula from the Kaba meteorite. *Earth Planet. Sci. Lett.*, 455:166–175.

Geisler, T., Schaltegger, U., and Tomaschek, F. (2007). Re-equilibration of Zircon in Aqueous Fluids and Melts. *Elements*, 3(1):43–50.

Glenn, D. R., Fu, R. R., Kehayias, P., Sage, D. L., Lima, E. A., Weiss, B. P., and Walsworth, R. L. (2017). Micrometer-scale magnetic imaging of geological samples using a quantum diamond microscope. *Geochemistry, Geophysics, Geosystems*, 18(8):3254–3267.

Gorti, U., Liseau, R., Sándor, Z., and Clarke, C. (2016). Disk Dispersal: Theoretical Understanding and Observational Constraints. *Space Science Reviews*, 205(1):125–152.

Gounelle, M., Krot, A. N., Nagashima, K., and Kearsley, A. (2009). Extreme ^{16}O enrichment in calcium-aluminum-rich inclusions from the Isheyevo (CH/CB) chondrite. *The Astrophysical Journal*, 698(1):L18–L22.

Grossman, J. N. and Brearley, A. J. (2005). The onset of metamorphism in ordinary and carbonaceous chondrites. *Meteoritics & Planetary Science*, 40(1):87–122.

Gunell, H., Maggiolo, R., Nilsson, H., Wieser, G. S., Slapak, R., Lindkvist, J., Hamrin, M., and Keyser, J. D. (2018). Why an intrinsic magnetic field does not protect a planet against atmospheric escape. *Astronomy & Astrophysics*, 614:L3. Publisher: EDP Sciences.

Haisch, K. E., Lada, E. A., and Lada, C. J. (2001). Disk frequencies and lifetimes in young clusters. *Astrophys. J.*, 553:L153–L156.

Hartmann, L., Calvet, N., Gullbring, E., and D'Alessio, P. (1998). Accretion and the Evolution of T Tauri Disks. *Astrophys. J.*, 495(1):385. Publisher: IOP Publishing.

Hartmann, L., Herczeg, G., and Calvet, N. (2016). Accretion onto Pre-Main-Sequence Stars. *Annual Review of Astronomy and Astrophysics*, 54(1):135–180. Publisher: Annual Reviews.

Heider, F. and Dunlop, D. J. (1987). Two types of chemical remanent magnetization during the oxidation of magnetite. *Physics of the Earth and Planetary Interiors*, 46(1):24–45.

Herndon, J. M., Rowe, M. W., Larson, E. E., and Watson, D. E. (1976). Thermomagnetic analysis of meteorites, 3. C3 and C4 chondrites. *Earth and Planetary Science Letters*, 29(2):283–290.

Hernández, J., Hartmann, L., Megeath, T., Gutermuth, R., Muzerolle, J., Calvet, N., Vivas, A. K., Briceño, C., Allen, L., Stauffer, J., Young, E., and Fazio, G. (2007). A Spitzer Space Telescope Study of Disks in the Young Orionis Cluster. *The Astrophysical Journal*, 662:1067–1081. ADS Bibcode: 2007ApJ...662.1067H.

Heslop, D. (2007). Are hydrodynamic shape effects important when modelling the formation of depositional remanent magnetization? *Geophysical Journal International*, 171(3):1029–1035.

Hu, Z. and Bai, X.-N. (2021). Dust Transport in Protoplanetary Disks with Wind-driven Accretion. *arXiv:2102.01110 [astro-ph]*. arXiv: 2102.01110.

Ireland, M. J. and Kraus, A. L. (2008). The Disk Around CoKu Tauri/4: Circumbinary, Not Transitional*. *The Astrophysical Journal*, 678(1):L59. Publisher: IOP Publishing.

Jiang, Z., Liu, Q., Dekkers, M. J., Zhao, X., Roberts, A. P., Yang, Z., Jin, C., and Liu, J. (2017). Remagnetization mechanisms in Triassic red beds from South China. *Earth and Planetary Science Letters*, 479:219–230.

Johnson, B. C., Walsh, K. J., Minton, D. A., Krot, A. N., and Levison, H. F. (2016). Timing of the formation and migration of giant planets as constrained by CB chondrites. *Science Advances*, 2(12):e1601658. Publisher: American Association for the Advancement of Science Section: Research Article.

Johnson, C. L., Mittelholz, A., Langlais, B., Russell, C. T., Ansan, V., Banfield, D., Chi, P. J., Fillingim, M. O., Forget, F., Haviland, H. F., Golombek, M., Joy, S., Lognonné, P., Liu, X., Michaut, C., Pan, L., Quantin-Nataf, C., Spiga, A., Stanley, S., Thorne, S. N., Wieczorek, M. A., Yu, Y., Smrekar, S. E., and Banerdt, W. B. (2020). Crustal and time-varying magnetic fields at the InSight landing site on Mars. *Nature Geoscience*, 13(3):199–204. Bandiera_abtest: a Cg_type: Nature Research Journals Number: 3 Primary_atype: Research Publisher: Nature Publishing Group Subject_term: Core processes;Geomagnetism;Inner planets;Magnetospheric physics Subject_term_id: core-processes;geomagnetism;inner-planets;magnetospheric-physics.

Kirschvink, J. L. (1980). The least-squares line and plane and the analysis of paleomagnetic data: examples from Siberia and Morocco. *Geophys. J. R. Astr. Soc.*, 62:699–718.

Kirschvink, J. L., Kopp, R. E., Raub, T. D., Baumgartner, C. T., and Holt, J. W. (2008). Rapid, precise, and high-sensitivity acquisition of paleomagnetic and rock-magnetic data: Development of a low-noise automatic sample changing system for superconducting rock magnetometers. *Geochemistry, Geophysics, Geosystems*, 9(5). _eprint: https://agupubs.onlinelibrary.wiley.com/doi/pdf/10.1029/2007GC001856.

Kita, N. T. and Ushikubo, T. (2011). Evolution of protoplanetary disk inferred from ^{26}Al chronology of individual chondrules. *Meteorit. Planet. Sci.*, 47:1108–1119.

Kita, N. T., Yin, Q.-Z., MacPherson, G. J., Ushikubo, T., Jacobsen, B., Nagashima, K., Kurahashi, E., Krot, A. N., and Jacobsen, S. B. (2013). ^{26}Al-^{26}Mg isotope

systematics of the first solids in the early solar system. *Meteoritics & Planetary Science*, 48(8):1383–1400.

Kleine, T., Budde, G., Burkhardt, C., Kruijer, T. S., Worsham, E. A., Morbidelli, A., and Nimmo, F. (2020). The Non-carbonaceous–Carbonaceous Meteorite Dichotomy. *Space Science Reviews*, 216(4):55.

Krot, A. N. (2019). Refractory inclusions in carbonaceous chondrites: Records of early solar system processes. *Meteoritics & Planetary Science*, 54(8):1647–1691.

Krot, A. N., Amelin, Y., Bland, P., Ciesla, F. J., Connelly, J. N., Davis, A. M., Huss, G. R., Hutcheon, I. D., Makide, K., Nagashima, K., Nyquist, L. E., Russell, S. S., Scott, E. R. D., Thrane, K., Yurimoto, H., and Yin, Q.-Z. (2009). Origin and chronology of chondritic components: A review. *Geochim. Cosmochim. Acta*, 73:4963–4997.

Krot, A. N., Amelin, Y., Cassen, P., and Meibom, A. (2005). Young chondrules in CB chondrites from a giant impact in the early Solar System. *Nature*, 436(7053):989–992. Number: 7053 Publisher: Nature Publishing Group.

Krot, A. N., Hutcheon, I. D., Brearley, A. J., Pravdivtseva, O. V., Petaev, M. I., and Hohenberg, C. M. (2006). Timescales and settings for alteration of chondritic meteorites. In Lauretta, D. S. and McSween, H. Y., editors, *Meteorites and the Early Solar System II*, pages 525–553. University of Arizona Press, Tucson.

Kruijer, T. S., Kleine, T., and Borg, L. E. (2020). The great isotopic dichotomy of the early Solar System. *Nature Astronomy*, 4(1):32–40. Number: 1 Publisher: Nature Publishing Group.

Lappe, S.-C. L. L., Church, N. S., Kasama, T., Fanta, A. B. d. S., Bromiley, G., Dunin-Borkowski, R. E., Feinberg, J. M., Russell, S., and Harrison, R. J. (2011). Mineral magnetism of dusty olivine: A credible recorder of pre-accretionary remanence. *Geochemistry, Geophysics, Geosystems*, 12(12).

Lappe, S.-C. L. L., Feinberg, J. M., Muxworthy, A., and Harrison, R. J. (2013). Comparison and calibration of nonheating paleointensity methods: A case study using dusty olivine. *Geochemistry, Geophysics, Geosystems*, 14(7):2143–2158.

Li, Y., Rubin, A. E., and Hsu, W. (2021). Formation of metallic-Cu-bearing mineral assemblages in type-3 ordinary and CO chondrites. *American Mineralogist*, 106(11):1751–1767.

Lichtenberg, T., Drażkowska, J., Schönbächler, M., Golabek, G. J., and Hands, T. O. (2021). Bifurcation of planetary building blocks during Solar System formation. *Science*, 371(6527):365–370. Publisher: American Association for the Advancement of Science Section: Research Article.

Lima, E. A. and Weiss, B. P. (2016). Ultra-high sensitivity moment magnetometry of geological samples using magnetic microscopy. *Geochemistry, Geophysics, Geosystems*, 17(9):3754–3774.

Liu, M.-C., McKeegan, K. D., Harrison, T. M., Jarzebinski, G., and Vltava, L. (2018). The Hyperion-II radio-frequency oxygen ion source on the UCLA ims1290 ion microprobe: Beam characterization and applications in geochemistry and cosmochemistry. *International Journal of Mass Spectrometry*, 424:1–9.

MacPherson, G. J. (2013). Calcium-aluminum-rich inclusions in chondritic meteorites. In Turekian, K. K. and Holland, H. D., editors, *Treatise on Geochemistry*, Planets, Asteroids, Comets, and The Solar System, pages 139–179. Elsevier Science, Amsterdam, second edition.

MacPherson, G. J., Bullock, E. S., Tenner, T. J., Nakashima, D., Kita, N. T., Ivanova, M. A., Krot, A. N., Petaev, M. I., and Jacobsen, S. B. (2017). High precision Al–Mg systematics of forsterite-bearing Type B CAIs from CV3 chondrites. *Geochimica et Cosmochimica Acta*, 201:65–82.

MacPherson, G. J., Simon, S. B., Davis, A. M., Grossman, L., and Krot, A. N. (2005). Calcium-Aluminum-rich Inclusions: Major Unanswered Questions. 341:225. Conference Name: Chondrites and the Protoplanetary Disk ADS Bibcode: 2005ASPC..341..225M.

McClelland, E. (1996). Theory of CRM acquired by grain growth, and its implications for TRM discrimination and palaeointensity determination in igneous rocks. *Geophysical Journal International*, 126(1):271–280. Publisher: Oxford Academic.

McKeegan, K. D., Chaussidon, M., and Robert, F. (2000). Incorporation of Short-Lived 10Be in a Calcium-Aluminum-Rich Inclusion from the Allende Meteorite. *Science*, 289(5483):1334–1337. Publisher: American Association for the Advancement of Science Section: Report.

McSween, H. Y. (1999). *Meteorites and Their Parent Planets*. Cambridge University Press, Cambridge, 2 edition.

Mighani, S., Wang, H., Shuster, D. L., Borlina, C. S., Nichols, C. I. O., and Weiss, B. P. (2020). The end of the lunar dynamo. *Science Advances*, 6(1):eaax0883.

Moore, K. M., Cao, H., Bloxham, J., Stevenson, D. J., Connerney, J. E. P., and Bolton, S. J. (2019). Time variation of Jupiter's internal magnetic field consistent with zonal wind advection. *Nature Astronomy*, 3(8):730–735. Bandiera_abtest: a Cg_type: Nature Research Journals Number: 8 Primary_atype: Research Publisher: Nature Publishing Group Subject_term: Atmospheric dynamics;Core processes;Giant planets;Planetary science Subject_term_id: atmospheric-dynamics;core-processes;giant-planets;planetary-science.

Moore, K. M., Yadav, R. K., Kulowski, L., Cao, H., Bloxham, J., Connerney, J. E. P., Kotsiaros, S., Jørgensen, J. L., Merayo, J. M. G., Stevenson, D. J., Bolton, S. J., and Levin, S. M. (2018). A complex dynamo inferred from the hemispheric dichotomy of Jupiter's magnetic field. *Nature*, 561(7721):76–78. Bandiera_abtest: a Cg_type: Nature Research Journals Number: 7721 Primary_atype: Research Publisher: Nature Publishing Group Subject_term: Core processes;Giant planets Subject_term_id: core-processes;giant-planets.

Morbidelli, A., Walsh, K. J., O'Brien, D. P., Minton, D. A., and Bottke, W. F. (2015). The Dynamical Evolution of the Asteroid Belt. *Asteroids IV*, pages 493–507.

Nagata, T., Funaki, M., and Kojima, H. (1991). Magnetic properties and natural remanent magnetization of carbonaceous chondrites containing pyrrhotite. *Antarctic Meteorite Research*, 4:390.

Nagy, L., Williams, W., Tauxe, L., and Muxworthy, A. R. (2019a). From Nano to Micro: Evolution of Magnetic Domain Structures in Multidomain Magnetite. *Geochemistry, Geophysics, Geosystems*, 20(6):2907–2918. _eprint: https://agupubs.onlinelibrary.wiley.com/doi/pdf/10.1029/2019GC008319.

Nagy, L., Williams, W., Tauxe, L., Muxworthy, A. R., and Ferreira, I. (2019b). Thermomagnetic recording fidelity of nanometer-sized iron and implications for planetary magnetism. *Proc. Natl. Acad. Sci. USA*, 116(6):1984–1991.

Oran, R., Weiss, B. P., and Cohen, O. (2018). Were chondrites magnetized by the early solar wind? *Earth and Planetary Science Letters*, 492:222–231.

Owen, J. E. (2016). The Origin and Evolution of Transition Discs: Successes, Problems, and Open Questions. *Publications of the Astronomical Society of Australia*, 33. Publisher: Cambridge University Press.

Owen, J. E., Clarke, C. J., and Ercolano, B. (2012). On the theory of disc photoevaporation. *Mon. Not. R. Astron. Soc.*, 422(3):1880–1901.

O'Brien, T., Tarduno, J. A., Anand, A., Smirnov, A. V., Blackman, E. G., Carroll-Nellenback, J., and Krot, A. N. (2020). Arrival and magnetization of carbonaceous chondrites in the asteroid belt before 4562 million years ago. *Communications Earth & Environment*, 1(1):1–7. Bandiera_abtest: a Cc_license_type: cc_by Cg_type: Nature Research Journals Number: 1 Primary_atype: Research Publisher: Nature Publishing Group Subject_term: Asteroids, comets and Kuiper belt;Early solar system;Meteoritics Subject_term_id: asteroids-comets-and-kuiper-belt;early-solar-system;meteoritics.

Paterson, G. A., Tauxe, L., Biggin, A. J., Shaar, R., and Jonestrask, L. C. (2014). On improving the selection of Thellier-type paleointensity data. *Geochem. Geophys. Geosyst.*, 15(4):1180–1192.

Patterson, C., Settle, D., and Glover, B. (1976). Analysis of lead in polluted coastal seawater. *Marine Chemistry*, 4(4):305–319.

Piazolo, S., La Fontaine, A., Trimby, P., Harley, S., Yang, L., Armstrong, R., and Cairney, J. M. (2016). Deformation-induced trace element redistribution in zircon revealed using atom probe tomography. *Nature Communications*, 7(1):10490. Bandiera_abtest: a Cc_license_type: cc_by Cg_type: Nature Research Journals Number: 1 Primary_atype: Research Publisher: Nature Publishing Group Subject_term: Geochemistry;Geology Subject_term_id: geochemistry;geology.

Picogna, G., Ercolano, B., Owen, J. E., and Weber, M. L. (2019). The dispersal of protoplanetary discs – I. A new generation of X-ray photoevaporation models. *Monthly Notices of the Royal Astronomical Society*, 487(1):691–701.

Pravdivtseva, O., Meshik, A., and Hohenberg, C. M. (2013). The I-Xe record: Early onset of aqueous alteration in magnetites separated from CM and CV chondrites. *Lunar Planet Sci. Conf. XLIV*, page abstract #3104.

Quidelleur, X., Grove, M., Lovera, O. M., Harrison, T. M., Yin, A., and Ryerson, F. J. (1997). Thermal evolution and slip history of the Renbu Zedong Thrust, southeastern Tibet. *Journal of Geophysical Research*, 102:2659–2679. ADS Bibcode: 1997JGR...102.2659Q.

Richter, F. M., Davis, A. M., Ebel, D. S., and Hashimoto, A. (2002). Elemental and isotopic fractionation of Type B calcium-, aluminum-rich inclusions: experiments, theoretical considerations, and constraints on their thermal evolution. *Geochimica et Cosmochimica Acta*, 66(3):521–540.

Righter, K., Sutton, S. R., Danielson, L., Pando, K., and Newville, M. (2016). Redox variations in the inner solar system with new constraints from vanadium XANES in spinels. *American Mineralogist*, 101(9):1928–1942.

Rosotti, G. P., Ercolano, B., Owen, J. E., and Armitage, P. J. (2013). The interplay between X-ray photoevaporation and planet formation. *Monthly Notices of the Royal Astronomical Society*, 430(2):1392–1401. Publisher: Oxford Academic.

Salmeron, R. and Ireland, T. R. (2012). Formation of chondrules in magnetic winds blowing through the proto-asteroid belt. *Earth and Planetary Science Letters*, 327-328:61–67.

Sato, M., Yamamoto, S., Yamamoto, Y., Okada, Y., Ohno, M., Tsunakawa, H., and Maruyama, S. (2015). Rock-magnetic properties of single zircon crystals sampled from the Tanzawa tonalitic pluton, central Japan. *Earth, Planets, Space*, 67:DOI 10.1186/s40623–015–0317–9.

Scally, A. and Clarke, C. (2001). Destruction of protoplanetary discs in the Orion Nebula Cluster. *Monthly Notices of the Royal Astronomical Society*, 325(2):449–456.

Schrader, D. L., Davidson, J., McCoy, T. J., Zega, T. J., Russell, S. S., Domanik, K. J., and King, A. J. (2021). The Fe/S ratio of pyrrhotite group sulfides in chondrites: An indicator of oxidation and implications for return samples from asteroids Ryugu and Bennu. *Geochimica et Cosmochimica Acta*, 303:66–91.

Schrader, D. L., Nagashima, K., Krot, A. N., Ogliore, R. C., Yin, Q.-Z., Amelin, Y., Stirling, C. H., and Kaltenbach, A. (2017). Distribution of ^{26}Al in the CR chondrite chondrule-forming region of the protoplanetary disk. *Geochim. Cosmochim. Acta*, 201:275–302.

Scott, E. R. D., Keil, K., and Stöffler, D. (1992). Shock metamorphism of carbonaceous chondrites. *Geochimica et Cosmochimica Acta*, 56(12):4281–4293.

Scott, E. R. D. and Krot, A. N. (2013). Chondrites and their components. In Holland, H. D. and Turekian, K. K., editors, *Treatise on Geochemistry*, volume 2 of *Planets, Asteroids, Comets, and the Solar System*, pages 66–137. Elsevier Science, Amsterdam.

Scott, E. R. D., Krot, A. N., and Sanders, I. S. (2018). Isotopic dichotomy among meteorites and its bearing on the protoplanetary disk. *The Astrophysical Journal*, 854(2):164.

Shadmehri, M. and Ghoreyshi, S. M. (2019). Time-dependent evolution of the protoplanetary discs with magnetic winds. *Monthly Notices of the Royal Astronomical Society*, 488(4):4623–4637.

Shah, J., Williams, W., Almeida, T. P., Nagy, L., Muxworthy, A. R., Kovács, A., Valdez-Grijalva, M. A., Fabian, K., Russell, S. S., Genge, M. J., and Dunin-Borkowski, R. E. (2018). The oldest magnetic record in our solar system identified using nanometric imaging and numerical modeling. *Nature Communications*, 9(1):1–6.

Shu, F. H., Shang, H., and Lee, T. (1996). Toward an astrophysical theory of chondrites. *Science*, 271(5255):1545–1552.

Simon, S. B., Krot, A. N., Nagashima, K., Kööp, L., and Davis, A. M. (2019). Condensate refractory inclusions from the CO3.00 chondrite Dominion Range 08006: Petrography, mineral chemistry, and isotopic compositions. *Geochimica et Cosmochimica Acta*, 246:109–122.

Smethurst, M. T. and Herrero-Bervera, E. (2002). Paleomagnetic Analysis of Calcium-Aluminum Inclusions (CAI's) from the Allende Meteorite. In *AGU Fall Meeting Abstracts*, volume 72, pages GP72A–0989.

Smith, R. J. (2009). Use and misuse of the reduced major axis for line-fitting. *American Journal of Physical Anthropology*, 140(3):476–486. _eprint: https://onlinelibrary.wiley.com/doi/pdf/10.1002/ajpa.21090.

Spencer, C. J., Kirkland, C. L., and Taylor, R. J. M. (2016). Strategies towards statistically robust interpretations of in situ U–Pb zircon geochronology. *Geoscience Frontiers*, 7(4):581–589.

Sridhar, S., Bryson, J. F. J., King, A. J., and Harrison, R. J. (2021). Constraints on the ice composition of carbonaceous chondrites from their magnetic mineralogy. *Earth and Planetary Science Letters*, 576:117243.

Stephenson, A. (1993). Three-axis static alternating field demagnetization of rocks and the identification of natural remanent magnetization, gyroremanent magnetization, and anisotropy. *Journal of Geophysical Research: Solid Earth*, 98(B1):373–381. _eprint: https://agupubs.onlinelibrary.wiley.com/doi/pdf/10.1029/92JB01849.

Sterenborg, M. G. and Crowley, J. W. (2013). Thermal evolution of early solar system planetesimals and the possibility of sustained dynamos. *Phys. Earth Planet. Inter.*, 214:53–73.

Sugiura, N. and Krot, A. N. (2007). ^{26}Al-^{26}Mg systematics of Ca-Al-rich inclusions, amoeboid olivine aggregates, and chondrules from the ungrouped carbonaceous chondrite Acfer 094. *Meteoritics & Planetary Science*, 42(7-8):1183–1195.

Sutton, S., Alexander, C. M. O., Bryant, A., Lanzirotti, A., Newville, M., and Cloutis, E. A. (2017). The bulk valence state of Fe and the origin of water in chondrites. *Geochimica et Cosmochimica Acta*, 211:115–132.

Suzuki, T. K., Ogihara, M., Morbidelli, A., Crida, A., and Guillot, T. (2016). Evolution of protoplanetary discs with magnetically driven disc winds. *Astronomy & Astrophysics*, 596:A74. Publisher: EDP Sciences.

Tang, F., Taylor, R. J. M., Einsle, J. F., Borlina, C. S., Fu, R. R., Weiss, B. P., Williams, H. M., Williams, W., Nagy, L., Midgley, P. A., Lima, E. A., Bell, E. A., Harrison, T. M., Alexander, E. W., and Harrison, R. J. (2019). Secondary magnetite in ancient zircon precludes analysis of a Hadean geodynamo. *Proceedings of the National Academy of Sciences*, 116(2):407–412.

Tang, H., Liu, M.-C., McKeegan, K. D., Tissot, F. L. H., and Dauphas, N. (2017). In situ isotopic studies of the U-depleted Allende CAI Curious Marie: Pre-accretionary alteration and the co-existence of 26Al and 36Cl in the early solar nebula. *Geochimica et Cosmochimica Acta*, 207:1–18.

Tarduno, J. A., Blackman, E. G., and Mamajek, E. E. (2014). Detecting the oldest geodynamo and attendant shielding from the solar wind: Implications for habitability. *Phys. Earth Planet. Inter.*, 233:68–87.

Tarduno, J. A., Cottrell, R. D., Bono, R. K., Oda, H., Davis, W. J., Fayek, M., Erve, O. v. Nimmo, F., Huang, W., Thern, E. R., Fearn, S., Mitra, G., Smirnov, A. V., and Blackman, E. G. (2020). Paleomagnetism indicates that primary magnetite in

zircon records a strong Hadean geodynamo. *Proceedings of the National Academy of Sciences*.

Tarduno, J. A., Cottrell, R. D., Davis, W. J., Nimmo, F., and Bono, R. K. (2015). A Hadean to Paleoarchean geodynamo recorded by single zircon crystals. *Science*, 349:521–524.

Tauxe, L. (2010). *Essentials of Paleomagnetism*. University of California Press.

Tauxe, L. and Staudigel, H. (2004). Strength of the geomagnetic field in the Cretaceous Normal Superchron: New data from submarine basaltic glass of the Troodos Ophiolite. *Geochemistry, Geophysics, Geosystems*, 5(2). _eprint: https://agupubs.onlinelibrary.wiley.com/doi/pdf/10.1029/2003GC000635.

Tikoo, S. M., Weiss, B. P., Buz, J., Lima, E. A., Shea, E. K., Melo, G., and Grove, T. L. (2012). Magnetic fidelity of lunar samples and implications for an ancient core dynamo. *Earth and Planetary Science Letters*, 337-338:93–103.

Tikoo, S. M., Weiss, B. P., Cassata, W. S., Shuster, D. L., Gattacceca, J., Lima, E. A., Suavet, C., Nimmo, F., and Fuller, M. D. (2014). Decline of the lunar core dynamo. *Earth and Planetary Science Letters*, 404:89–97.

Tikoo, S. M., Weiss, B. P., Shuster, D. L., Suavet, C., Wang, H., and Grove, T. L. (2017). A two-billion-year history for the lunar dynamo. *Sci. Adv.*, 3:e1700207.

Timms, N. E., Reddy, S. M., Fitz Gerald, J. D., Green, L., and Muhling, J. R. (2012). Inclusion-localised crystal-plasticity, dynamic porosity, and fast-diffusion pathway generation in zircon. *Journal of Structural Geology*, 35:78–89.

Torrano, Z. A., Schrader, D. L., Davidson, J., Greenwood, R. C., Dunlap, D. R., and Wadhwa, M. (2021). The relationship between CM and CO chondrites: Insights from combined analyses of titanium, chromium, and oxygen isotopes in CM, CO, and ungrouped chondrites. *Geochimica et Cosmochimica Acta*, 301:70–90.

Trail, D., Cherniak, D. J., Watson, E. B., Harrison, T. M., Weiss, B. P., and Szumila, I. (2016). Li zoning in zircon as a potential geospeedometer and peak temperature indicator. *Contrib. Mineral. Petrol.*, 171:doi:10.1007/s00410–016–1238–8.

Turner, N. J., Fromang, S., Gammie, C., Klahr, H., Lesur, G., Wardle, M., and Bai, X.-N. (2014). Transport and accretion in planet-forming disks. In *Protostars and Planets VI*, pages 411–432. University of Arizona Press.

Wang, H., Weiss, B. P., Bai, X.-N., Downey, B. G., Wang, J., Wang, J., Suavet, C., Fu, R. R., and Zucolotto, M. E. (2017). Lifetime of the solar nebula constrained by meteorite paleomagnetism. *Science*, 355(6325):623–627.

Wang, L., Bai, X.-N., and Goodman, J. (2019). Global Simulations of Protoplanetary Disk Outflows with Coupled Non-ideal Magnetohydrodynamics and Consistent Thermochemistry. *The Astrophysical Journal*, 874(1):90. Publisher: American Astronomical Society.

Wang, Q. and Wilde, S. A. (2018). New constraints on the Hadean to Proterozoic history of the Jack Hills belt, Western Australia. *Gondwana Research*, 55:74–91.

Watson, G. S. (1956). A test for randomness of directions. *Geophysical Journal International*, 7:160–161.

Weiss, B. P., Bai, X.-N., and Fu, R. R. (2021). History of the solar nebula from meteorite paleomagnetism. *Science Advances*, 7(1):eaba5967. Publisher: American Association for the Advancement of Science Section: Review.

Weiss, B. P. and Bottke, W. F. (2021). What Can Meteorites Tell Us About the Formation of Jupiter? *AGU Advances*, 2(2):e2020AV000376. _eprint: https://agupubs.onlinelibrary.wiley.com/doi/pdf/10.1029/2020AV000376.

Weiss, B. P., Fu, R. R., Einsle, J. F., Glenn, D. R., Kehayias, P., Bell, E. A., Gelb, J., Araujo, J., Lima, E. A., Borlina, C. S., Boehnke, P., Johnstone, D. N., Harrison, T. M., Harrison, R. J., and Walsworth, R. L. (2018). Secondary magnetic inclusions in detrital zircons from the Jack Hills, Western Australia, and implications for the origin of the geodynamo. *GEOLOGY*, 46(5):427–430.

Weiss, B. P., Gattacceca, J., Stanley, S., Rochette, P., and Christensen, U. R. (2010). Paleomagnetic records of meteorites and early planetesimal differentiation. *Space Science Reviews*, 152(1):341–390.

Weiss, B. P., Lima, E. A., Fong, L. E., and Baudenbacher, F. J. (2007). Paleomagnetic analysis using SQUID microscopy. *J. Geophys. Res.: Solid Earth*, 112:B09105, doi:10.1029/2007JB004940.

Weiss, B. P., Maloof, A. C., Harrison, T. M., Swanson-Hysell, N. L., Fu, R. R., Kirschvink, J. L., Watson, E. B., Coe, R. S., Tikoo, S. M., and Ramezani, J. (2016). Reply to Comment on "Pervasive remagnetization of detrital zircon host rocks in the Jack Hills, Western Australia and implications for records of the early dynamo". *Earth Planet. Sci. Lett.*, 450:409–412.

Weiss, B. P., Maloof, A. C., Tailby, N., Ramezani, J., Fu, R. R., Hanus, V., Trail, D., Watson, E. B., Harrison, T. M., Bowring, S. A., Kirschvink, J. L., Swanson-Hysell, N. L., and Coe, R. S. (2015). Pervasive remagnetization of detrital zircon host rocks in the Jack Hills, Western Australia and implications for records of the early geodynamo. *Earth Planet. Sci. Lett.*, 430:115–128.

Weiss, B. P. and Tikoo, S. M. (2014). The lunar dynamo. *Science*, 346(6214). Publisher: American Association for the Advancement of Science Section: Review.

Weiss, B. P., Wang, H., Sharp, T. G., Gattacceca, J., Shuster, D. L., Downey, B., Hu, J., Fu, R. R., Kuan, A. T., Suavet, C., Irving, A. J., Wang, J., and Wang, J. (2017). A nonmagnetic differentiated early planetary body. *Earth Planet. Sci. Lett.*, 468:119–132.

White, L. F., Darling, J. R., Moser, D. E., Reinhard, D. A., Prosa, T. J., Bullen, D., Olson, D., Larson, D. J., Lawrence, D., and Martin, I. (2017). Atomic-scale age resolution of planetary events. *Nature Communications*, 8(1):15597. Bandiera_abtest: a Cc_license_type: cc_by Cg_type: Nature Research Journals Number: 1 Primary_atype: Research Publisher: Nature Publishing Group Subject_term: Geochemistry;Meteoritics Subject_term_id: geochemistry;meteoritics.

Wieczorek, M. A., Weiss, B. P., and Stewart, S. T. (2012). An impactor origin for lunar magnetic anomalies. *Science*, 335:1212–1215.

Wood, J. A. (2000). Pressure and Temperature Profiles in the Solar Nebula. *Space Science Reviews*, 92(1):87–93.

Yu, Y., Tauxe, L., and Genevey, A. (2004). Toward an optimal geomagnetic field intensity determination technique. *Geochem. Geophys. Geosyst.*, 5:doi:10.1029/2003GC000630.

Zhang, M., Bonato, E., King, A. J., Russell, S. S., Tang, G., and Lin, Y. (2020). Petrology and oxygen isotopic compositions of calcium-aluminum-rich inclusions in primitive CO3.0-3.1 chondrites. *Meteoritics & Planetary Science*, 55(4):911–935. _eprint: https://onlinelibrary.wiley.com/doi/pdf/10.1111/maps.13473.

Zhu, Z., Nelson, R. P., Hartmann, L., Espaillat, C., and Calvet, N. (2011). Transitional and pre-transitional disks: gap opening by multiple planets? *The Astrophysical Journal*, 729(1):47. Publisher: IOP Publishing.

List of Figures

List of Tables